MSPT : Motion Simulator for Proton Therapy

Paul Morel

UNIVERSITÉ PARIS-EST

Thèse

soumise pour obtenir le grade de
DOCTEUR DE L'UNIVERSITÉ PARIS-EST

MSPT : Motion Simulator for Proton Therapy

Sous la direction de Stéphane Vialette et Xiaodong Wu.
Sous l'encadrement de Guillaume Blin.

Spécialité **Informatique**
École doctorale **MSTIC**
Soutenue publiquement par **Paul Morel**
le **17 novembre 2014**

Jury :

Guillaume BLIN	Université de Bordeaux	Examinateur
Pascal DESBARATS	Université de Bordeaux	Rapporteur
Serge MIGUET	Université Lumière Lyon 2	Rapporteur
Cyril NICAUD	Université Paris-Est	Président
Stéphane VIALETTE	Université Paris-Est	Directeur
Dongxu WANG	University of Iowa	Examinateur
Xiaodong WU	University of Iowa	Directeur

UNIVERSITÉ PARIS-EST

École Doctorale MSTIC

Thèse de doctorat en informatique

MSPT: Motion Simulator for Proton Therapy

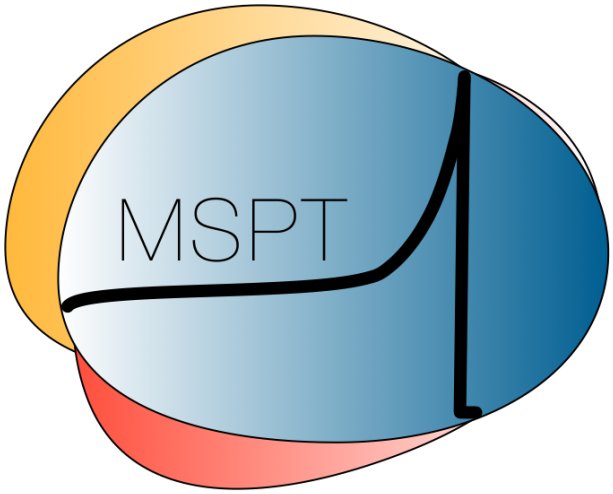

Paul MOREL

Thèse dirigée par Stéphane VIALETTE, co-dirigée par Xiaodong WU et co-encadrée par Guillaume BLIN.

Thèse préparée à l'**Université Paris-Est Marne La Vallée, UMR CNRS 8049 LIGM**, Bâtiment Copernic, 5 boulevard Descartes, Cité Descartes, Champs Sur Marne, 77454 Marne la Vallée cedex 2, France.

À ma fille, Victoria
et à ma femme, Pauline.

Acknowledgments

I thank Guillaume Blin[1], Stéphane Vialette[2] and Xiaodong Wu[3,4], who jointly supervised my research during my PhD studies. They guided me and advised me throughout my work to achieve my research on radiation therapy. I would like to express my gratitude for the precious help of Dongxu Wang[4], who played an important role during my PhD. His advice throughout the development of `MSPT`, his clinical knowledge, his expertise in proton therapy and his help with all the simulations in RayStation have been a great support. I am grateful to Ryan Flynn[4] and Edgar Gelover Reyes[4] for their advice and collaboration on the proton therapy project. I thank Daniel Hyer[4], Yusung Kim[4] and Christina Zacharatou[5] for sharing and discussing about radiation therapy and proton therapy.

I express my thanks to Pascal Desbarats[1], Serge Miguet[6] and Cyril Nicaud[2], members of my committee, for their time, their advice and their interest in my work.

I thank the members of the LIGM and the Université Paris-Est Marne La Vallée for the three years spent together working and sharing good times.

I would like to acknowledge the financial support I received from the ANRduring my PhD: ANR project BIRDS JCJC SIMI 2-2010.

I express my gratitude to my family, Patrick, Thérèse, Pierre, Benoît and Myriam, who nurtured my ambitions and my interest in engineering and in medicine since my young age. I also thank my family-in-law, Vanessa, Catherine, Alexandre, Sylvain, Marie-Françoise, Marion, Etienne, and Quentin for their support, their advice and their thoughtful attention since I know them. I also express my thanks to Vanessa, Pierre, Thérèse and Patrick for reading some parts of this thesis and helping me improve both my English and my French writing.

I thank all my friends, for all the moments we shared during these three years, which allowed me to unwind and to stop thinking about my thesis in order to get back to earth!

I wish to thank especially, Pauline, my wife, for her endless love and support, for the time she spent taking care of so many things while I was working on this thesis, for always believing in me, for encouraging me surpass myself and for making my life happier. Finally, I would like to thank Victoria, our amazing daughter, for being such a source of joy and laugh.

1. LaBRI, Université de Bordeaux (France)
2. LIGM, Université Paris-Est Marne La Vallée (France)
3. Department of Electrical and Computer Engineering, University of Iowa (USA)
4. Department of Radiation Oncology, University of Iowa (USA)
5. Institut Bergonié, Bordeaux (France)
6. LIRIS, Université Lumière Lyon 2 (France)

Abstract

In proton therapy, the delivery method named spot scanning, can provide a particularly efficient treatment in terms of tumor coverage and healthy tissues protection. The dosimetric benefits of proton therapy may be greatly degraded due to intra-fraction motions. Hence, the study of mitigation or adaptive methods is necessary. For this purpose, we developed an open-source 4D dose computation and evaluation software, MSPT (Motion Simulator for Proton Therapy), for the spot-scanning delivery technique. It aims at highlighting the impact of intra-fraction motions during a treatment delivery by computing the dose distribution in the moving patient. In addition, the use of MSPT allowed us to develop and propose a new motion mitigation strategy based on the adjustment of the beam's weight when the proton beam is scanning across the tumor.

In photon therapy, a main concern for deliveries using a multileaf collimator (MLC) relies on finding a series of MLC configurations to deliver properly the treatment. The efficiency of such series is measured by the total beam-on time and the total setup time. In our work, we study the minimization of these efficiency criteria from an algorithmic point of view, for new variants of MLCs: the rotating MLC and the dual-layer MLC. In addition, we propose an approximation algorithm to find a series of configurations that minimizes the total beam-on time for the rotating MLC.

Keywords: Proton therapy, photon therapy, simulator, intra-fraction motions, multileaf collimator decomposition.

Résumé

En proton thérapie, la technique de balayage, permet de traiter efficacement le patient vis à vis de l'irradiation de la tumeur et la protection des tissus sains. Ces bénéfices dosimétriques peuvent cependant être grandement dégradés par les mouvements intra-fraction. Par conséquent, l'étude de méthodes d'atténuation ou d'adaptation est nécessaire. C'est pour cela, que nous avons développé un logiciel "open-source" de calcul et d'évaluation de dose en 4D, MSPT (Motion Simulator for Proton Therapy), pour la technique de balayage. Son but est de mettre en avant l'impact des mouvements intra-fraction en calculant la répartition de dose dans le patient. En outre, l'utilisation de MSPT nous a permis de mettre au point et de proposer une nouvelle méthode d'atténuation du mouvement basée sur l'ajustement du poids du faisceau quand celui-ci balaye la tumeur.

En photon thérapie, un enjeu principal pour les traitements délivrés à l'aide de collimateurs multilames (MLC) consiste à trouver un ensemble de configurations du MLC permettant d'irradier correctement la tumeur. L'efficacité d'un tel ensemble se mesure par le total beam-on time et le total setup time. Dans notre étude, nous nous intéressons à la minimisation de ces critères, d'un point de vue algorithmique, pour de nouvelles technologies de MLC : le MLC rotatif et le MLC à double couche. De plus, nous proposons un algorithme d'approximation pour trouver un ensemble de configurations minimisant le total beam-on time pour le MLC rotatif.

Mots clés : Proton thérapie, photon thérapie, simulateur, mouvements intra-fraction, décomposition de collimateurs multilames.

Résumé français de la thèse

La radiation thérapie est un des traitements contre le cancer le plus utilisé. Ce type de traitement peut être délivré de différentes façons. Dans cette thèse nous nous intéressons à une technique couramment utilisée appelée la photon thérapie ainsi qu'à la proton thérapie qui reste peu utilisée mais qui suscite de plus en plus d'intérêt.

En proton thérapie nous nous sommes intéressés au problème du mouvement des patients pendant le traitement. Pour cela, nous avons développé un logiciel visant à reproduire un traitement de proton thérapie délivré à un patient mobile. L'intérêt de ce simulateur est de rendre compte de l'impact du mouvement sur le traitement. D'autre part, il peut être utilisé pour mettre au point des stratégies ayant pour but de réduire l'impact de mouvement.

En marge de ce travail, nous nous sommes intéressés à des problèmes algorithmiques rencontrés en photon thérapie.

Dans une première partie nous introduirons le domaine de la radiation thérapie et plus précisément : la photon thérapie et la proton thérapie. Nous introduirons également des problèmes rencontrés dans ces deux techniques. Dans une seconde partie nous présenterons un logiciel développé pour faciliter l'étude du mouvement en proton thérapie. Enfin nous exposerons les résultats de l'étude algorithmique réalisée en photon thérapie.

Chapitre 1

Radiation thérapie

1.1 Présentation de la radiation thérapie

La radiation thérapie est un traitement médical visant à détruire des cellules cancéreuses à l'aide de radiations ionisantes. Ce traitement est apparu en 1896, peu de temps après la découverte des rayons X par le Dr. Roentgen (1895). Au fil du temps, cette technique a évolué pour donner naissance à différents procédés de radiation thérapie utilisés de nos jours : la curiethérapie, la photon thérapie et la proton thérapie. La curiethérapie, appartenant à la radiation thérapie interne, consiste à insérer une source radioactive dans le patient afin de traiter la tumeur en plaçant cette source dans la tumeur ou à proximité de cette dernière. La photon thérapie, appartenant à la radiation thérapie externe (voir Figure 1.1), utilise un rayon à base de photons, dont l'énergie est supérieure à 100 keV, et dont la source, située à l'extérieur du patient, est orientée vers la tumeur. La proton thérapie, appartenant également à la radiation thérapie externe, utilise un rayon de protons, dont l'énergie est située entre 30 et 230 MeV. Son principe est similaire à celui de la photon thérapie pour traiter un patient. Dans le cadre de cette thèse nous nous intéresserons à la photon thérapie et à la proton thérapie.

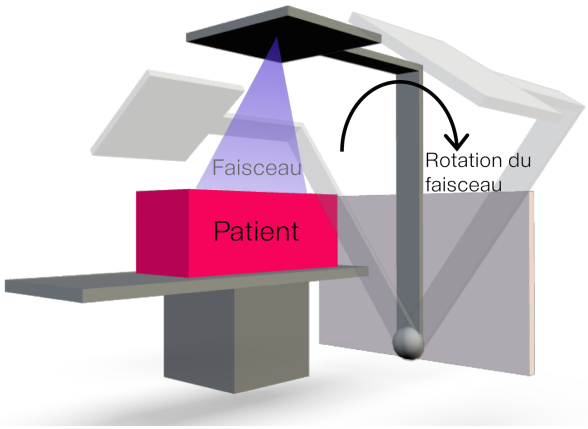

FIGURE 1.1 – Illustration de la radiation thérapie externe : le faisceau de radiations ionisantes est externe au patient et peut tourner autour de ce dernier.

1.2 Comparaison entre la photon et la proton thérapie

De nos jours, la photon thérapie est un des traitements les plus utilisés pour traiter les cancers. La proton thérapie suscite de plus en plus d'intérêt de par le monde en raison des bénéfices que cette technique apporte aux patients par rapport à la photon thérapie. En effet, la différence majeure entre ces deux techniques est la quantité d'énergie déposée dans le corps du patient, appelée *dose* et mesurée en Gray (Gy), ainsi que sa répartition. Il est nécessaire de savoir que lors d'un traitement, on cherche à déposer une dose très importante au niveau de la tumeur, afin de tuer les cellules cancéreuses, et de limiter autant que possible la dose reçue par les tissus sains dont les organes particulièrement sensibles aux radiations appelés *organes à risque* (OAR). Limiter la dose reçue par les cellules saines est important afin de ne pas risquer de les tuer ou d'engendrer une dégénérescence de ces cellules qui pourrait conduire à des tumeurs dites secondaires dont l'apparition peut se produire à la suite d'un traitement à base de radiations. En photon thérapie le maximum de dose est déposé rapidement après la pénétration du rayon dans le patient, et la dose déposée décroît progressivement sans devenir nulle en traversant le corps du patient. En proton thérapie, le maximum de dose est déposé à une certaine profondeur, appelée profondeur du pic de Bragg (Bragg Peak) dépendant de l'énergie des protons. En aval de cette profondeur la dose déposée devient nulle. En amont de cette profondeur, la dose déposée est relativement faible. Si le rayon de protons contient des protons de différentes énergies (rayon poly-énergétique), il est possible d'observer plusieurs pics de Bragg, qui permettent de déposer une forte dose dans une épaisseur de tissus définie, appelée la région cible. La Figure 1.2, présente un schéma de la dose déposée par des photons et des protons en fonction de la profondeur dans un certain milieu. La Figure 1.3, présente la dose reçue par un patient par des rayons de photons et de protons.

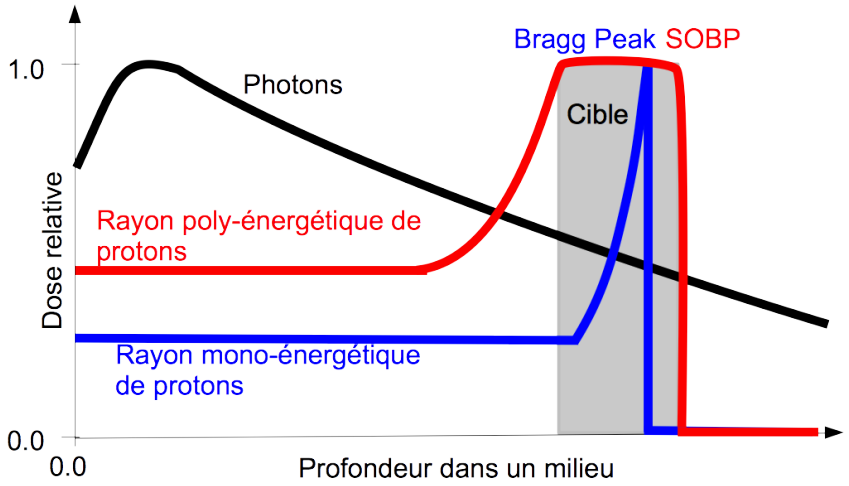

FIGURE 1.2 – Profils de dose pour des photons et des protons.

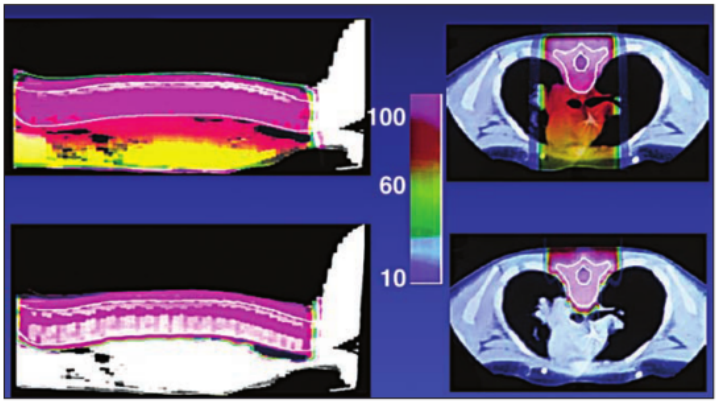

FIGURE 1.3 – Comparaison de la dose déposée dans un patient pour des photons (haut) et des protons (bas). [Kirsch and Tarbell, 2004]

Comme il est possible de le constater, l'utilisation de protons réduit considérablement la dose reçue par le patient. Malgré cela, la proton thérapie n'est pas encore très utilisée dans le monde. En effet, en Août 2013, seulement 43 centres de proton thérapie étaient recensés dans le monde, ce qui correspond à 122 salles de traitement. Cela représente 0.9% des centres de photon thérapie [Goethals and Zimmermann, 2013]. Le principal facteur limitant le développement de la proton thérapie est le coût : environ 95 millions d'euros (≈ $130 millions) pour un centre de proton thérapie et environ 23 millions d'euros (≈ $30 millions) pour un centre de photon thérapie. De plus, le traitement d'un patient nécessite plusieurs séances d'irradiation, appelées *fractions*, dont le coût est d'environ 740 euros (≈ $1000) pour la proton thérapie et d'environ 230 euros (≈ $300) pour la photon thérapie [Peeters et al., 2010]. Petit à petit les entreprises de proton thérapie améliorent les technologies pour les rendre moins onéreuses. Il est estimé que d'ici 2030 le nombre de salles de traitement atteindra 1000 [Goethals and Zimmermann, 2013].

1.3 Des challenges en radiation thérapie

La photon thérapie est délivrée à l'aide d'un large faisceau de photons tournant autour du patient et auquel une forme est donnée afin de correspondre aux contours de la tumeur, à la dose minimale que doit recevoir la tumeur et la dose maximale qui ne doit pas être dépassée pour les OARs. Cette conformation, en 2 dimensions, est accomplie à l'aide d'un collimateur multilames (MLC). Un MLC est composé de paires de lames parallèles pouvant bloquer ou laisser passer le faisceau (voir Figure 1.4). La planification du traitement consiste à définir une grille en 2 dimensions de la dose qui doit être délivrée localement au patient pour chaque angle du faisceau. Cette grille, appelée plan d'intensité, est réalisée par une séquence de configurations du MLC. Bien que la qualité d'un plan de traitement soit jugée par des paramètres dosimétriques, deux critères permettent d'évaluer son efficacité. Le premier critère, appelé *total beam-on time*, correspond à la durée totale de l'irradiation du patient. Il est égal à la somme de la durée de chaque configuration du MLC. Le second critère, appelé *total setup time*, représente le temps nécessaire pour positionner les lames du MLC pour l'ensemble des configurations. Il est approximativement proportionnel au nombre de configurations. L'enjeu est de minimiser ces deux critères afin d'avoir un

plan efficace et de s'assurer que le patient ne reçoit pas des radiations superflues ou un traitement prolongé inutilement.

(a) Vue d'un Multileaf Collimator (MLC) dans le système utilisé pour délivrer le traitement.

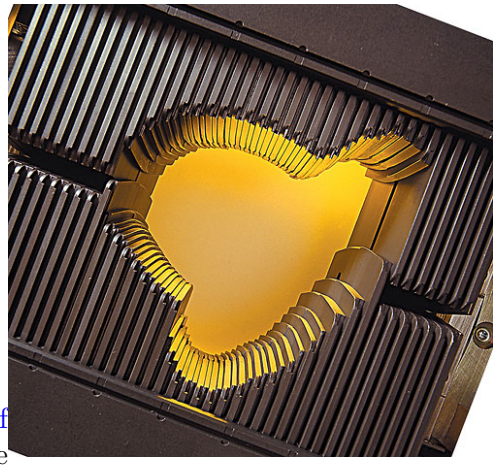

(b) Une configuration de MLC

FIGURE 1.4 – Exemples de MLCs

Un traitement de proton thérapie peut être délivré principalement de deux façons : la technique de *diffusion* ou la technique de *balayage*. La technique de diffusion est similaire au procédé utilisé pour la photon thérapie, c'est à dire qu'un large faisceau est conformé pour correspondre à la forme de la tumeur. Cette technique, très employée de nos jours, commence à laisser place à la technique de balayage qui permet une meilleure précision pour irradier la tumeur et limiter les radiations inutiles reçues par le patient. Ce procédé emploie un faisceau mono-énergétique de protons très fin (de l'ordre des quelques millimètres) qui est balayé sur l'ensemble de la tumeur. Le changement d'énergie des protons, au cours du traitement, permet de modifier la profondeur où a lieu le balayage dans le patient en raison du pic de Bragg (voir Figure 1.5). Cette seconde méthode, bien que très précise, est très sensible aux mouvements du patient pendant l'irradiation. Ces mouvements, qualifiés d'*intra-fraction*, peuvent être d'origines différentes comme par exemple : respiration, battements du cœur, toux, gaz intestinaux, ou le hoquet. Ces mouvements, peuvent entraîner de fortes dégradations de la dose reçue par le patient. La Figure 1.6 présente un exemple d'irradiation avec et sans mouvement.

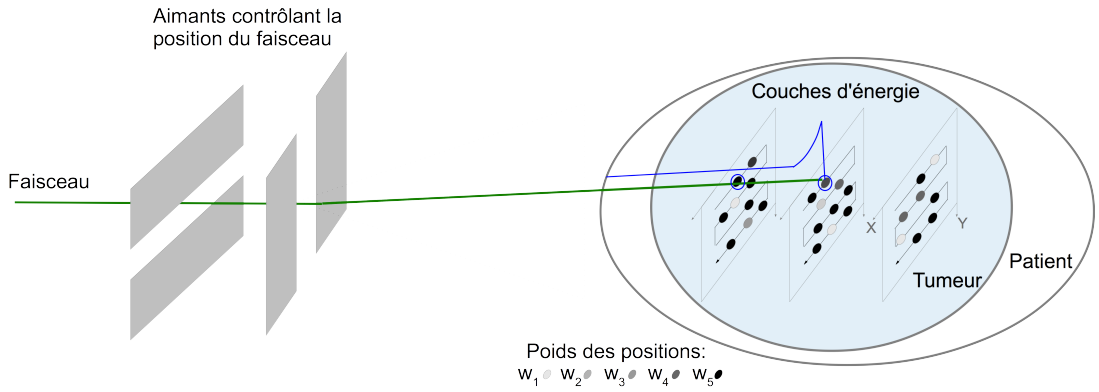

FIGURE 1.5 – Illustration de la technique de balayage. Pour chaque énergie du faisceau de protons définie dans le plan de traitement correspond une position du pic de Bragg (courbe bleue). Une couche d'énergie correspond à l'ensemble des points situés à la profondeur du pic de Bragg. La position du faisceau est contrôlée par un jeu d'aimants. A une énergie et une position de faisceau correspond un *poids* qui représente la durée pendant laquelle l'irradiation de ce faisceau est maintenue.

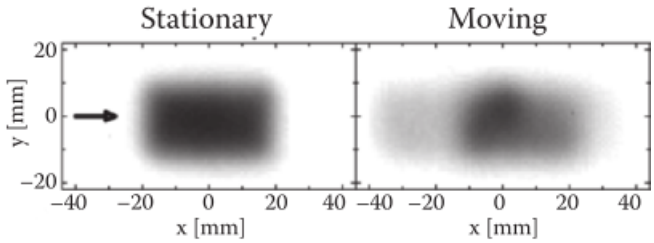

FIGURE 1.6 – Résultat de l'irradiation d'une plaque radiographique avec (droite) et sans (gauche) mouvements. [Paganetti et al., 2012]

Dans le cadre de cette thèse nous aborderons le problème de minimisation des critères d'efficacité rencontrés en photon thérapie et le problème de mouvements intra-fraction en proton thérapie.

Chapitre 2

MSPT : Un simulateur de mouvement pour la proton thérapie

2.1 Développement d'un outil pour l'étude des mouvements intra-fraction.

Afin d'étudier le problème de mouvements intra-fraction en proton thérapie nous avons développé un logiciel, appelé `MSPT` ("Motion Simulator for Proton Therapy"). Ce simulateur est "open source" et distribué sous la licence GNU GPL (v3). Le code source, la documentation et le manuel utilisateur peuvent être obtenus à http://code.google.com/p/mspt/.

Le but principal de cet outil est de rendre compte de la répartition de dose dans le patient lors de mouvements intra-fraction pour un plan de traitement et un certain mouvement. Le second intérêt de `MSPT` est de fournir à l'utilisateur des informations permettant de comparer différents plans de traitement afin de pouvoir améliorer la robustesse du traitement pour ce patient vis à vis des mouvements intra-fraction. Une technique de compensation de mouvement est également mise en œuvre dans `MSPT`, afin de proposer une stratégie visant à améliorer la robustesse des traitements en présence de mouvements intra-fraction.

Ce simulateur a été développé en Python 2.7 et utilise des sous-routines en C pour améliorer la vitesse de traitement de certaines opérations. Il reçoit en entrée l'image CT (Computed Tomography) du patient, le plan de traitement (énergies des protons, positions du faisceau pour le balayage et le *poids* de chaque position qui est équivalent à une durée), le contour des structures du patient (délimitation du corps du patient, d'organes et de la tumeur - voir Figure 2.1) et optionnellement la répartition de dose simulée dans un logiciel de planification de traitement. Toutes ces entrées utilisent le standard DICOM (Digital Imaging and Communication in Medicine). En outre l'utilisateur fournit un fichier de paramétrage du simulateur qui définit son comportement ainsi que les mouvements du patient. `MSPT` fournit à la fin de la simulation un ensemble de données permettant d'évaluer la qualité du traitement aussi bien visuellement que quantitativement (voir exemple dans la Figure 2.2).

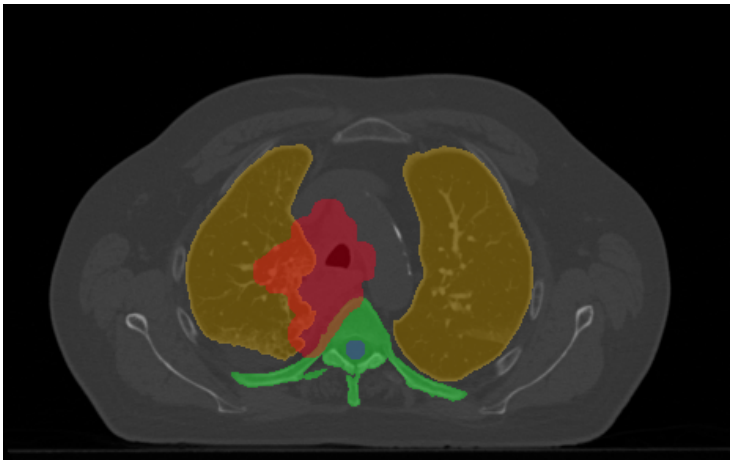

FIGURE 2.1 – Exemple d'une image CT et de la représentation de différentes structures du patient : poumons (orange), région cible comprenant la tumeur (rouge), moelle épinière (bleu) et des os de la colonne vertébrale (vert).

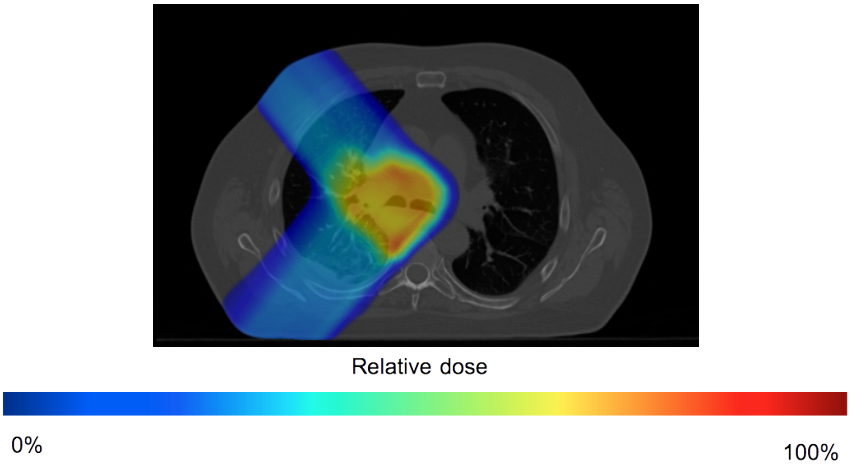

FIGURE 2.2 – Exemple d'une image CT et de la représentation de la répartition de dose simulée dans `MSPT`.

2.2 Modélisation

Le patient est représenté par des matrices 3D obtenues à l'aide du CT. Plusieurs matrices sont utilisées pour représenter la densité des tissus, leur pouvoir d'arrêt, la profondeur radiologique ainsi que le dose déposée. Pour calculer la dose déposée nous utilisons le modèle analytique proposé par Hong et al. [1996]. Ce modèle repose sur un calcul dans l'eau mis à l'échelle pour correspondre à d'autres milieux. Nous avons dû ajouter à ce modèle un facteur de correction de dose dépendant de l'énergie et un facteur de correction de pouvoir d'arrêt dépendant de la densité afin de pouvoir faire correspondre la dose calculée dans `MSPT` à celle obtenue par un autre logiciel utilisé comme référence dans notre

étude.

Le traitement est simulé suivant le plan de traitement fourni par l'utilisateur. Ce plan de traitement définit les angles du faisceau, autour du patient, utilisés pour l'irradiation. Pour chaque angle du traitement, `MSPT` utilise les énergies, les positions du faisceau et leur poids. Afin de correspondre aux informations spatiales du plan nous utilisons les systèmes de coordonnées associés à l'image CT et au plan de traitement (systèmes de coordonnées *IEC fixed* et *IEC gantry*). Afin de représenter l'évolution de la répartition de dose dans le patient en fonction du temps, chaque poids est divisé en durées unitaires pendant lesquelles le patient est considéré comme statique. Par exemple, si le poids correspond à une durée de 10 ms et que la durée unitaire est de 1 ms, le poids est divisé en 10 durées unitaires. Au début de chaque durée unitaire la position du patient ainsi que sa modélisation sont mises à jour afin de calculer la dose reçue pendant la durée unitaire.

Les mouvements sont simulés à l'aide d'une transformation rigide du corps du patient. Ils sont définis par des fonctions dépendant du temps. Dans le cadre de notre travail nous avons utilisé un modèle de respiration [Lujan et al., 1999] basé sur une fonction cosinus. Nous avons ajouté la possibilité de faire varier aléatoirement l'amplitude et la période de la respiration en utilisant des variables aléatoires configurables par l'utilisateur.

2.3 Evaluation du simulateur

Afin d'évaluer le calcul de dose effectué par `MSPT`, nous avons comparé la dose simulée par notre simulateur, à celle calculée par le modèle *ProtonMachine* d'un logiciel commercial de planification de traitement : RayStation (RaySearch Laboratories). Nous avons tout d'abord effectué des simulations de faisceaux mono-énergétiques dans un volume d'eau pour différentes énergies entre 30 MeV et 230 MeV. Ces simulations ont montré une très bonne concordance entre `MSPT` et *ProtonMachine* (voir Figure 2.3).

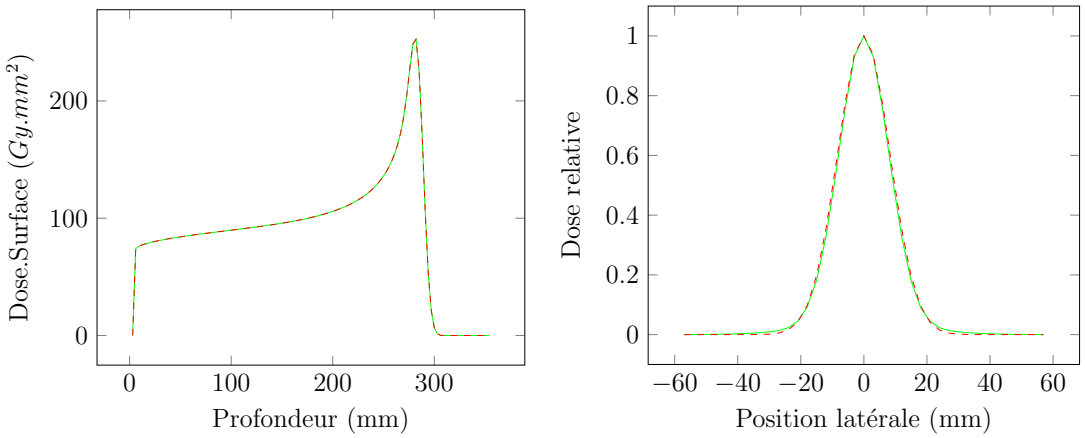

FIGURE 2.3 – Graphiques représentant la dose en fonction de la profondeur (gauche) et le profil latéral (droite) de la répartition de dose d'un faisceau de protons de 210MeV dans l'eau avec *ProtonMachine* (vert) et `MSPT` (rouge).

Nous avons ensuite évalué le calcul de dose sur des cas de patients. Les résultats ont montré une bonne cohérence (voir Figure 2.4) malgré l'apparition d'artefacts systémiques dans les différents cas utilisés. Ces artefacts situés sur l'extrémité distale de la tumeur présentent une région de sur-dose (points chauds), le long du contour de la tumeur et une région sous-dosée (points froids) après la tumeur (voir Figure 2.5). La cause de cet artefact n'a pas pu être mise en évidence mais pourrait venir de différences dans le calcul de la profondeur radiologique *ProtonMachine* et `MSPT`.

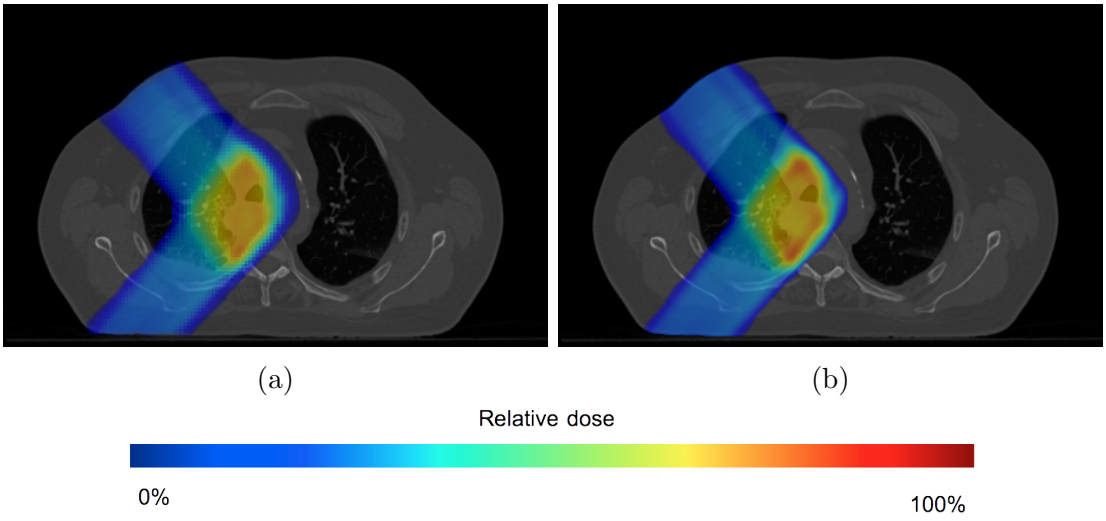

FIGURE 2.4 – Distribution de dose simulée pour un patient dans *ProtonMachine* (2.4a) et dans `MSPT` (2.4b).

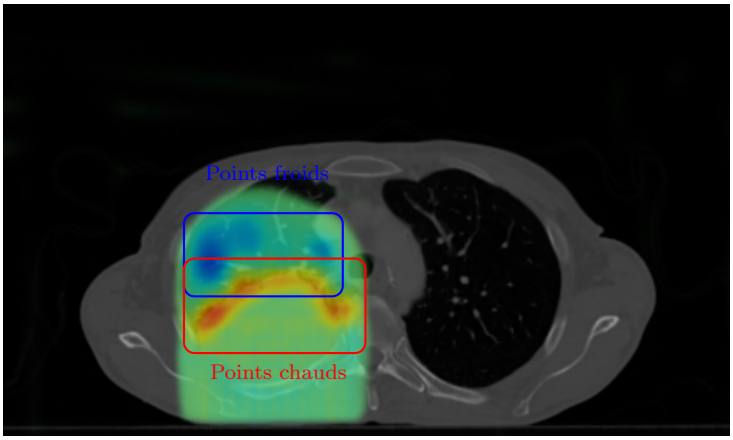

FIGURE 2.5 – Points chauds et points froids (respectivement situés par les rectangles rouge et bleu).

Nous avons enfin utilisé le simulateur pour rendre compte de la dégradation de la dose reçue par le patient lors de mouvements intra-fraction (voir Figure 2.6). Cette dégradation se traduit par une irradiation réduite de la région de la tumeur, une irradiation accentuée

dans les OARs et l'apparition de points chauds et de points froids.

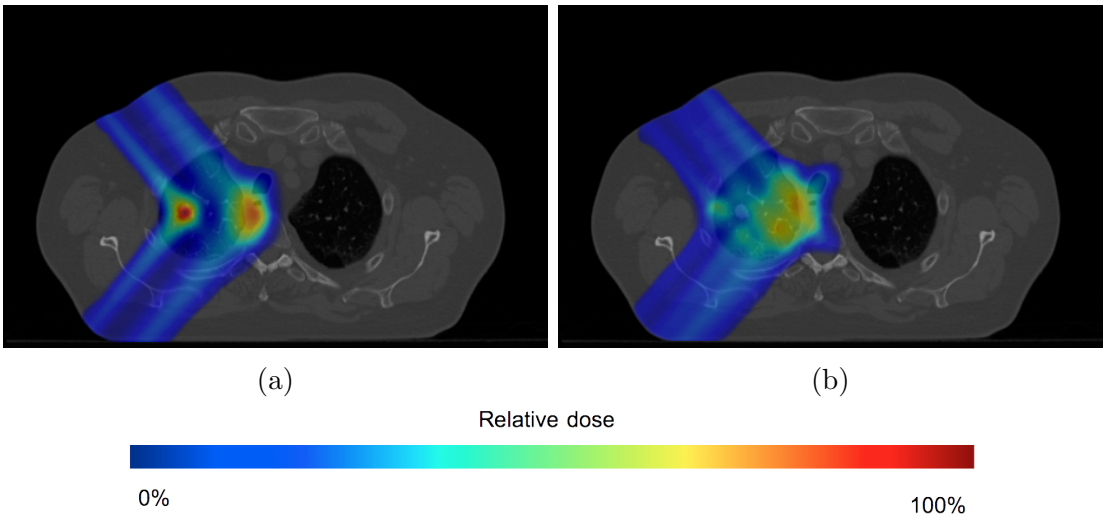

FIGURE 2.6 – Distributions de dose calculées pour un patient statique (2.6a) et un patient mobile (2.6b) dans `MSPT`.

2.4 Compensation du mouvement

Enfin, nous proposons une nouvelle approche de compensation de mouvement basée sur l'adaptation du poids de chaque faisceau en fonction du mouvement et sur la posibilité de balayer plusieurs fois un même position pour une énergie donnée. Le travail effectué correspond à une étude préliminaire de cette stratégie afin de mettre en avant les intérêts et les limites.

Considérons un plan de traitement pour lequel les positions du faisceau de protons d'énergie E_n sont représentées par les couples (b_i, w_i) ordonnés suivant l'indice i. b_i correspond aux coordonnées de la position du faisceau et w_i son poids. Ce plan de traitement engendre l'irradiation de l'ensemble des (P_i), correspondant aux points cibles des positions (b_i, w_i) (la position (b_k, w_k) irradie le point (P_k) pour un patient statique) du faisceau, situés dans le patient sur la couche d'énergie associée à E_n (ensemble des points situés à la distance d_{BP} de la source du faisceau, où d_{BP} correspond à la profondeur du pic de Bragg).On considère que (P_i) est irradié par le faisceau $(t = i, w = w_i)$ où t correspond à la date d'irradiation définie par l'ordre des positions du faisceau et w correspond au poids du faisceau. La stratégie de compensation consiste à changer w de telle sorte qu'à $t = i$, w soit fixé à w_k afin d'irradier le point (P_k) le point cible du faisceau à $t = i$ en raison du mouvement défini par le vecteur $v(t)$ situé dans le plan perpendiculaire au faisceau. La Figure 2.7 illustre ce principe.

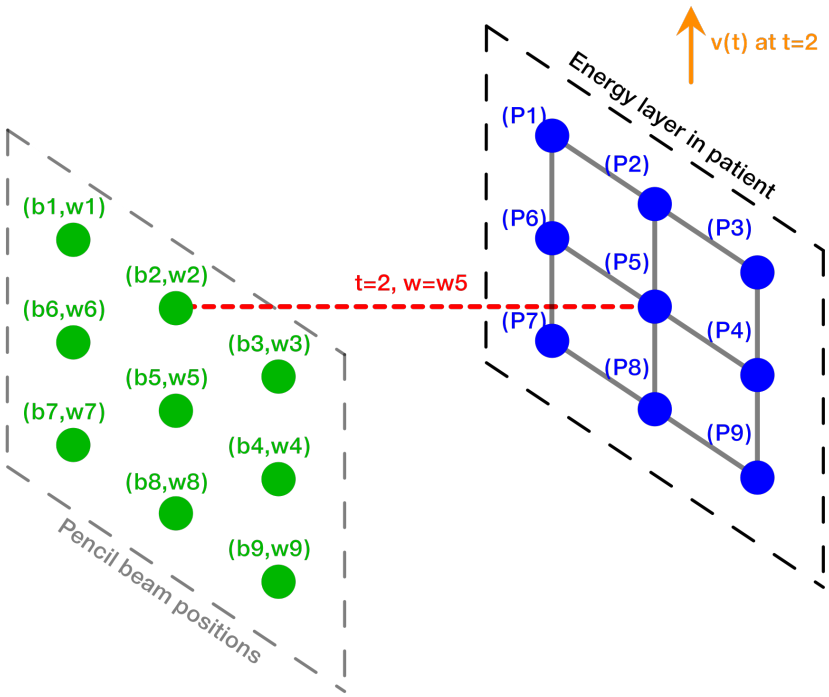

FIGURE 2.7 – Illustration du traitement, pour un patient mobile, utilisant la technique de compensation. Les positions du faisceau sont représentées en vert, le faisceau en rouge, les points cibles en bleu et le vecteur de déplacement du patient (2D) en orange.

L'évaluation de cette méthode nous a permis de montrer qu'elle réduit fortement l'impact du mouvement sur la répartition de dose dans le patient. Les erreurs de répartition de dose obtenues, par rapport à la répartition dans un patient statique, sont très faibles (inférieures à 5%) et le critère indiquant que 95% du volume de la tumeur reçoit au moins 95% de la dose prescrite est rempli. Par conséquent, les erreurs peuvent être considérées comme cliniquement acceptables. La Figure 2.8 correspond aux courbes représentant le volume relatif de la tumeur et d'OARs, recevant au moins une certaine dose, appelées DVHs (Dose Volume Histogram). Ces DVHs sont obtenus pour un patient statique et un patient mobile avec et sans la technique de compensation. Les distributions de dose correspondantes sont représentées avec une image CT dans la Figure 2.9. Notre stratégie permet pour le moment de compenser seulement des mouvements 2D perpendiculaires au faisceau. Un développement en 3D pourrait donc faire partie de futurs travaux de recherches et d'améliorations. De plus, les mouvements simulés n'étant basés que sur une transformation rigide du corps du patient, une future étude pourrait porter sur la compensation des mouvements présentée pour des transformations déformables.

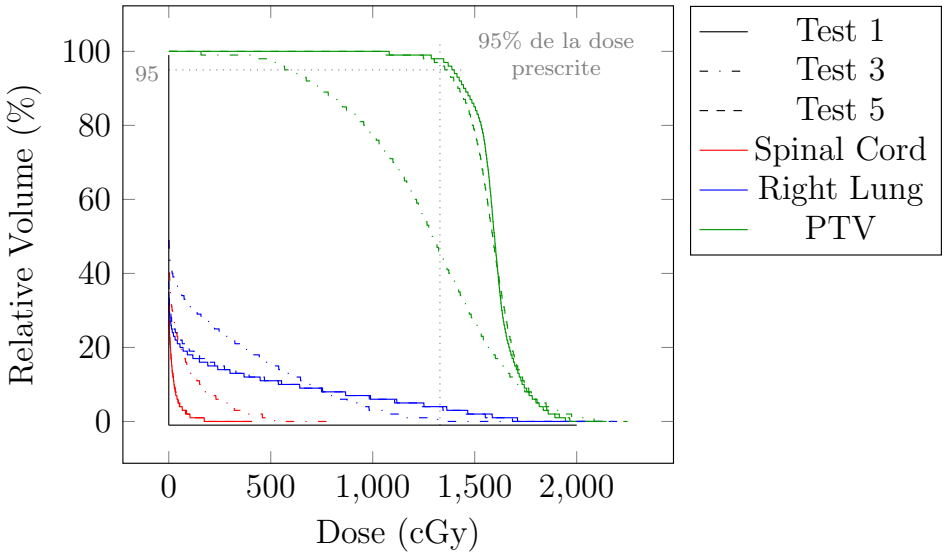

FIGURE 2.8 – Comparaison des DVHs pour un traitement délivré à un patient statique (Test 1) et à un patient mobile avec (Test 5) et sans (Test 3) compensation pour un mouvement de 1.5 cm d'amplitude. Les structures du patient considérées sont la tumeur (PTV), le poumon droit (Right Lung) et la moelle épinière (Spinal Cord).

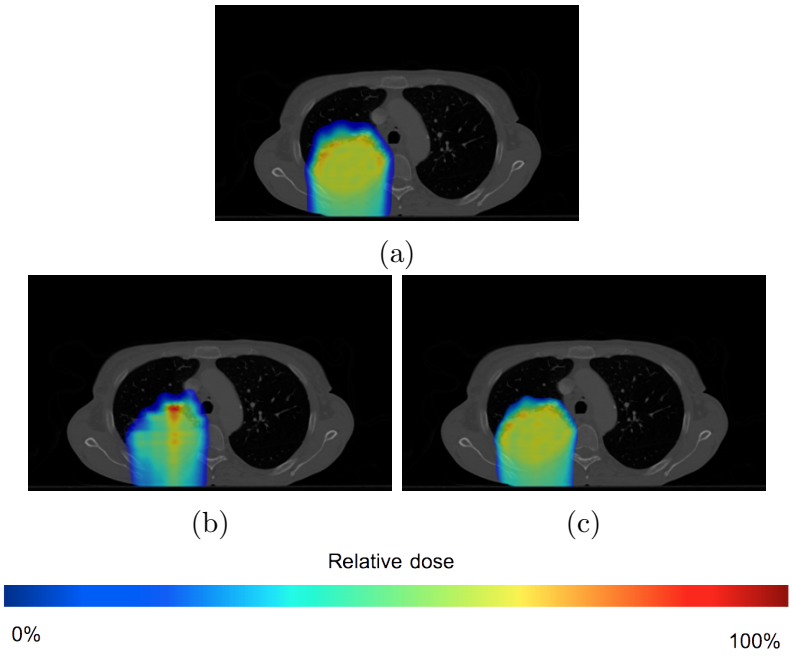

FIGURE 2.9 – Distributions de dose pour un patient statique (2.9a) et un patient mobile sans (2.9b) et avec (2.9c) compensation.

Chapitre 3

Quelques résultats en photon thérapie

3.1 Aspects algorithmiques de la photon thérapie

Comme mentionné précédemment (Section 1.3), en photon thérapie la planification d'un traitement génère des plans d'intensité correspondant à des grilles en 2 dimensions. Par conséquent, chaque grille peut être représentée comme une matrice 2D, appelée matrice d'intensité. Le problème demandant de trouver pour un plan d'intensité l'ensemble des configurations permettant de réaliser ce plan peut alors être considéré comme un problème de décomposition de matrice en matrices binaires. Dans ces matrices binaires, les 0 correspondent aux régions où le MLC bloque le faisceau de photons, et les 1 aux régions où il irradie le patient. Les problèmes de minimisation des critères *total beam-on time* et *total setup time* peuvent alors correspondre, respectivement, à des contraintes de minimisation du nombre de matrices binaires et de minimisation de la somme des coefficient des matrices binaires. Ces coefficients sont appelés *poids*.

3.2 Précédents résultats algorithmiques

De précédents travaux sur le MLC conventionnel ont montré que le problème de minimisation du *total beam-on time* peut être résolu en temps linéaire [Ahuja and Hamacher, 2005].

Burkard [2002] a prouvé que le problème de minimisation du *total setup time* est NP-Difficile pour les matrices d'intensité ayant au moins 2 lignes. Ce résultat a été renforcé par Baatar et al. [2005] qui ont montré que ce problème reste NP-Difficile même pour les matrices à 1 ligne.

3.3 Résultats algorithmiques pour de nouveaux MLCs

Dans le cadre de ce travail nous nous sommes intéressés à deux nouvelles technologies de MLC : le MLC rotatif, dans lequel des rotations de 90° sont autorisées entre 2 configurations et le MLC double couche, correspondant à deux couches de paires de lames perpendiculaires entre elles (voir Figure 3.1).

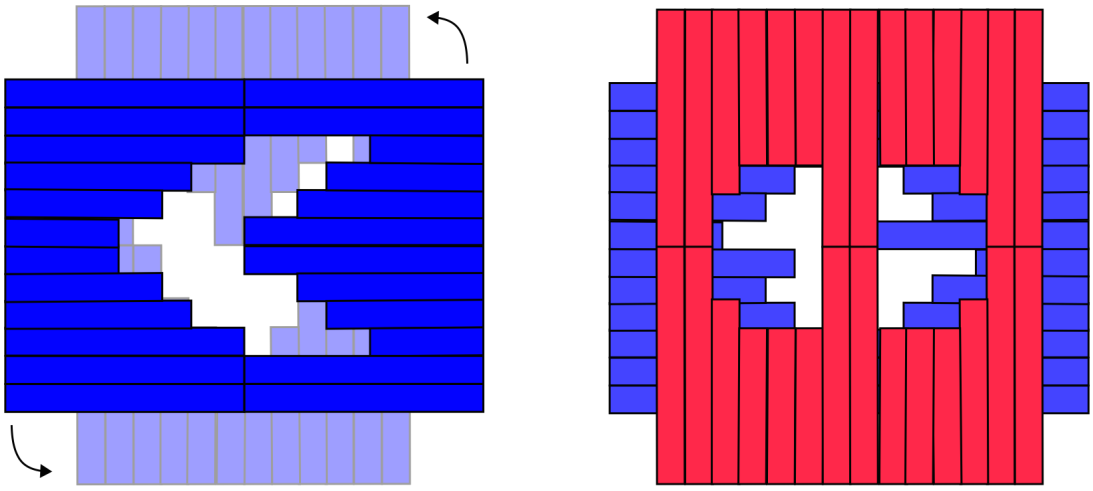

FIGURE 3.1 – Schémas d'un MLC rotatif (gauche) et d'un MLC à double couche (droite).

Dans une première partie de l'étude nous avons démontré que le problème de décomposition dans le cas d'un MLC à double couche est NP-Difficile lorsque l'on cherche à minimiser le critère *total setup time*. Ensuite, nous avons démontré que le problème de décomposition dans le cas d'un MLC rotatif est également NP-Difficile lorsque l'on cherche à minimiser les critères *total setup time* et *beam on time*. De plus, nous proposons un algorithme d'approximation en temps polynomial permettant de fournir une solution entière au problème de décomposition pour un MLC rotatif minimisant le *beam on time*. Cet algorithme consiste à chercher dans un premier temps une solution optimale continue où les poids des matrices sont des valeurs réelles positives (la contrainte de valeurs entières est relaxée). Les poids des configurations horizontales sont ensuite arrondis afin d'avoir une solution entière pour ces configurations. La soustraction de cette solution horizontale à la matrice d'intensité initiale correspond à la matrice d'intensité à décomposer en utilisant des configurations verticales du MLC. Cette décomposition utilisant des valeurs entières est réalisable en temps linéaire ([Ahuja and Hamacher, 2005]). La solution entière verticale nous permet ainsi d'obtenir une solution entière, pour le problème de décomposition utilisant un MLC rotatif, garantissant une bonne approximation qui est au plus à $2m$ de la solution optimale continue où m correspond au nombre de paires de lames du MLC.

Chapitre 4

Conclusion

Au cours de cette thèse, nous nous sommes intéressés au domaine de la radiation thérapie. Nous avons principalement travaillé au développement d'un simulateur de mouvement pour la proton thérapie utilisant la technique de balayage. Le but de ce simulateur est de fournir un outil permettant de rendre compte de l'impact de mouvements intra-fraction sur le traitement reçu par le patient. Un intérêt de ce simulateur est de pouvoir comparer des plans de traitement afin de trouver celui qui est le plus robuste à ces mouvements. De plus, il permet d'étudier des méthodes de réduction de l'impact du mouvement comme celle que nous proposons afin d'améliorer la qualité des traitements et de les rendre moins sensibles aux mouvements intra-fraction. Enfin, nous nous sommes intéressés au problème de configurations des MLCs pour de nouvelles technologies basées sur une double couche de MLCs et un MLC rotatif. Nous avons montré que trouver une séquence de configurations, pour ces deux types de MLCs, minimisant le *total beam on time* et/ou le *total setup time* est NP-Difficile. Cependant nous proposons un algorithme d'approximation pour résoudre le problème de minimisation du *total beam on time* dans le cas d'un MLC rotatif.

Ces différents travaux nous ont permis d'une part de rendre accessible un logiciel amené à évoluer pour permettre d'autres études visant à améliorer la qualité des traitements de proton thérapie en cas de mouvements intra-fraction. D'autre part ils ont permis d'étudier une nouvelle approche pour compenser ces mouvements et ainsi rendre les traitements plus robustes. Enfin, l'étude du séquençage de nouveaux types de MLCs nous a permis de mettre en avant aussi bien les problèmes algorithmiques qu'ils soulèvent pour de futures recherches, que l'intérêt de leur utilisation.

Foreword

My PhD studies started in September 2011. After working in computer science applied to medical imaging during one year at Casilab (University of North Carolina, Chapel Hill, USA), one year and a half at Imaging Informatics (University of Calgary, Canada) and obtaining a master's degree from CPE-Lyon (Chimie Physique Electronique, Lyon, France) in computer science, I decided to pursue my studies with a PhD applied to the field of medicine. Indeed, this field is really motivating since computer science can provide advanced tools and information to doctors and to medical personnel to diagnose, treat and cure patients. This is how I came to choose this PhD thesis related to the use of computer science in radiation therapy in the *AlgoB* team of the LIGM (Laboratoire d'Informatique Gaspard Monge) at the Université Paris-Est Marne La Vallée (France).

This PhD thesis falls within the ANR BIRDS [1] (Agence Nationale de la Recherche - BIological networks, RaDiotherapy and Structures) project. This project encompasses 3 distinct tasks. The first and second tasks dedicated to the study of algorithmic in the field of algorithmic structures and in the field of biological networks, which are the main topics of research in the *AlgoB* team. The third task aims at exploring new areas of research, for the team, where algorithmic and computer science could lead to improvements, and more specifically in radiation therapy. Initially, this third task focused on an algorithmic study of a specific device called Multi-Leaf Collimator (MLC) used in photon therapy, a sub-field of radiation therapy (also known as radiotherapy). With this aim in mind, Dr. Guillaume Blin, in charge of this project, started collaborating with Dr. Xiaodong Wu and the department of Radiation Oncology at the University of Iowa (Iowa, USA) in February 2011. After the beginning of my PhD, thanks to this collaboration we started to realize that the proton therapy, another technique of radiation therapy could offer interesting problems that could be addressed with computer science, such as the patient motions during the treatment delivery. Therefore, we broaden the study of radiation therapy, not only to photon therapy, but also to proton therapy. This collaboration allowed me to build and improve my knowledge in radiation therapy from a physical and a clinical point of view.

1. http://igm.univ-mlv.fr/AlgoB/BIRDS/

Contents

Table of Contents

List of Tables

List of Figures

Glossary

Glossary

CT Number

CT Number is a value assigned to a voxel in a CT image. This value is based on the Hounsfield Unit. CT numbers for air, water and compact bone are respectively -1000HU, 0HU, and +1000HU.

Gray

Unit representing the absorbed dose by a medium for ionizing radiation. One gray is the absorption of one joule of energy, per kilogram of matter:
$1Gy = 1\frac{J}{kg}$.

Hounsfield Unit

Unit to scale the linear attenuation coefficient of a medium compared to the linear attenuation coefficient of water:
$HU = 1000 \times \frac{\mu_X - \mu_{Water}}{\mu_{Water}}$, where μ_X is the linear attenuation coefficient (m^{-1}) of the medium X, depending on the atomic number, the mass density and the photon energy.

Mega-electron Volt

1 MeV is equal to $1.60217657 \times 10^{-13}$ Joules. It corresponds to the energy gained or lost by the charge of 10^6 electrons moving across an electric potential difference of 1 Volt.

Stereotactic Body Radiation Therapy

Stereotactic Body Radiation Therapy is a treatment procedure involving high dose fractions.

Computed Tomography

Computed tomography is an anatomical imaging technique using X-rays (photons) that allows the acquisition of a 3D image of a patient. It provides especially a good rendering of dense tissues such as bones.

Dose-Volume Histogram

A dose-volume histogram is a 2D plot representing the percentage of volume receiving a certain amount of dose.

Magnetic Resonance Imaging

Magnetic Resonance Imaging is an anatomical imaging technique using variable magnetic fields that allows the acquisition of a 3D image of a patient. It provides especially a good rendering of soft tissues such as ligaments.

Positron Emission Tomography

Positron Emission Tomography is a functional imaging technique using the detection of pairs of gamma-rays produced indirectly by a positron-emitting radioisotope injected in the patient bloodstream. This technique allows a 3D acquisition of the biological activity of a patient.

Single Photon Emission Computed Tomography

Single Photon Emission Computed Tomography is a functional imaging technique using gamma rays obtained by injecting a radioisotope in the patient bloodstream. This technique allows a 3D acquisition of the biological activity of a patient.

Treatment Planning System

Software used to plan and optimize a treatment plan.

Radiological Depth

The radiological depth at point P in a medium is the thickness of water having the same effect on the particle energy as the thickness from the beam's entrance into the medium to a given point P .

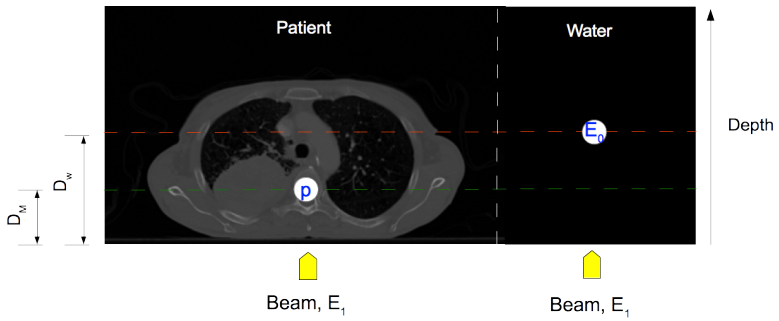

Let's consider a beam of energy E_1 entering into a patient body. At point P located at a depth D_M, the beam's energy drops to E_0. In water, a beam entering with the energy E_1, will loose some energy and reach E_0 at depth D_W. Hence, the radiological depth at P is D_W.

Voxel

Volume element representing the resolution of a 3D matrix.

Acronyms

2D	2-dimensions.
3D	3-dimensions.
4D	4-dimensions.
CFRT	Conformal Radiation Therapy.
CT	Computed Tomography.
CT#	CT Number.
CTV	Clinical Target Volume.
DICOM	Digital Imaging and Communications in Medicine.
DVH	Dose Volume Histogram.
GTV	Gross Tumor Volume.
Gy	Gray.
HU	Hounsfield Unit.
IEC	International Electrotechnical Commission.
IMRT	Intensity Modulated Radiation Therapy.
linac	Linear Accelerator.
MeV	Mega-electron Volt.
MLC	Multileaf Collimator.
MRI	Magnetic Resonance Imaging.
MU	Monitor Units.
OAR	Organ At Risk.
PET	Positron Emission Tomography.
PRV	Planning organ at Risk Volume.
PTV	Planning Target Volume.
SBRT	Stereotactic Body Radiation Therapy.
SPECT	Single Photon Emission Computed Tomography.
TPS	Treatment Planning System.

Introduction

Radiation therapy is one of the most common cancer treatments. It uses ionizing radiation to kill cells within a tumor. A treatment aims at irradiating with high dose the tumor and at protecting the so-called *organs at risk (OARs)*, which correspond to healthy tissues sensitive to radiation. A treatment can be delivered using different types of radiation: photon-based radiation in the so-called *photon therapy*, and proton-based radiation in the so-called *proton therapy*. Photon therapy is much more used than proton therapy. Indeed, as of August 2013, the number of proton therapy centers represents 1% of the photon therapy centers [Goethals and Zimmermann, 2013]. The main reason for this difference is the cost of such medical centers. However, proton therapy arouses more and more interests due to its advantages in providing an accurate irradiation of the tumor combined with a good sparing of *healthy tissues* and *organs at risk*. It was shown that protons are preferable to photons, in particular, when it comes to treat tumors close to dose-sensitive anatomical structures such as in head-and-neck treatments [Chan and Liebsch, 2008], prostate cancer [Lee et al., 1994] or when it is essential to reduce toxicity to healthy tissues such as in pediatric patients [Fuss et al., 1999], [Clair et al., 2004]. Moreover, it was shown that protons allow a greater tumor control probability and a smaller normal tissue complications probability than photons [Fuss et al., 1999], [Fuss et al., 2000], [Lin et al., 2000]. This is one of the reasons why more and more studies focus on this type of radiation therapy both on the clinical and the physical sides.

In proton therapy, mainly two techniques can be used: the *scattering* and the *spot scanning*. However, we focused on the spot scanning delivery strategy. It consists of a thin proton beam scanned across the tumor volume. It provides a good conformity to complex tumor shapes, which reduces toxicity to healthy tissues. However, this accuracy is greatly degraded when the patient moves during the treatment, which is unavoidable since the patient is alive and the lungs and other organs (*e.g.*, the heart) are constantly in motion. Such motions are called *intra-fraction motions*. The problem of intra-fraction motion has some impact on the overall treatment. The improvement of the treatment's robustness to motion requires the capacity of dose computation on dynamic patient dataset (*i.e.*, a *4-dimensions (4D)* treatment planning). Studies are often conducted with the researcher's in-house treatment planning system or an expensive clinical treatment planning system. The limited availability of 4D treatment planning system makes it difficult to study this subject by a broader category of researchers. This is why we developed an open-source 4D dose computation and evaluation software, `MSPT` (Motion Simulator for Proton Therapy). The main interest of this simulator lies in the ability to render the impact of a predicted patient motion on a prescribed treatment plan. This capability makes it an innovative research tool to evaluate and compare different methods of motion management or mitigation. While the main objective of `MSPT` is to quantify the treatment degradation induced by particular motions, it can also be used to elaborate some compensation methods to improve treatment robustness such as the one we propose.

On the fringe of this work, we tackled algorithmic problems encountered in photon therapy. We focused on the so-called *Intensity Modulated Radiation Therapy (IMRT)* delivery technique using *MLC*. A central problem of this technique requires finding a series of leaves configurations that can be shaped with MLC. From an algorithmic point of view,

this can be considered as a matrix decomposition problem. We analyzed this problem for dual-layer MLCs and rotating MLCs. We propose theoretical results for both types of MLCs and an approximation algorithm for rotating MLCs.

In the first part of this dissertation, we will introduce the field of radiation therapy and more specifically the proton therapy and photon therapy from an historical and a physical point of view. We will also introduce the problems addressed in the rest of this manuscript: intra-fraction motion in proton therapy and MLC decomposition in photon therapy. In a second part, we will present our simulator `MSPT`, developped to study the intra-fraction motion and improve the robustness of treatments as regards to motion. We will also propose a new approach to reduce the impact of intra-fraction motions. Finally, we will present algorithmic results and an approximation algorithm for the MLC decomposition problem.

Part I

Radiation Therapy

Chapter 1

History of the radiation therapy

The history of radiation therapy begins with the discovery of *X-rays* (photons with an energy level approximately between 60 and 100 KeV) in 1895 by Dr. Wilhelm Roentgen [Röntgen, 1896] in Germany. This breakthrough changed the medical world by providing a new non-invasive diagnostic method allowing to see inside a patient in 2-dimensions (2D), thereby giving birth to a new medical specialty: namely, *Radiology*. Figure 1.1 shows the first radiography obtained by Dr. Roentgen.

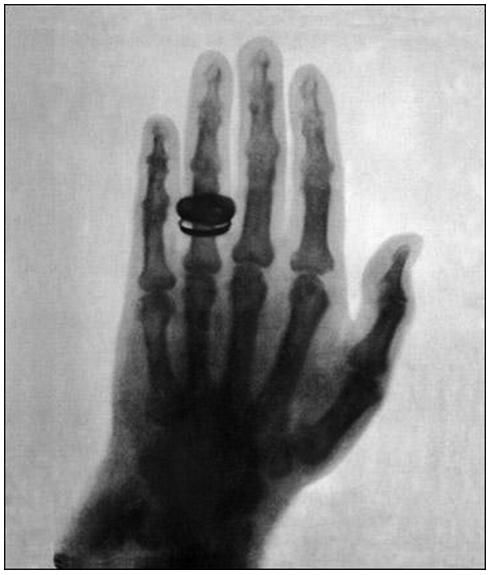

Figure 1.1 – Dr. Roentgen's first X-ray image. The subject was his wife's hand. [Baumrind, 2011]

Soon after, it was observed that exposure to X-rays could damage body tissues and in 1896 a first attempt to treat a breast tumor was performed by Dr. Emil H. Grubbe in Chicago (USA) [Science, 1957; Vujosevic and Bokorov, 2010] using an X-ray machine. It was followed by other attempts such as in 1896 for a stomach cancer by Victor Despeignes in Lyon (France). This was the beginning of a new medical field called *radiation oncology* [Connell and Hellman, 2009] and more specifically *external beam radiation therapy*.

In 1903, Dr. Henri Becquerel, along with Pierre and Marie Curie, won a Nobel Prize in Physics for the discovery of radioactivity. This team was able to isolate the first known radioactive elements, named Polonium and Radium, that naturally emit ionizing radiation. Their research resulted in a new radiation treatment called *brachytherapy* (also known as curietherapy or internal radiation therapy). The treatment, which consists in implanting radioactive seeds within a patient was first used in 1901 by Dr. Henri-Alexandre Danlos in Paris (France) [Gupta, 1995].

In the 1920's-30's the idea of fractionated radiation therapy was introduced. The treatment was divided over the time, instead of a single large exposure, in order to reduce toxicity to healthy tissues in the patient. Nowadays, fractionation is still widely used for all types of radiation therapy techniques [Paganetti et al., 2012].

Early in the development of the radiation therapy, it was recognized that the use of high energy photon beams (greater than a few hundred keV) would provide better outcomes. This technique became known as *photon therapy*. Initially the equipment could not provide such beams, but in 1924 Gustav Ising invented the particle *Linear Accelerator (linac)* concept [Ising, 1924] which was later used by Rolf Wideröe to build a linac in 1928 [Wideröe, 1928]. In 1929, Ernest O. Lawrence designed the cyclotron, a "coiled" linac, inspired by Ising and Wideröe research [Bryant, 2010]. As a result of these inventions, high energy photon beams could be generated, from high energy - for that time - electron beams, but also high energy protons and ion beams (*e.g.*, 1.25Mega-electron Volt (MeV) protons by Lawrence's *cyclotron* in 1932 [Bryant, 2010]). In 1943, Oliphant proposed the *synchrotron* concept [Wilson, 1996] to accelerate charged particles. In 1946, Goward and Barnes made a first demonstration of an 8MeV synchrotron at Woolwich Arsenal (UK). Two months later, Elder, Gurewitsch, Langmuir and Pollock, built a 70MeV synchrotron at the General Electric Laboratory in Schenectady (USA).

In 1946, Robert R. Wilson outlined the importance of protons in radiation therapy [Wilson, 1946] explaining that protons of 125MeV could penetrate body tissues up to a range of 12cm and 27cm for protons of 200MeV. In addition, he demonstrated that the biological damage depends on the density of ionization and that, in the case of protons, this density of ionization increases considerably near the end of the range. In 1954, Ernest O. Lawrence used proton beams to treat a first patient at the Lawrence Berkeley Laboratory in California (USA) [Lawrence, 1957; Paganetti et al., 2012]. This was the beginning of *proton therapy*, another external beam radiation therapy method. Figure 1.2 shows this first patient with Dr. Lawrence.

Figure 1.2 – 1954: First treated patient at Lawrence Berkeley Laboratory.[1]

a. © 2010 The Regents of the University of California, Lawrence Berkeley National Laboratory

In the late 1950's, a new concept arose in radiation therapy: the *Conformal Radiation Therapy (CFRT)*, *i.e.*, making a shape of the radiation field conform to the shape of the target volume in order to minimize the dose received by surrounding healthy tissues while delivering a high dose to the tumor. Soon after, Dr. Takahashi introduced the *Multileaf Collimator (MLC)* device in Nagoya (Japan) [Takahashi et al., 1961; Kobayashi et al., 1996]. Composed of two sets of facing leaves, it could be moved to conform to the radiation field. It was first used in 1963 by Dr. Wanatabe in [Watanabe, 1963; Kobayashi et al., 1996] and has been applied both to photon and proton therapy - it is still in use today.

In 1979, Godfrey N. Hounsfield and Allan M. Cormack where awarded the Nobel Prize in Physics for the invention of the *Computed Tomography (CT)*, a 3-dimensions (3D) imaging technique using X-rays [Peeters et al., 1979; Raju, 1999]. This breakthrough allowed radiation oncologists to shift from 2D to 3D treatment planning and therefore consider a 3D radiation delivery.

In 1982, the concept of *Intensity Modulated Radiation Therapy (IMRT)* was introduced by Brahme and colleagues [Brahme et al., 1982] in 2D. The IMRT consists in considering the "dose distribution" as a "picture" and using the "photon beams" as "pencils" to draw the "picture" by changing the "pencil" thickness, *i.e.*, changing the intensity of photon beams [Webb, 2003]. This concept was also applied to proton therapy and brachytherapy.

In the late 1970's and early 1980's the *spot scanning* (also called beam-scanning) technique was introduced for 3D irradiation in proton therapy [Grunder and Leemann, 1977; Goitein and Chen, 1983; Paganetti et al., 2012]. It consists of using magnets to steer a thin proton (or heavy ion) beam, across the target volume, to control the delivery in 3D. The goal of this method was to replace the use of broad beams that were shaped through a collimator.

In 1991, proton therapy was introduced in France to treat patients at Nice and Orsay.

Nowadays, photon therapy, brachytherapy and proton therapy are still used. While, photon therapy is one of the most common techniques applied in treating cancer, proton therapy is becoming more and more popular (see Section 2.3.1 for more details).

Chapter 2

Principles and physics of radiation therapy techniques

Principle of Radiation Therapy
Radiation therapy is a cancer treatment, based on ionizing radiation aimed at killing the cancerous cells of a tumor.

2.1 External beam radiation therapy

2.1.1 Principle

External beam radiation therapy is a technique where the radiation is delivered from outside the patient. The apparatus delivering the radiation - called the *nozzle* - can be attached to a rotating device called the *gantry*. The gantry rotates around the patient to aim at the tumor from a given angle. In certain therapy centers, the nozzle can also be fixed which precludes any rotation. A particle accelerator is located upstream from the nozzle. Figure 2.1 presents a general example of external beam radiation therapy with a gantry.

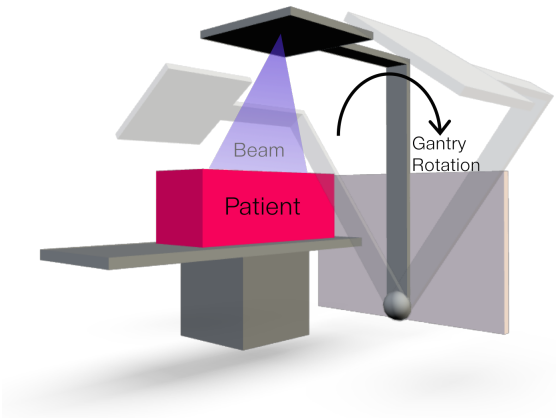

Figure 2.1 – Schematic of an external beam radiation therapy system

External beam radiation therapy techniques include:

- Photon therapy
- Proton therapy
- Heavy ion therapy

Photon beams are generated by accelerating a beam of electrons, through a linac. This beam strikes a target made of metal such as tungsten [Khan, 2010]. Protons (hydrogen ions) and heavy-ions (such as carbon ions) are generated by accelerating these ions in either a cyclotron or a synchrotron or less commonly a linear accelerator.

2.1.2 Particle accelerators

Particle accelerators do just what their name suggests, they accelerate particles (electrons or ions) to an energy level - corresponding to the particle velocity - so that particles can penetrate the body as deeply as possible. Although new ways to accelerate particles, especially for protons and heavy ions, are being investigated (*e.g.*, dielectric wall accelerators or laser driven accelerators [Paganetti et al., 2012]), we will present only the three primary accelerators currently in use.

Linear accelerator

Linear accelerators (linac) increase the speed of particles along a linear beamline. The acceleration is produced by oscillating electric potentials, which create electromagnetic fields, along the beamline. In radiation therapy, linac are generally used to accelerate electrons over a short distance (order of meter) to produce photons and are small enough to be located in the gantry. An example of a linear accelerator in a system used for photon therapy is presented in Figure 2.2.

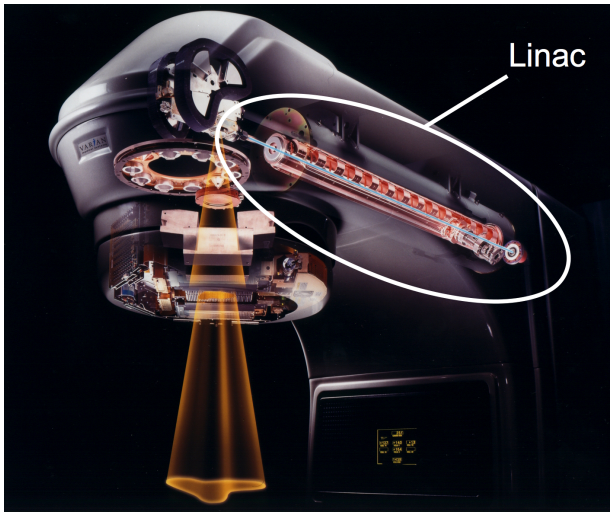

Figure 2.2 – Example of a linac located in a photon therapy gantry. [1]

a. Source: Varian

Cyclotron

Cyclotrons accelerate particles along a spiral path from the center to the outer radius, where the maximum speed is reached, using static magnetic fields perpendicular to a high frequency alternating electric field. A cyclotron provides a continuous particle beam with a fixed energy, *e.g.*, around 250MeV for protons used in radiation therapy. In order to change the beam energy, the extracted particles go through a *degrader*, which slows down the particles to the desired energy, and through a range modulator, made of low-Z materials such as plexiglas, that allow a fine energy tunning before reaching the delivery nozzle. However, going through degraders reduces the intensity of low energy beams. For medical facilities, the diameter of a cyclotron can vary between 3.5m (100 tons) and 5m (200 tons) [Paganetti et al., 2012]. A schematic of a cyclotron and the beamline to the gantry is presented in Figure 2.3.

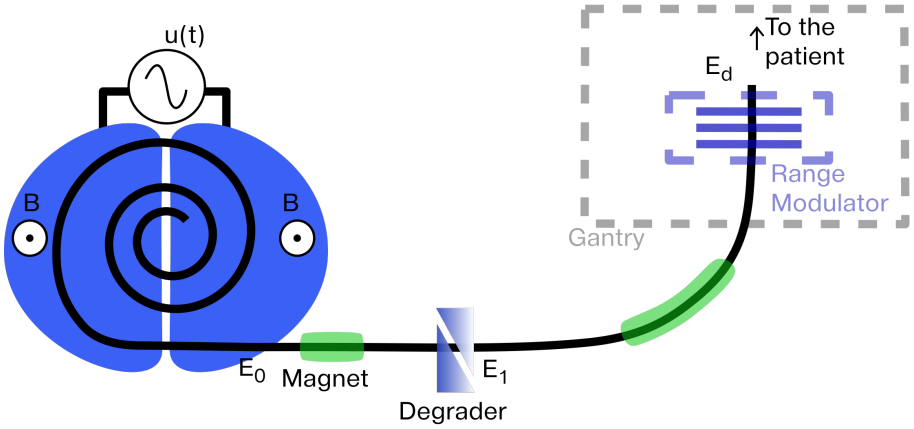

Figure 2.3 – Schematic of a cyclotron and the beamline to the gantry. E_0: energy of protons exiting the synchrotron, E_1: energy after a first tuning by a degrader, E_d: energy used for the delivery after a fine tuning. B and $u(t)$ represent respectively the static magnetic field and the alterning electric field.

Synchrotron

Synchrotons accelerate particles through a circular beamline. The process starts with the injector, an ion source, that fills the synchrotron with a limited quantity of low energy particles - in the order of few MeV[Paganetti et al., 2012]. The particles are then guided through the beamline using time dependent magnetic fields that bend the particle trajectories, and then are accelerated by kicker magnets placed along the beamline. The energy of the resulting beam is related to the number of cycles traveled. Once particles reach the desired energy, a deflector magnet change their trajectory to be extracted and they are conducted to the gantry by electromagnetic beamline. Therefore, a synchrotron accelerates particle beams to a desired energy without degraders. As a result, high and low energy beams have the same intensity (*i.e.*, the same number of protons per time unit). However, for practical reasons in medical treatments, beams are accelerated to different energy levels and a fine tuning is performed in the nozzle. Once the synchrotron spilled all the particles (the spill duration is called the "spill length"), the injection and acceleration processes start again. Hence, the particle production is pulsatile. In medical

applications the spill length is around 5s [Kraus et al., 2011] and the time between two spills is around 2-3s [Smith et al., 2009] for modern synchrotrons.

In medical facilities, synchrotron diameter varies between 6 and 8 meters [Paganetti et al., 2012]. A schematic of a synchrotron is presented in Figure 2.4.

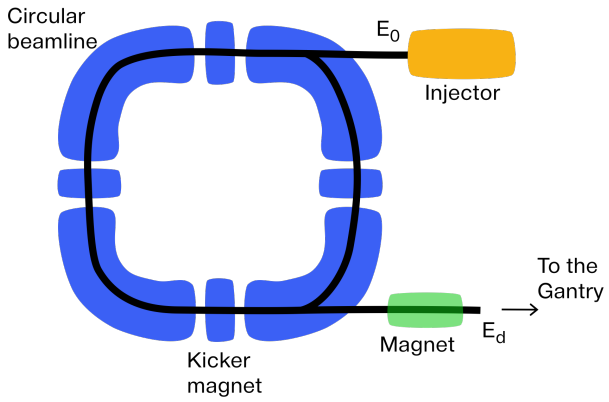

Figure 2.4 – Schematic of a synchrotron. E_0: energy of protons injected in the cyclotron, E_d: energy used for the delivery.

Cyclotrons and synchrotrons in medical facilities

As mentioned in Section 2.1.2, cyclotrons and synchrotrons require some space and are located outside the treatment room. This is advantageous in that particle beams can be provided to several treatment rooms. Illustration of a medical facility and a treatment room are respectively given in Figures 2.5 and 2.6.

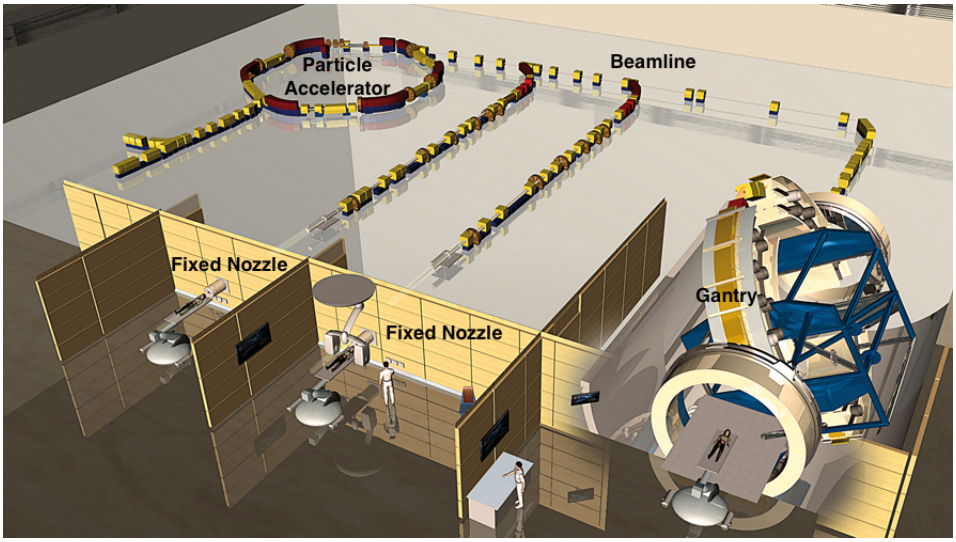

Figure 2.5 – Schematic of a proton therapy center. [2]

b. Source: Berkeley Lab - http://newscenter.lbl.gov/2010/10/18/ion-beam-therapy/.

Figure 2.6 – Gantry in a proton therapy treatment room. The nozzle is able to rotate 360 degrees around the movable patient couch. [Paganetti and Bortfeld, 2005]

Cyclotrons and synchrotrons are both an effective way to accelerate protons. However, only synchrotons can currently be used to accelerate heavy particles [Paganetti et al., 2012]. Another difference between these particle accelerators is the time needed to provide beams of different energies to the gantry as a result of the methods used to change the energy - around 2-3s for synchrotrons [Smith et al., 2009] and around 50-150ms for cyclotrons [Pedroni et al., 2004; Schippers et al., 2007].

2.2 Internal beam radiation therapy

The internal beam radiation therapy (also called brachytherapy) consists of inserting radioactive seeds (such as Caesium-137, Iridium-192) in specific locations in a patient in order to irradiate the target volume. A schematic of such treatment is presented in Figure 2.7.

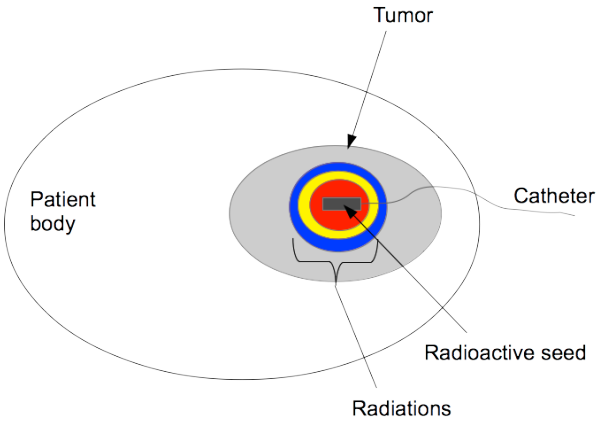

Figure 2.7 – Schematic of the brachytherapy principle.

Internal beam radiation therapy, even though mentioned for general knowledge, will not be studied in the scope of this work.

2.3 Protons and photons in radiation therapy

The rest of this dissertation will focus on radiation therapies performed by proton and photon beams.

2.3.1 Establishment and cost comparison

As of August 2013, there were 43 proton therapy centers with a total of 122 treatment rooms worldwide. This corresponds to 0.9% of conventional photon therapy centers. However, proton therapy is a growing field and it has been estimated that there will be 1000 treatment rooms by 2030 [Goethals and Zimmermann, 2013]. Cost is the limiting factor in establishing more proton therapy facilities - €95 millions (≈ $130 millions) for a proton only facility and €23 millions (≈ $30 millions) for a conventional photon therapy center. Regarding the cost per fraction, it is estimated respectively to be €740 (≈ $1000) and €230 (≈ $300) [Peeters et al., 2010].

2.3.2 Radiation comparison

Photon and proton based radiation interact differently with materials. Photon radiation deposits a large amount of energy when entering the material and decreases with the depth. Proton radiation deposits a relatively small amount of energy when entering the material and increases to a depth known as the Bragg Peak, at which point no energy is left and the radiation stops. Figure 2.8 presents the dose profiles, *i.e.*, the energy deposited along the depth, for a photon beam, a *mono-energetic proton beam*, and a beam composed of protons of different energies (referred to as *poly-energetic proton beam*). The target region corresponds to the area that should ideally receive the highest dose. We can notice that the photons deposit a high amount of energy when entering a medium and continues to irradiate after the target region, whereas the mono-energetic proton beam deposits more energy inside the target and nothing after. Figure 2.9 presents the deposited dose for treatments performed with photons and protons. It clearly shows that tissues behind the target region can be spared using proton radiation.

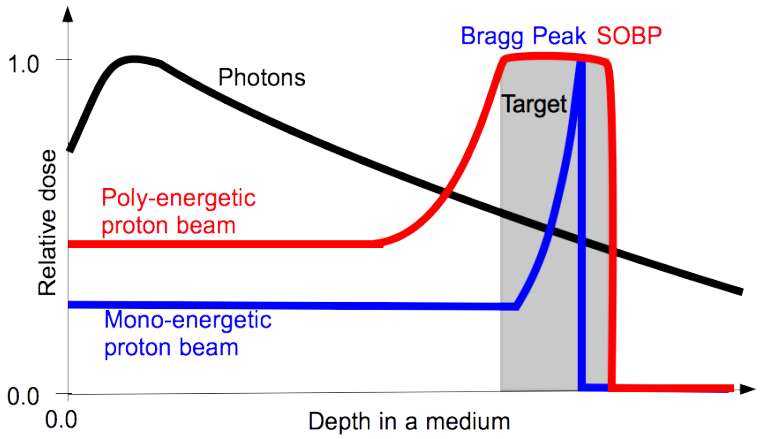

Figure 2.8 – Dose profiles for photons and protons.

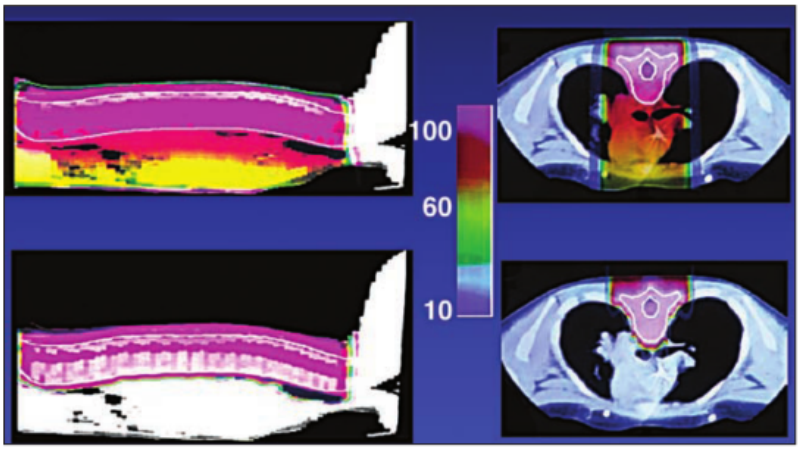

Figure 2.9 – Comparison of deposited dose for a treatment: photons (upper panels) versus protons (lower panels). [Kirsch and Tarbell, 2004]

2.4 Process of a radiation therapy treatment

2.4.1 General treatment planning

Once a tumor has been found and the medical team (*e.g.*, physician, oncologist, physicist, dosimetrist) decides to treat the cancer with radiation, images are taken to locate the tumor and assess its biological activity. The imaging modalities depend on the decisions made by the medical team but can include anatomical imaging techniques such as Magnetic Resonance Imaging (MRI), CT or ultrasounds and functional imaging techniques such as Single Photon Emission Computed Tomography (SPECT) or Positron Emission Tomography (PET).

Using information collected from the images and medical examinations, the clinicians delineate different volumes that will be used for the planning process [International Commission on Radiation Units and Measurements, 2008]:

- The *Gross Tumor Volume (GTV)* corresponds to the tumor location visible in the images.
- The *Clinical Target Volume (CTV)* corresponds to the GTV and the suspected microscopic spread of the tumor.
- The *Planning Target Volume (PTV)* corresponds to a geometrical concept that includes the CTV and the surroundings of the tumor to take into account geometric uncertainties such as internal motions of the CTV during the therapy, set-up uncertainties such as positioning and alignment of the beam and the patient, mechanical uncertainties, and human factors.
- The *organs at risk (OARs)* correspond to healthy tissues sensitive to radiation that should receive the smallest possible dose and ideally no dose.
- The *Planning organ at Risk Volume (PRV)* corresponds to the OARs and the surroundings similarly to the PTV with a goal of ensuring with a high probability that the OARs are spared.

Based on the dose prescribed by a physician and the volumes previously defined, a physicist or a dosimetrist will produce a treatment plan defining the gantry angles and the control files of the delivery system, such as MLC configurations in photon therapy. The planning must ensure that the PRV does not receive more than a maximum threshold and that the PTV receives no less than a minimum threshold. The amount of radiation is measured in Gray (Gy). A example of minimum dose for a tumor ranges from 60 to 80 Gy and for healthy tissues the maximum dose will vary with the tissue's sensitivity to irradiation and are in the order of: 20 Gy for lungs, 50 Gy for bones or 12 Gy for the eyes. The treatment plan will also define the treatment fractions which correspond to the administration of portions of the overall treatment. For example, for an adult, one can plan to deliver 1.8 to 2 Gy per day [Paganetti et al., 2012], five days a week for three to five weeks. The fractionation of treatment helps protect the patient, since delivering a high dose to a patient in a single fraction can be lethal. Moreover, healthy cells tend to recover more easily than cancerous cells from radiation. Therefore, fractionation allows the former cells to regenerate before being irradiated again. Once the treatment plan has been approved by the physician, the patient can be treated.

2.4.2 Photon therapy planning and delivery

Several methods exist to deliver a photon therapy treatment. Either the beam can rotate around the patient and stop at specific angle to deliver the irradiation, such as in the IMRT technique commonly referred to as the "step and shoot technique", or it can rotate continuously and irradiate continuously such as in the Volumetric Arc Therapy (VMAT). Another technique, not relying on MLCs but on a thin photon beam (order of millimeter) to accurately deliver the treatment is called stereotactic radiotherapy (*e.g.*, $CyberKnife$® from Accuray). Among these techniques, we focused on the IMRT, which offers interesting algorithmic problems.

The IMRT technique uses a nozzle that generates a cone beam that rotates around the patient and converges on the tumor site. In the planning process, for each of these angles a 2D dose distribution (also called intensity map or fluence map) across the radiation beam is computed based on optimization techniques [Hamacher and Küfer, 2002] in order to plan the desired overall dose. Figure 2.10 presents intensity maps for various gantry angles. At each gantry angle the beam is shaped using a MLC which consists of a set of parallel pairs of facing strips referred to as leaves. These strips are composed of high atomic number material, such as Tungsten, in order to stop radiation. The strips of a given pair can move toward or away from each other. In the former case, the pair will form an open gap and in the latter it will block the radiation. A specific positioning of all the pairs of leaves is called a MLC configuration. Figure 2.11 shows an example of MLC configuration.

The planning phase consists of finding a fluence map, corresponding to a 2D grid of the dose that must be delivered locally in the patient for each gantry angle. In order to achieve these fluence maps, a Treatment Planning System (TPS), using optimization techniques, computes and finds a set of MLC configurations per gantry angle to be used during the treatment along with the time each configuration must be maintained. While the quality

of a plan is judged for dosimetric properties, two criteria are considered to evaluate the efficiency of the MLC configurations. The first one, the beam on time, corresponds to the total patient irradiation time and is the sum of the duration of each configuration. The other criteria is the total setup time, which corresponds to the time needed to shape all the configurations. This time is approximately proportional to the number of configurations. These two criteria needs to be minimized to have an efficient plan and ensure that the patient doesn't receive an unnecessary dose or prolonged treatment.

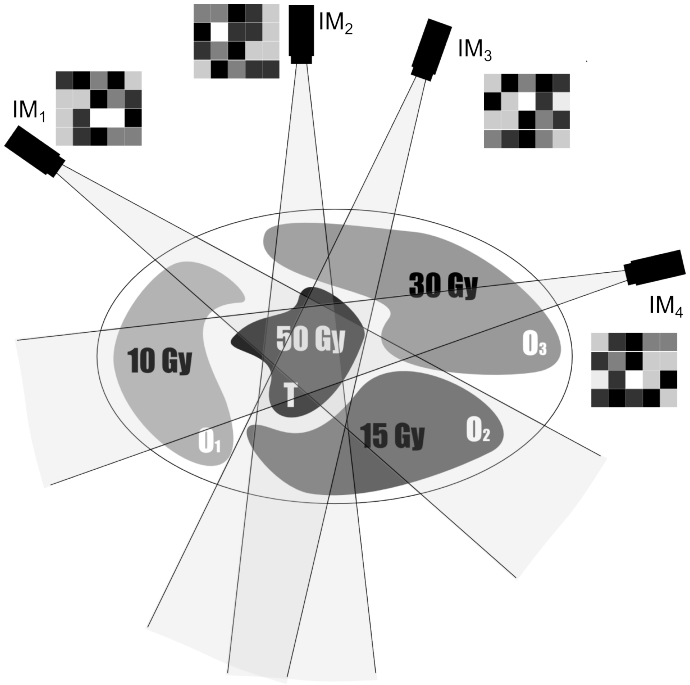

Figure 2.10 – IMRT grantry angles and intensity maps: IM_1, IM_2, IM_3, IM_4.

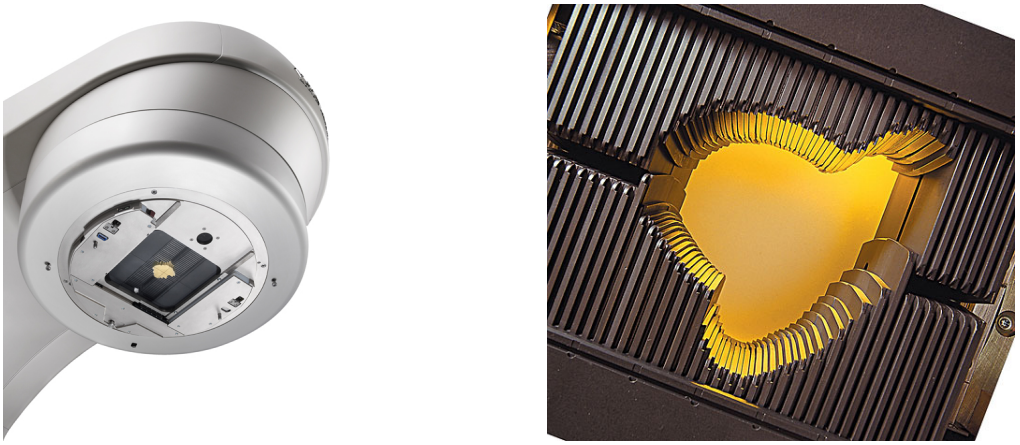

(a) View of an MLC in a nozzle

(b) An MLC configuration

Figure 2.11 – Examples of MLCs

The MLC described above is the conventional MLC and the most widely used. However, in the last decade new technologies allowed for the development of new types of MLCs. Among them the Dual Layer MLC and the Rotating MLC will be presented in Part III Section 2.2. In the scope of this thesis, we studied, in Part III, the minimization of the beam on time and the total setup time for these new types of MLCs.

2.4.3 Proton therapy planning and delivery

In proton therapy, protons are accelerated in a particle accelerator and conducted to the nozzle through an electro-magnetic beamline. The gantry allows the nozzle to rotate around the patient. In the planning phase, one defines the angles where the gantry stops. Based on these angles, the prescribed dose and the fractions of a treatment plan are computed and optimized in a TPS. The treatment plan provides energies to be used to irradiate the 3D volume of the tumor.

There is a Bragg Peak associated with each proton energy (see Section 2.3.2) as well as a so-called *energy layer* which corresponds to the set of positions in the patient's body where the Bragg Peak will occur. Note that, due to the heterogeneity of tissue mass densities, an energy layer may not correspond to a plane layer. In order to cover a wider region than the width of the Bragg Peak, one can combine proton beams of several energies which will generate a so-called Spread-Out Bragg Peak (SOBP) (see Figure 2.8). This SOBP is used to cover the entire depth of the tumor. On the way to the tumor, the amount of dose deposited by the beams will accumulate while staying in a moderate scale compared to the dose applied to the tumor. This technique leads to better coverage of the tumor and minimizes the impact to healthy tissues, especially behind the tumor. These energy layers are defined during the planning to control the depth of the tumor (see Figure 2.12). The irradiation of an energy layer is controlled by the delivery technique used. There exists two main methods described below.

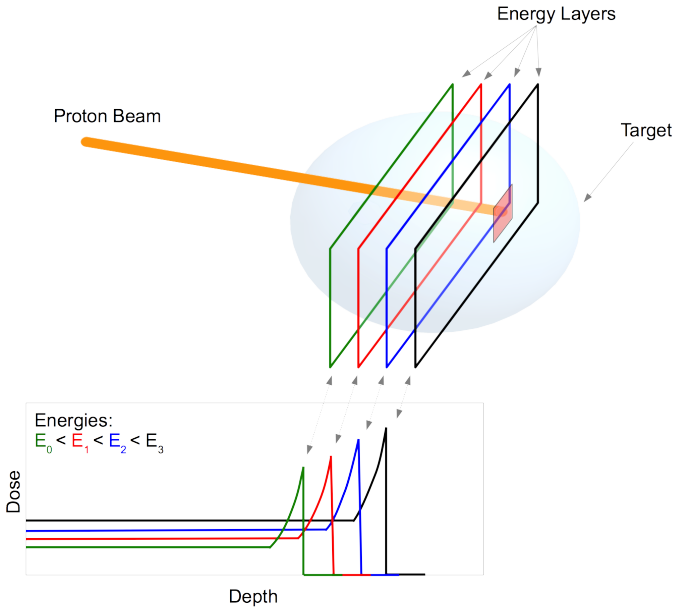

Figure 2.12 – Principle of energy layers

The first method (see Figure 2.13), called *scattering*, uses a beam that is broaden through two scatterers in order to cover the entire tumor or a large portion of it. This broaden beam width can be in the order of several centimeters. The beam is then shaped laterally and vertically by the use of a collimator (also called aperture). A range compensator adjoining the aperture allows for fine and local tuning of the Bragg Peak positions over the beam's surface (see Figure 2.14), especially for the distal energy layer. The aperture and range compensator are machined specifically for each patient.

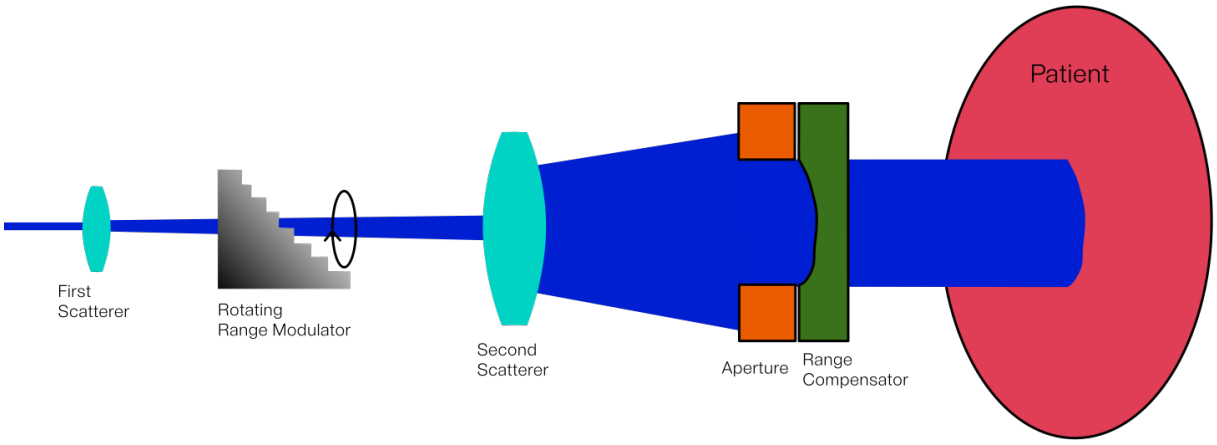

Figure 2.13 – Scheme of beam scattering delivery

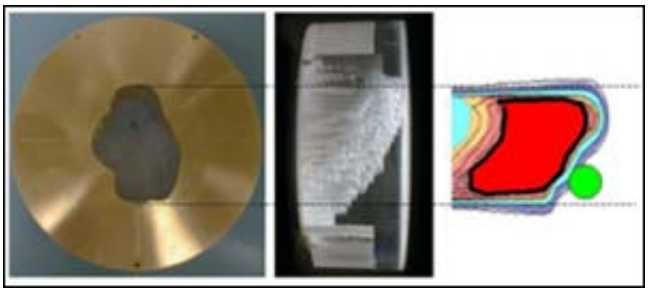

Figure 2.14 – Example of brass aperture and range compensator.[3]

c. Picture from http://www.massgeneral.org/radiationoncology/AboutProtonTherapy.aspx

The second method, called *spot scanning*, uses a narrow pencil beam to deliver dose to the target in a spot by spot fashion. The principle of this technique is to laterally and vertically deviate a thin proton beam (a so called "beamlet" in the order of millimeters) using a set of steering magnets and to sequentially change the energy of the beam in order to create a SOBP (see Figure 2.8). By controlling the beam deviation one can scan an entire energy layer using a mono-energetic beam. The beam stays at a given position for a certain amount of time, called weight, to deliver a certain amount of protons. This weight is measured in Monitor Units (MU). In the case of discrete spot scanning delivery, the beam can be turned off between two spots. It can also be kept on in the so-called raster scanning. As mentioned earlier, the principle of multiple energy layers is used to allow a 3D scanning of the tumor site (see Figure 2.15).

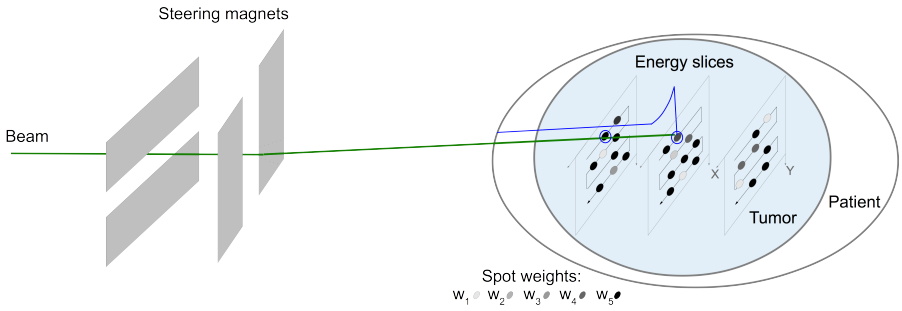

Figure 2.15 – Scheme of the spot scanning technique.

One difference between the scattering and the spot scanning techniques is the sensitivity to motion. Scattering is less sensitive to motions and range uncertainties since the beam covers a wide area. However, spot scanning allows a better conformity to complex shapes especially if there are concavities in the tumor. Moreover, it provides a better conformity to the proximal part of the target and does not require patient specific aperture and compensator.

The planning phase, performed through a TPS, consists of determining the set of energies to use in order to form a SOBP. Moreover, for the scattering method, the aperture and the range compensator must be machined. In the scanning technique, a set of beam positions associated with a weight is defined and optimized for each energy layer. The

result is a *treatment plan* consisting of a set of beam parameters (E, X, Y, W) where E is the beam energy (also defining the target energy layer), X and Y control the deviation of the beam in the energy layer and W is the duration of the irradiation of this given spot. Finally, the TPS can also synthesize the treatment plan as an expected dose distribution in the patient volume.

2.5 Radiation therapy challenges

2.5.1 Uncertainties in radiation therapy

The quality of radiation therapy treatments is influenced by random and systemic uncertainties due to the equipment as well as patient motions.

Uncertainties are mainly composed of setup uncertainties and range uncertainties. Setup uncertainties refer to the patient-device positioning. This type of uncertainty is in the order of $\pm 1.5mm$ [Paganetti et al., 2012]. Range uncertainties are due, among other things, to uncertainties in the CT Number ($\pm 3.5\%$ of range), in the Bragg Peak position ($\pm 1.3mm$), in the SOBP position ($\pm 0.6 - 1.0mm$) and the range computation in tissues with complex heterogeneities ($\pm 1mm$).

Motions can be either inter-fraction or intra-fraction. Inter-fraction motions consist in all the varying shapes in the patient body between one fraction to another. For instance, weight variations, tumor swelling or shrinkage, full or empty bladder or intestinal gas can generate motions of the tumor or of the OARs which can result in their underdosage or overdosage, respectively. Intra-fraction motions are all the motion occurring during the delivery: *e.g.*, breathing, heart beats, hiccup, cough. The spot scanning in proton therapy is particularly sensitive to intra-fraction motions since it relies on a thin proton beam.

2.5.2 Mitigation techniques in radiation therapy

Different techniques are used to cope with the uncertainties and the motions during a treatment. In general, in facilities, periodical commissioning of the treatment devices, the TPS, or the imaging machines helps reduce uncertainties. During the planning phase, designing margins around the tumor and the OARs, as described in Section 2.4.1, allows one to take into account uncertainties and encompass different tumor positions that could occur during the treatment. Moreover, the choice of the number of beams or the beam angles has an impact on the effect of uncertainties and motions during treatments. For example, if the amplitude of a motion along a given direction is smaller than in the other directions, one could place the beam along this direction. Moreover, increasing the number of beam angles allows one to lower the error between the planned dose and the actual delivered dose for each beam angle, thereby increasing the likelihood of properly irradiating the tumor.

To deal with inter-fraction motion, some strategies of re-planning between fractions have been shown to be effective [Hansen et al., 2006].

During the delivery, internal or external markers can be used to properly align the patient and the treatment device. They can also be used to infer the tumor position such as in fluoroscopy using radioactive internal markers, the *Calypso*® system (Varian) using electro-magnetic internal markers, or simply by using external visual markers. With these inferences, the delivery machine can be adapted in real time such as in the beam tracking method [Bert et al., 2010] based on the adaptation of the beam position and energy, or in the dynamic MLC technique [Sawant et al., 2009] based on the adaptation of the MLC configuration. These markers can also be used to deliver the treatment using the beam-gating [Keall et al., 2006], which consists of irradiating the patient only when the markers reach a specific position. Another strategy used during the treatment to reduce the impact of motion is to control the patient breathing cycle either by asking the patient to hold his/her breath while being irradiated, coaching the patient to breathe with audio and/or visual cues, or by administering anesthesia [Bert and Durante, 2011]. Other strategies, such as abdominal compression [Keall et al., 2006], tend to limit the motion amplitude.

2.5.3 Intra-fraction motion in proton therapy

The effect of motion on radiation dose delivery is especially large in proton therapy, particularly when spot scanning is used as the delivery technique. Since spot scanning uses a narrow pencil beam to deliver dose to the target in a spot by spot fashion, any motion during the delivery can result in undesirable hot spots in healthy tissue or cold spots in target. The resulting dose distribution in the patient may substantially differ from the expected one. Figure 2.16 shows the difference between the irradiation received by a static and a moving radiographic film.

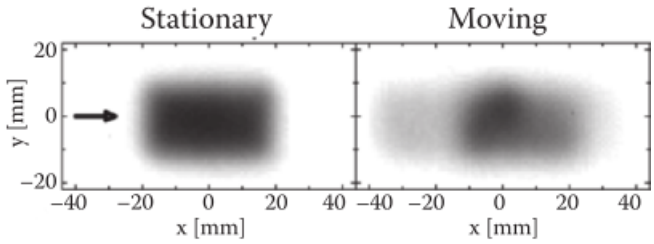

Figure 2.16 – Results of irradiation without (left) and with (right) motion on a radiographic film. [Paganetti et al., 2012]

The problem of intra-fraction motion in spot scanning proton therapy has been widely studied with a number of promising solutions [Zenklusen et al., 2010; Bert et al., 2012; Eley et al., 2014]. These solutions require the capacity of dose computation on a dynamic patient dataset, *i.e.*, 4-dimensional treatment planning, and are often conducted with the researcher's in-house treatment planning system or an expensive clinical treatment

planning system. The limited availability of such 4D treatment planning systems makes it difficult to study this subject by a broader category of researchers. Based on these assumptions, in the scope of this thesis, we decided to make a contribution by developing a tool, named `MSPT` (Motion Simulator for Proton Therapy), aiming at computing and rendering the evolution of the dose distribution during the treatment delivery. In addition, we developed a motion compensation technique in `MSPT` to provide a new approach for a motion mitigation method based on the adaptation of the beam's weight. These developments will be addressed in Part II.

Part II

MSPT: Motion Simulator for Proton Therapy

Chapter 1

MSPT a new tool to study intra-fraction motions

1.1 Development of a proton therapy motion simulator

As introduced in Part I Section 2.5, intra-fraction motions, especially breathing motions, can substantially degrade the quality of a proton therapy treatment using the spot scanning technique. In order to highlight the impact of these motions on the resulting dose distribution and provide a research tool to evaluate and compare different methods of motion management or mitigation, we decided to develop `MSPT`. It is a 4D dose computation and evaluation software.

Before developing `MSPT`, different strategies were considered to perform simulations. Using a commercial treatment planning system (TPS), such as RayStation (RaySearch Laboratories) or Eclipse (Varian), appeared to be not flexible enough regarding the control of motion and often not available to researchers outside a proton therapy center. Such software are especially expensive: around €500 000 (≈ $650 000) for a license and the proton therapy treatment planning functionalities outside a proton therapy facility. Moreover, since these software are dedicated to medical use they can be viewed as black boxes and modifying them or adding third-party plugins is not possible. This limits greatly their use as part of our research. We also considered using a Monte-Carlo engine such as the well-known Geant4 [Agostinelli et al., 2003; Allison et al., 2006; Archambault and Beaulieu, 2003], and TOPAS [Perl et al., 2012](a simulation toolkit built on top of Geant4), which are both freely available and provide accurate dose calculation. However, despite of the dosimetric accuracy, it requires a significant amount of computer time to perform dose computation (*e.g.*, in the order of a couple of hours for a single pencil beam using Geant4, and less than a minute in `MSPT` on a laptop). Moreover, Geant4 or TOPAS require a deep expertise in Monte-Carlo dose calculations and some experience to setup properly proton-therapy simulations. To keep our work with the focus of applied research, we wanted to be able to compute dose distribution in a relatively short time frame and obtain a result close to the dose distribution provided by a commercial TPS. We also wanted this software easily adaptable and accessible such that any user could match it

to their TPS. To our knowledge, no openly distributed dose computation software has become available to meet these requirements. That is why we created the proton therapy simulator, MSPT, based on an analytical dose calculation model specific for spot scanning deliveries.

MSPT source code, user guide and documentation are available at:
http://code.google.com/p/mspt/. It is distributed under the GNU GPL (v3) license.

1.2 MSPT objectives

While MSPT has been developed with the will of providing an open-source and flexible software to make it broadly applicable, two main objectives were important: render the impact of intra-fraction motion and provide a tool to compare treatment plan or mitigation techniques to improve the treatment robustness to motion.

1.2.1 Render the impact on the dose distribution

The first ability of MSPT is to render the final dose distribution resulting from the delivery of a treatment plan to a dynamic patient. This is made possible by the implementation of physical models used to reproduce the interaction between proton beams and matter and described in Section 3.3. However, to be able to render the evolution and the final dose distribution, in the entire patient volume, for a treatment delivered to a moving patient, we also had to introduce motion models and allow these motions during the delivery of a single pencil beam. The patient and motions representations will be addressed in Section 3.2.

1.2.2 Improve the treatment robustness

The second interest of MSPT is to provide information to the user to be able to compare dose distributions such as dose-volume histograms, hot and cold spots and statistical comparisons of the dose distributions. It also provides the 3D resulting dose distributions to let the user perform more specific comparisons outside MSPT. The outputs are described in Section 2.4. Based on these information, the user could compare different treatment strategies for a same patient and could decide which one is more robust to motion.

In addition, a motion compensation technique has been developed in MSPT, which adapts the weight of each beam position without changing the treatment plan. This results in a treatment equivalent to the initial one but with a different scanning path more adapted to the motion simulated. This scanning path is provided to the user as another output to offer help in the improvement of the initial plan, with the objective of making the plan more robust to motion.

Chapter 2

Simulator implementation

2.1 Simulator implementation

`MSPT` was developed in Python 2.7, for the flexibility of this programming language and using subroutines encoded in C to improve the execution speed of critical parts. Digital Imaging and Communications in Medicine (DICOM) files are read using the library PyDICOM [Mason, 2012]. Matrices manipulations rely on SciPy [Jones et al., 2001] and Numpy [Van Der Walt et al., 2011] packages. 2D graphics are rendered using Matplotlib package [Hunter, 2007].

`MSTP` has the ability to model scanning pencil beam based on measured data or an existing beam model from other treatment planning systems. Currently, a beam was modeled after an existing beam model called *"ProtonMachine"* in RayStation (RaySearch Laboratories), a commercial TPS. This model is later referred to as *ProtonMachine*.

2.2 About `MSTP`'s development

The development of `MSTP` has been a major part of this thesis. It represents almost 3 years of development. During these 3 years we had to become familiar with the proton therapy and have a good understanding of the spot scanning delivery technique (*e.g.*, mechanical and physical aspects of the delivery systems) and the underlying physics. In addition, it was necessary to become familiar with clinical knowledge, such as the data used by TPS or the data used by clinicians to evaluate the quality of a treatment plan. This has been made possible thanks to the collaboration with physicists from the department of radiation oncology at the University of Iowa. They followed the development since the beginning and shared their expertise. Moreover, they helped us by planning and simulating static proton therapy treatments in RayStation. These plans and simulations were used to evaluate `MSTP` (see Chapter 4) and were also used as a basis for our motion and compensation simulations.

In order to develop a tool that could be of interest for future research in the field of proton therapy we wanted to ensure that the dose calculations performed by `MSTP` were

coherent with the dose calculations obtained from *ProtonMachine*. Obtaining close results required a lot of effort and ingenuity as RayStation can be viewed as a tool whose internal details are hidden to the user. For example, data such as the number of protons per monitor units (MU), or the dose profiles (*i.e.*, curves representing the dose as a function of depth) for all the energies used by *ProtonMachine* were not accessible and necessitated reverse engineering or auxiliary studies. The dose and stopping power correction factor functions (see Section 3.3) illustrate some of these auxiliary studies.

To facilitate the use of `MSTP`, we designed it such that it could handle DICOM files dedicated to radiation therapy and DICOM image files (see Section 2.3), which is the typical data used by clinical TPS. More generally, DICOM is a standard used in medical facilities for communication and storage of medical information. Handling these files required a good knowledge of the DICOM standards in order to extract all the data needed to simulate the delivery (*e.g.*, number of fractions, number of beams, beam angles, body structures, pencil beam position relative to the patient). This resulted in the development of the *dicomReader* package (see Section 2.5) that could be used as a standalone package.

Based on the various competencies and data acquired we designed, implemented and evaluated `MSTP`. The documentation has been generated with Sphinx[1] and is available on `MSTP`'s website. The implementation can be described in a few figures: 24 classes, around 400 functions and more than 12500 lines of code.

2.3 The DICOM standard

In this section, we will present briefly the DICOM standard in order to provide sufficient background information to the reader for a better understanding of the following sections.

The DICOM standard is defined by the American College of Radiology (ACR) and the National Electrical Manufacturer's Association (NEMA). It describes transmission and storage protocols for clinical data and images. This standard is used in any medical facility. Its design is object-oriented. The description of the DICOM standard is complex and goes beyond the scope of this thesis. Therefore, we will provide a brief and simplified presentation[2]. The DICOM objects used in `MSTP` contain a set of *Attributes* (associated to a *Tag* corresponding to a unique identification number) corresponding to data elements stored in the object. The data stored can be for example a string, a number, an array or another object. A first object used in `MSTP` is the CT Image object storing the patient images. The patient image being a 3D volume, each slice (or frame) of the volume is stored in a CT Image object. Hence, a CT Image object stores a 2D image. The patient 3D image corresponds to a series of CT Image objects. The extension of the DICOM standard for radiation therapy is the DICOM RT standard and is composed of different objects. Those used in `MSTP` are: RT Dose, RT Structure Set and RT Plan. The RT

1. http://sphinx-doc.org/
2. More details about the DICOM standard can be obtained at http://medical.nema.org/standard.html.

Dose object stores the dose distribution planned in a TPS as a result of the treatment plan defined by the RT Plan. The RT Structure Set object stores the volumes of interest defined in the patient, such as, tumor, heart or lung.

Table 2.1 provides an example of data stored in the slice of a CT Image (*i.e.*, a CT Image object). Some attributes relate to the patient information or the image acquisition. The main attributes used in `MSTP` are *Slice Thickness*, *Image Position (Patient)*, *Image Orientation (Patient)*, *Rows*, *Columns*, *Pixel Spacing*, *Pixel Data*, *Rescale Slope and Intercept*.

Tag	Attribute	Value	Description
(0008, 0016)	SOP Class UID	CT Image Storage	This attribute describes the type of data stored in the object
(0008, 0018)	SOP Instance UID	1.3.12.2.1107.5.99.2.20599.30000011122902110259300016743	Identification number of the instance of the object
(0008, 0022)	Acquisition Date	'20120515'	Date of the image acquisition
(0010, 0010)	Patient's Name	'Anonymous'	Name of the patient
(0018, 0015)	Body Part Examined	'CHEST'	Body part of the patient being examined
(0018, 0050)	Slice Thickness	'3.0'	Thickness of the image slices in mm
(0020, 0032)	Image Position (Patient)	['-249.51171875', '-411.51171875', '197.000000']	Coordinates [x,y,z] of the top left pixel of the current slice in mm (*i.e.*, pixel [0,0] in the slice).
(0020, 0037)	Image Orientation (Patient)	['1', '0', '0', '0', '1', '0']	Coordinates of the orientation vectors of the first row and the first column with respect to the patient.
(0028, 0010)	Rows	167	Number of rows
(0028, 0011)	Columns	167	Number of columns
(0028, 0030)	Pixel Spacing	['3.0', '3.0']	Spacing between rows and columns in mm
(7fe0, 0010)	Pixel Data	Array of 55778 bytes	Array storing the pixel values
(0028, 1053)	Rescale Slope	'1'	The slope and intercept are the parameters of the affine transformation to obtain the true pixel intensity (in HU) from Pixel Data.
(0028, 1052)	Rescale Intercept	'-1024'	
...	...	...	

Table 2.1 – Portion of a CT Image object representing a 2D slice of the patient CT image.

Table 2.2 provides an example of data stored in a RT Structure Set object. An instance of this object stores all the contours defined on all the slices of the CT Image for each region of interest (ROI) in the patient (*i.e.*, each body structure delineated). Each ROI named by *ROI Name*, is stored as a sequence of contours and each contour is defined by a set of points defined by the attribute *Contour Data*. Each Contour Data is related to a specific slice of the CT image. Contour Data corresponds to the delineation of the ROI in this CT slice.

Tag	Attribute	Value	Description
(0008, 0016)	SOP Class UID	RT Structure Set Storage	This attribute describes the type of data stored in the object
(0008, 0018)	SOP Instance UID	1.2.826.0.1.3680043.8.176.2012641625103337.48.4226207444	Identification number of the instance of the object
(3006, 0026)	ROI Name	'Tumor'	Name of the selected ROI
(3006, 0042)	Contour Geometric Type	'CLOSED_PLANAR'	Type of contour ('CLOSED_PLANAR' or 'POINT')
(3006, 0046)	Number of Contour Points	'30'	Number of points in the current contour
(3006, 0050)	Contour Data	['6.4141769237', '-115.4705176', '102', '5.2292955389', '-115.0995526', '102', ... '6.4141769237', '-115.4705176', '102']	Coordinates of the points defining the contour in a slice of the CT Image.
...	...	...	...

Table 2.2 – Portion of a RT Structure Set object storing the contours of the regions of interest in the patient.

Table 2.3 provides an example of data stored in a RT Plan object. An instance of this object stores all the beam directions (*i.e.*, gantry angles). For each beam direction, a sequence of energies is defined. For each energy, a list of positions associated to weights is saved. The number of attributes used in `MSTP` is substantial. However, some of the main attributes used are *Number of Fractions Planned*, *Nominal Beam Energy*, *Gantry Angle*, *Isocenter Position*, *Scan Spot Position Map*, *Scan Spot Meterset Weights*, and *Scanning Spot Size*.

Tag	Attribute	Value	Description
(0008, 0016)	SOP Class UID	RT Ion Plan Storage	This attribute describes the type of data stored in the object
(300a, 0003)	RT Plan Name	'Test Plan'	Name of the treatment plan
(300a, 0009)	Treatment Protocols	'PencilBeamScanning'	Type of treatment used.
(300a, 0078)	Number of Fractions Planned	'3'	Number of fractions.
(300a, 0086)	Beam Meterset	'484.53744762'	Total number of MU delivered.
(300a, 0015)	Nominal Beam Energy Unit	'MEV'	Energy units used in the plan.
(300a, 0114)	Nominal Beam Energy	'118.56781803'	Energy used.
(300a, 011e)	Gantry Angle	'180'	Angle of the gantry rotation in degrees.
(300a, 012c)	Isocenter Position	['-46.75731948', '-117.8241278', '69.994276167']	Coordinates (related to the CT Image) of the origin of the coordinate system used to define the pencil beam position in the treatment plan (IEC fixed coordinate system - see Section 3.1).
(300a, 0394)	Scan Spot Position Map	[-13.5, -11.5, -26.0, -16.5]	(x,y) positions of the pencil beams defined in the IEC gantry coordinate system (see Section 3.1). Two positions are defined in this example.
(300a, 0396)	Scan Spot Meterset Weights	[0.024522660300135612, 0.005508291535079479]	Weight of each pencil beam position in MU.
(300a, 0390)	Scan Spot Tune ID	'5_0_mm'	Information about the pencil beam's width.
(300a, 0398)	Scanning Spot Size	[11.774100303649902, 11.774100303649902]	These values are the horizontal and vertical Full Width Half Maximum (FWHM) in mm and allow the calculation of the pencil beam's widths corresponding to the standard deviation of a Gaussian distribution. In this example, the FWHM of 11.77 results in a sigma value of 5 mm, as expected from Scan Spot Tune ID.
...	...	...	...

Table 2.3 – Portion of a RT Plan object storing the entire treatment plan.

Table 2.4 provides an example of data stored in a RT Dose object. An instance of this object stores a 3D dose distribution. The main attributes used in `MSTP` are *Slice Thickness*, *Image Position (Patient)*, *Image Orientation (Patient)*, *Number of Frames*, *Rows*, *Columns*, *Pixel Spacing*, *Grid Frame Offset Vector*, *Dose Grid Scaling*, and *Pixel Data*.

Tag	Attribute	Value	Description
(0008, 0016)	SOP Class UID	RT Dose Storage	This attribute describes the type of data stored in the object
(0018, 0050)	Slice Thickness	'3'	Thickness of the slices of the 3D dose distribution matrix stored in Pixel Data.
(0020, 0032)	Image Position (Patient)	['-196.3120157', '-299.5664854', '-309']	Coordinates in mm of the voxel [0,0,0] (in the 3D dose distribution matrix) defined in the coordinate system used for the CT image.
(0020, 0037)	Image Orientation (Patient)	['1', '0', '0', '0', '1', '0']	Coordinates of the orientation vectors of the first row and the first column with respect to the patient.
(0028, 0008)	Number of Frames	'183'	Number of frames (slices) in the 3D dose distribution matrix.
(0028, 0010)	Rows	81	Number of rows.
(0028, 0011)	Columns	136	Number of columns.
(0028, 0030)	Pixel Spacing	['3', '3']	Spacing between rows and columns in mm.
(3004, 0002)	Dose Units	'GY'	Dose units.
(3004, 000c)	Grid Frame Offset Vector	['0', '3', ... , '540', '543', '546']	This vector contains the offset from the first frame depth in mm. For example, the second frame has an offset of 3 mm. The first frame depth is -309 mm (Image Position (Patient)), so the depth of the second frame is -306 mm.
(3004, 000e)	Dose Grid Scaling	'0.00078957540579'	Scaling factor for the dose data stored in Pixel Data in order to obtain a 3D matrix in units of Dose Units
(7fe0, 0010)	Pixel Data	Array of 4031856 bytes	Array storing the 3D dose distribution.
...	...	...	...

Table 2.4 – Portion of a RT Dose object storing the 3D dose distribution.

2.4 Simulator inputs and outputs

The simulator receives as inputs the treatment plan (energies, beam positions, weights), the patient CT image, the contour of the structures (*e.g.*, entire patient body, organs, tumor), and optionally, the dose calculated by another TPS. These four inputs are all in the DICOM standard.

In addition to the DICOM files, `MSPT` receives optionally a configuration file which set global variables in `MSPT` controlling the delivery parameters, the a priori motion information which can be either from a 4D CT analysis or any function describing motion trajectories, the compensation strategy and the outputs. The details of the configuration parameters can be found in the following sections and in the user manual on `MSPT` website.

`MSPT` provides different outputs to be able to assess the quality of the delivery both visually and quantitatively. For instance, the 3D matrices representing the patient, including defined structures, can be saved as stacks of 2D images or as 3D matrices. Dose distribution matrices, expected and computed, are stored in DICOM files and as stack of 2D images. Dose Volume Histograms (DVHs) are stored as 2D images and as lists of dose-volume data points. Hot and cold spots are stored as 2D images along with statistics in a text files summarizing the quantity of hot and cold spots per structure.

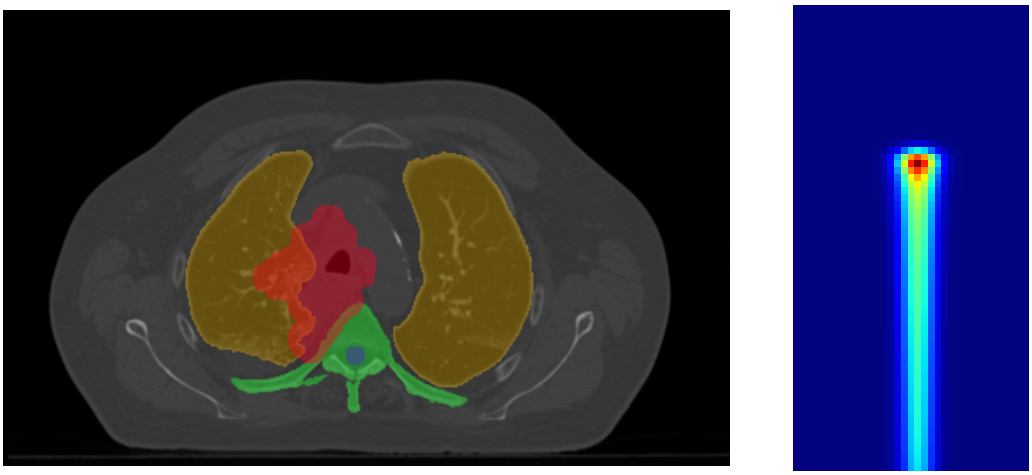

Figure 2.1 – Example of visual outputs: a CT slice with several binary masks of different body structures (left) and the dose distribution of a single proton pencil beam (right).

2.5 Simulator architecture

In this section, we will present an overview of the main python packages we developed to build `MSPT` and the principal relationships between them as well as between them and the main python extensions in C. Figure 2.2 presents the overall organization of MSPT: it shows the 23 classes used for the simulations. Another utility class called *Email* has not been represented in the figure since this class is not mandatory for simulations. However, if the user decides to use this functionality, it is instantiated along with *SimulatorMSPT* in the *main* function.

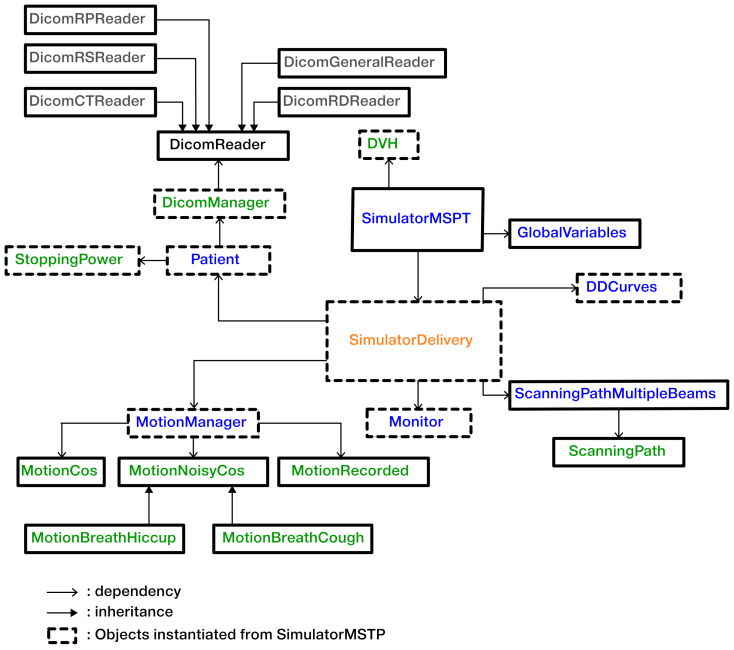

Figure 2.2 – Class diagram of `MSPT`.

Package *simulator*

The package *simulator*, controls at a high level the overall process of the simulation. The two main classes are *GlobalVariables* and *SimulatorMSPT*. The former is derived from a dictionary and used to manage `MSPT` settings defined by the user. The later, instantiated by the *main* function, receives the inputs from the user, instantiates the main objects (patient, motion, motion monitor, depth-dose curves of reference and scanning path) and uses them to instantiate the object of the class *SimulatorDelivery* responsible for the simulation of the delivery. Moreover, at the end of the simulation, *SimulatorMSPT* stores the overall simulation outputs such as the entire final dose distribution or the comparison between the expected dose distribution and the computed one.

Package *dicomReader*

The package *dicomReader* has been developped on top of PyDICOM to be able to load DICOM data and more specifically CT (series of CT Image objects), treatment plan (RT Plan object), body structures (RT Structure Set object) and expected dose distribution (RT Dose object) through the class *DicomManager*. We implemented different types of readers: *dicomCTReader* in charge of the CT image files, *dicomRPReader* in charge of the treatment plan, *dicomRSeader* in charge of the patient body structures, and *dicomRDReader* in charge of the expected dose distribution. The DICOM data is loaded through these readers, which are initialized from the *SimulatorMSPT* object. In addition, we implemented the classes *ScanningPathMultipleBeams* and *ScanningPath*, which aims at storing the treatment plan (gantry angles in *ScanningPathMultipleBeams* and energies, beam positions and beam weights in *ScanningPath*) along with the scanning path parameters (*e.g.*, number of repaintings, type of volumetric repainting) provided in `MSPT` configuration file. These classes are also instantiated from the *SimulatorMSPT* object. Finally, a module *ctToDensityConv* has been created to load and provide a function to obtain the conversion data from CT Number (CT#) to mass density.

Package *patient*

The package *patient* contains the class *Patient* storing all the data of the patient model: 3D arrays of CT#, density, relative stopping power, radiological depth, expected dose distribution and the binary masks of the body structures. The patient is initialized in the *SimulatorMSPT* object.

Package *physics*

The package *physics* manage the depth-dose curves, through the class *DDCurves*, and the stopping-power reference data with the *StoppingPower* class. The depth dose curves and stopping power data of reference are initialized in *SimulatorMSPT* object.

Package *motion*

The package *motion* contains the different types of motions that can be used along with the model of the motion monitoring system. Classes implemented for motions are *Motion-*

Cos (*i.e*, motion simulated as a cosine function), *MotionNoisyCos* (*i.e*, motion based on a cosine function with random amplitude and period variations), *MotionBreathCough* (*i.e.*, motion derived from *MotionNoisyCos* simulating a patient coughing), *MotionBreathHiccup* (*i.e.*, motion derived from *MotionNoisyCos* simulating a patient with a hiccup) and *MotionRecorded* (*i.e.*, a list of motion observations). The class *MotionMonitor* models a motion monitoring system.

Package *scanning*

The package *scanning* contains the class *SimulatorDelivery* that simulates the delivery process for a *Patient* static or moving according to a certain motion and irradiated by given *ScanningPathMultipleBeams* and *ScanningPath*.

Package *extensionC*

The package *extensionC* contains all the python extensions implemented in C: calculation of the dose distribution of a single pencil beam (*beamletSimulation()*), calculation of the radiological depth (*calcRadiolDepth()*) and functions used to build the patient data: CT (*fillCTArray()*), density (*fillDensityArray()*), expected dose (*fillDoseArray()*) and stopping power (*fillStopPwrArray()*) arrays. These extensions are standalone functions called through interface python functions.

Main organization

In this section, we present how are used and organized the different classes, modules and functions previously mentioned. We will present the main tasks of a simulation in `MSPT` (*i.e.*, build the patient model and perform the simulation of the delivery) from a programming point of view. The physics related details of the simulation are presented in the next chapter.

The dependencies and principal functions called from a *Patient* object are summarized in figures 2.3 and 2.4. The initialization of a *Patient* object relies on the information provided by the input DICOM files. It starts with the modeling of the patient body tissues (physics details in Section 3.2.1). It consists of representing the patient as a 3D array where each voxel corresponds to a physical entity (*e.g.*, mass density, stopping power). In a first step, the CT# are obtained from *DicomCTReader* with the function *dataForAttribute()*. In the *Patient* object the 3D array is filled by the function *fillCTArray()*. Then, the conversion from CT# to density is performed with a conversion table accessed by the function *getConversionTableCTToMassDens()* from the module *ctToDensityConv*. The 3D density array is initialized by the function *fillDensityArray()*. The third step generates 3D binary masks of the body structures. The function *getMasksForAssociatedDicomImage()* of the *DicomRSReader* returns them to the *Patient* object. If the user provides the expected dose distribution, the function *dataForAttribute()* of the *dicomRDReader* and the function *fillDoseArray()* initialize the 3D array representing this expected dose distribution. This step finishes the initialization. During the simulation of the delivery the 3D stopping power array is filled based on the 3D density array and the conversion data

obtained from *getConversionTableStpPwrForEnergy()* and filled by the function *fillStopPwrArray()*. Finally, the computation of the dose distribution requires the calculation of the radiological depth in the patient. This is performed by the function *calcRadiolDepth()*.

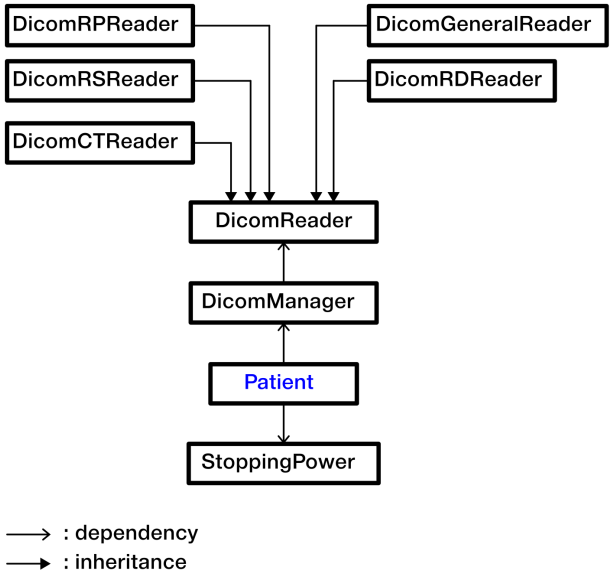

Figure 2.3 – Diagram representing the dependencies used to build a *Patient*.

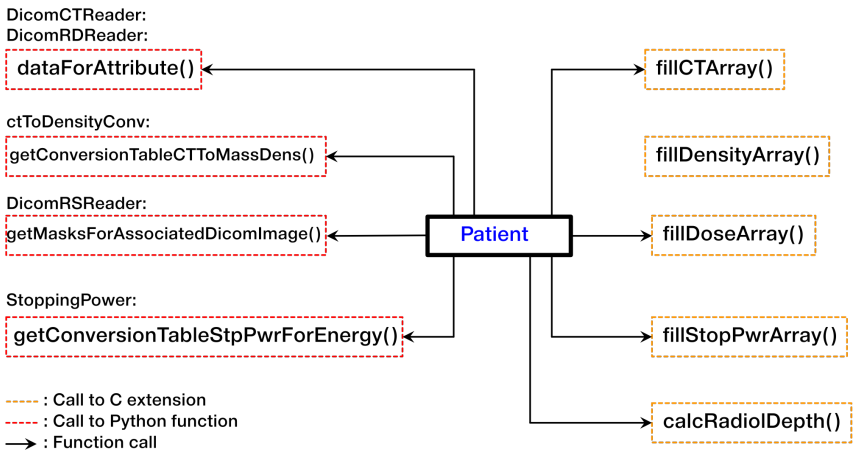

Figure 2.4 – Diagram representing the main function calls from the *Patient* object to initialize and update the patient model.

The dependencies and principal functions called from a *SimulatorDelivery* object are summarized in figures 2.5 and 2.6. During the simulation of the delivery gantry angles are provided through an iterator of *ScanningPathMultipleBeams* and the positions, weights and energies of the pencil beam are provided through an iterator of *ScanningPath*. At every proton energy transition, during the delivery, the corresponding depth dose curve data is obtained through the function *dataForEnergy()*. Before every computation of the dose distribution induced by a pencil beam the true displacement vector of the patient body

is obtained through the function *getDisplacementVectorAtTime()*. In addition, based on this displacement vector, the radiological depth in the patient body re-computed and accessed by *getPatientDataForDisplVector()*. Finally the dose distribution is calculated with the function *beamletSimulation()*.

In the implementation of the mitigation strategy we rely on the model of a motion monitoring system (*i.e.*, *Monitor*). Since its accuracy can vary, depending on `MSPT` settings, we refer to the motion information provided as a *measurement* (*i.e.*, true displacement vector plus or minus some measurement error). To obtain this measurement the delivery simulator invokes the function *getMotionMeasurement()*. This measurement is accessed only when the pencil beam position changes.

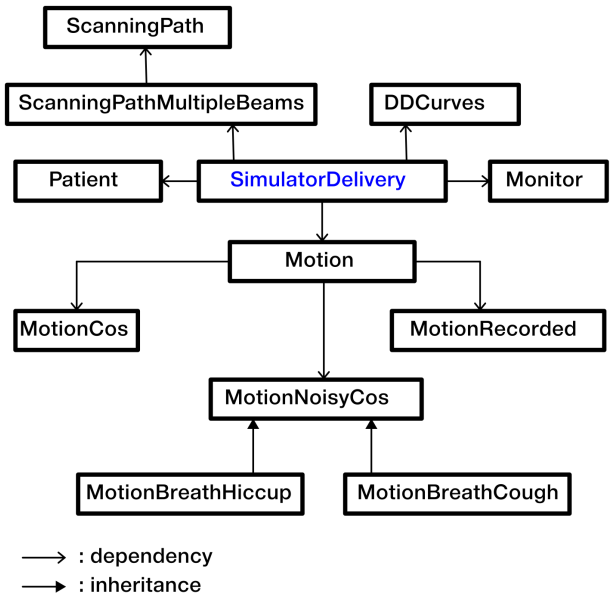

Figure 2.5 – Diagram representing the relationships between the classes used to simulate the delivery of a treatment in *SimulatorDelivery*).

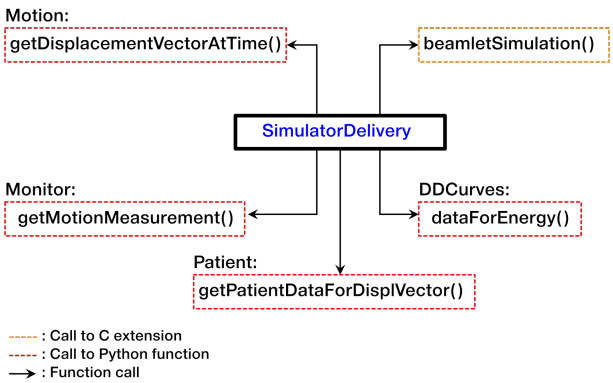

Figure 2.6 – Diagram representing the main function calls from the *SimulatorDelivery* object during the simulation of a delivery.

Chapter 3

Physics models

3.1 Coordinate systems

MSPT relies on three main coordinate systems to represent the patient being treated and to simulate the delivery of a treatment. The first is the DICOM patient coordinate system (see Section 3.1), which corresponds to the coordinate system defined in the patient CT images. The second coordinate system, called the International Electrotechnical Commission (IEC) fixed coordinate system (see Section 3.1), is used to define specific positions to relate position defined for the delivery and the DICOM patient coordinate system. In addition, in MSPT, it is also used to define patient motion parameters. The third coordinate system, namely the IEC gantry coordinate system (see Section 3.1), is used to define the positions for the delivery at a specific gantry angle. We will present these three coordinate systems in details in the next sections.

DICOM patient coordinate system

The patient is represented as volume by a 3D matrix from the CT image. Indices of the volume elements (voxel) start at the top left corner of the first image slice (also referred to as frame). The CT DICOM file specifies the location, in the DICOM patient coordinate system, of this first voxel.

The DICOM patient coordinate system is defined by the X_{dicom}, Y_{dicom} and Z_{dicom} axis. It is defined in the DICOM images by the abscissa (X_{dicom}) and ordinate (Y_{dicom}) orientation vectors are stored in the attribute *Image Orientation Patient*, expressing the direction cosine of the first row of voxels and the first column with respect to the patient. Z_{dicom} corresponds to the cross product of X_{dicom} and Y_{dicom}. For example, if *Image Orientation Patient* $= [0, 0, 1, 0, 1, 0]$, the X_{dicom} axis is along the first row of voxels, Y_{dicom} axis is along the first column of voxels and Z_{dicom} is along the image frames' direction.

Figure 3.1 shows the coordinate system and the voxel indexing system.

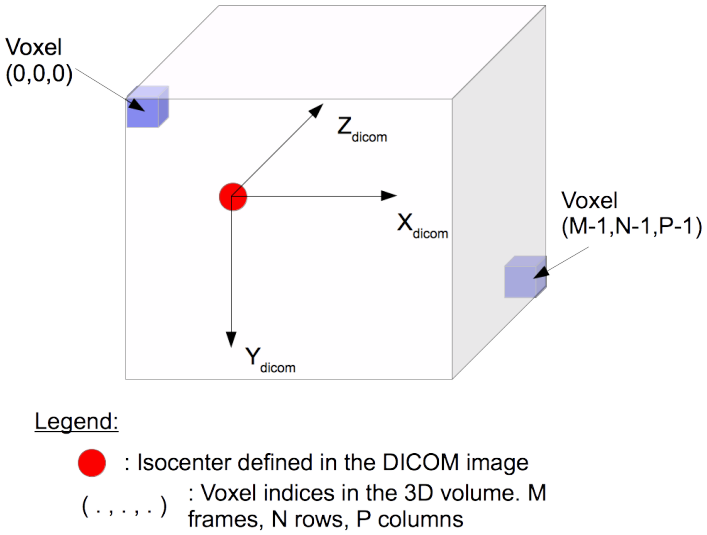

Figure 3.1 – DICOM patient coordinate system and voxel indexing system.

The transformation matrix from voxel indices to the coordinate system is defined as follows [Medical Imaging and Technology Alliance, 2011] :

$$\begin{pmatrix} P_x \\ P_y \\ P_z \\ 1 \end{pmatrix} = \begin{pmatrix} X_x\Delta_i & Y_x\Delta_j & Z_x\Delta_k & S_x \\ X_y\Delta_i & Y_y\Delta_j & Z_y\Delta_k & S_y \\ X_z\Delta_i & Y_z\Delta_j & Z_z\Delta_k & S_z \\ 0 & 0 & 0 & 1 \end{pmatrix} \begin{pmatrix} i \\ j \\ k \\ 1 \end{pmatrix} \tag{3.1}$$

Where:

- P_x, P_y, P_z are respectively the x, y, z coordinates of the voxel (k, j, i) in the volume in units of mm.
- S_x, S_y, S_z are the coordinates of the Image Position Patient attribute in the CT DICOM file. It corresponds to the coordinates, in mm, of the voxel $(0, 0, 0)$.
- X_x, X_y, X_z are the components of direction cosine of the first row of voxels (from the *Image Orientation Patient* attribute in the CT DICOM file).
- Y_x, Y_y, Y_z are the components of direction cosine of the first column of voxels (from the *Image Orientation Patient* attribute in the CT DICOM file).
- Z_x, Z_y, Z_z are the components of direction cosine of the frames' direction with respect to the cross product between X_{dicom} and Y_{dicom}.
- k, j, i are respectively the frame, row and column indices. They start at 0.
- Δ_k, Δ_j, Δ_i are respectively the frame, row and column spacings of the voxels in units of mm.

IEC coordinate systems

The IEC [International Electrotechnical Commission, 2011] defines standard coordinate systems for equipment and data related to the process of radiation therapy. In our

simulator, we used the IEC Fixed and Gantry coordinate system. These coordinate systems are Cartesian right-handed and are represented in Figure 3.2.

The IEC fixed (with respect to the patient/table) coordinated system has its origin at the isocenter defined in the treatment plan. Its $Z_{\text{IEC Fixed}}$ axis points upward (*i.e*, toward the nozzle when the gantry angle is 0° and the $Y_{\text{IEC Fixed}}$ axis points along the gantry rotation axis.

The IEC gantry coordinate system is the IEC fixed coordinate system rotated clockwise around the $Y_{\text{IEC Fixed}}$ axis (*i.e.*, the $Y_{\text{IEC Gantry}}$ axis). Its $Z_{\text{IEC Gantry}}$ axis points toward the nozzle.

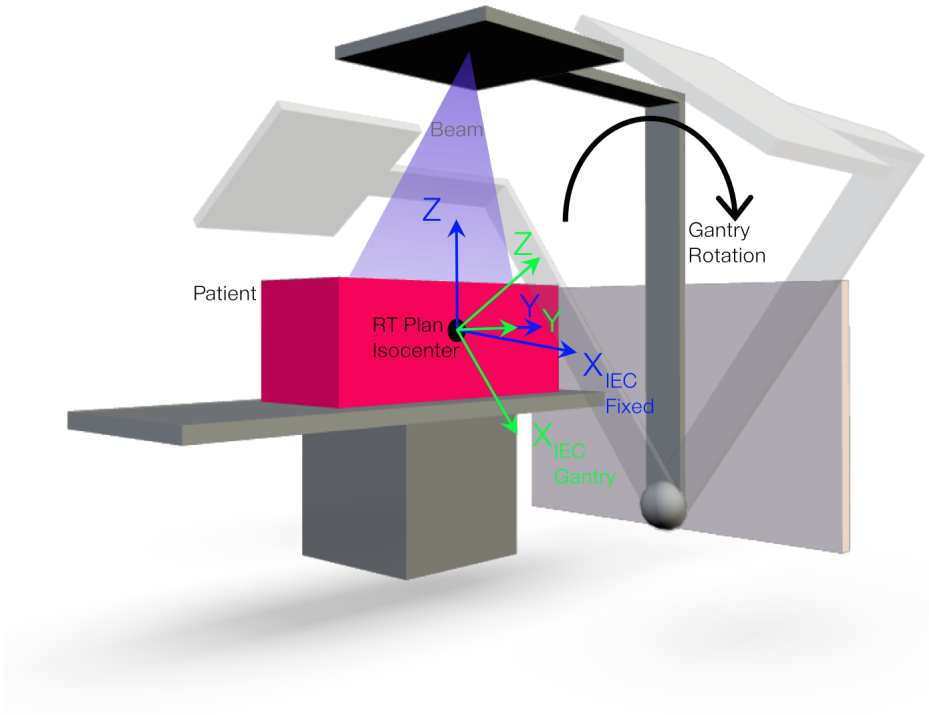

Figure 3.2 – IEC Coordinate systems

For a clock-wise gantry rotation θ, a rotation matrix calculates the mapping of points defined in the IEC fixed to the IEC gantry coordinate system:

$$\begin{pmatrix} X_{\text{IEC Gantry}} \\ Y_{\text{IEC Gantry}} \\ Z_{\text{IEC Gantry}} \\ 1 \end{pmatrix} = \begin{pmatrix} \cos(\theta) & 0 & \sin(\theta) & 0 \\ 0 & 1 & 0 & 0 \\ -\sin(\theta) & 0 & \cos(\theta) & 0 \\ 0 & 0 & 0 & 1 \end{pmatrix} \begin{pmatrix} X_{\text{IEC Fixed}} \\ Y_{\text{IEC Fixed}} \\ Z_{\text{IEC Fixed}} \\ 1 \end{pmatrix} \tag{3.2}$$

The transformation matrix to convert the coordinates of the DICOM coordinate sys-

tem to the IEC fixed coordinate system:

$$\begin{pmatrix} x_{IECfixed} \\ y_{IECfixed} \\ z_{IECfixed} \\ 1 \end{pmatrix} = \begin{pmatrix} 1 & 0 & 0 & -I_x \\ 0 & 0 & 1 & -I_y \\ 0 & -1 & 0 & I_z \\ 0 & 0 & 0 & 1 \end{pmatrix} \begin{pmatrix} x_{dicom} \\ y_{dicom} \\ z_{dicom} \\ 1 \end{pmatrix} \tag{3.3}$$

where I : (I_x, I_y, I_z) is the position of the treatment plan isocenter in the DICOM coordinate system.

3.2 Patient and motion models

3.2.1 Patient representation

To model the patient, we first convert the CT# of each voxel into mass densities using a default or user-defined conversion table and, then, into relative proton stopping powers, which quantifies the proton energy loss induced by each voxel. Figure 3.3, represents the default conversion table from CT# to mass density. It was obtained from RayStation data.

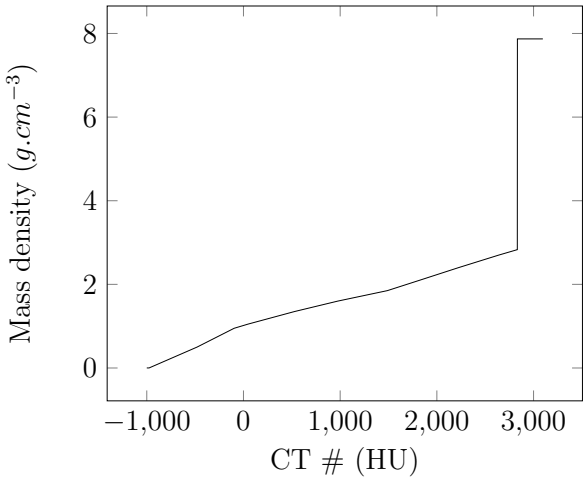

Figure 3.3 – Conversion from CT# to mass density

The conversion from mass densities into relative proton stopping power (*i.e.*, relative to water proton stopping power) is based on a linear interpolation of mass stopping power values. This interpolation uses tables storing the mass stopping power for proton energies ranging from 30 MeV to 230MeV with a step of 5 MeV, later referred to as *"energies of reference"*, for each of the following media: air (1.205×10^{-3} $g.cm^{-3}$), adipose (0.920 $g.cm^{-3}$), water (1.0 $g.cm^{-3}$), skeletal muscle (1.04 $g.cm^{-3}$) and cortical bone (1.85 $g.cm^{-3}$). Hence, for a given proton energy and density one can easily compute the mass stopping power using a linear interpolation between the energies and between the densities. The mass stopping power table were obtained from the database PSTAR (Physical Measurement Laboratory) [Berger et al., 2005]. These tables provide for the mass stopping power values, which are multiplied by the density to obtain the stopping power

and divided by the stopping power of water in order to obtain the relative stopping power.

3.2.2 Motion management

The motion information, provided as an input, controls the motion simulation. The motion consists of a function $f : (x, y, z, t) \mapsto (x', y', z')$, time dependent providing the new position of each voxel or intended delivery spot in the patient.

For the purpose of testing `MSPT`, the motion is currently simulated using a rigid body transformation based on a breathing model, later referred to as "*ideal breathing model*", defined by Lujan et al. [1999] and slightly modified by George et al. [2005] and Seco et al. [2009], relying on a cosine function as follows:

$$\begin{pmatrix} x(t) \\ y(t) \\ z(t) \end{pmatrix} = \begin{pmatrix} x_0 \\ y_0 \\ z_0 \end{pmatrix} + \begin{pmatrix} b_x \cos(\frac{2\pi t}{\tau_x} + \phi_x) \\ b_y \cos(\frac{2\pi t}{\tau_y} + \phi_y) \\ b_z \cos(\frac{2\pi t}{\tau_z} + \phi_z) \end{pmatrix} \tag{3.4}$$

where (x_0, y_0, z_0) is the initial position in the IEC fixed coordinate system, b_x, b_y, b_z are respectively the motion amplitudes along the $X_{\text{IEC Fixed}}$, $Y_{\text{IEC Fixed}}$ and $Z_{\text{IEC Fixed}}$ axis, τ_x, τ_y, τ_z the respective motion periods and ϕ_x, ϕ_y, ϕ_z the respective starting phase. Figure 3.4 shows an illustration of the breathing model along one axis.

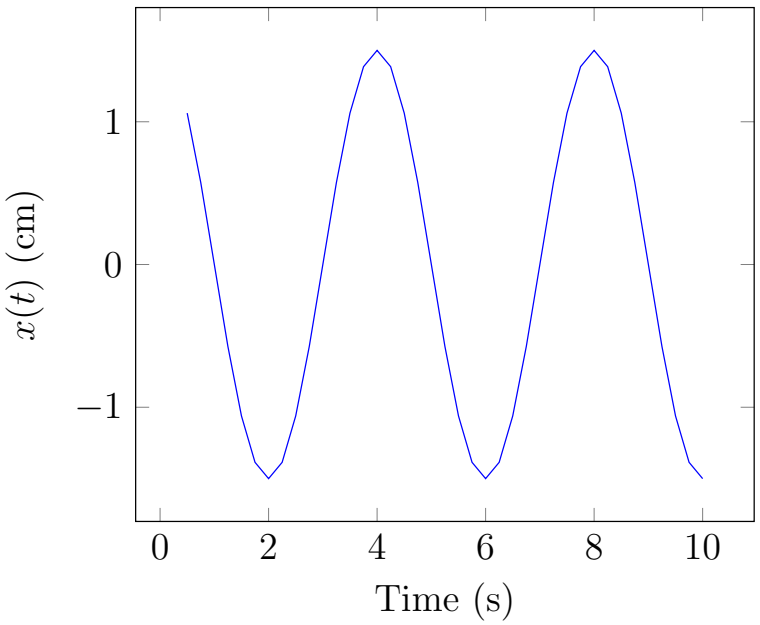

Figure 3.4 – Illustration of $x(t)$ for the ideal breathing motion model: $b_x = 1.5$ cm, $\tau_x = 4.0$ s, $\phi_x = 0$ rad.

In order to simulate more realistic breathing motions we developed other models to allow variability in motion amplitude and period and to allow unexpected events such as hiccup and cough.

To introduce variability in motion amplitude and period in the breathing model, we included random variables in the ideal breathing motion model:

$$\begin{pmatrix} x(t) \\ y(t) \\ z(t) \end{pmatrix} = \begin{pmatrix} x_0 \\ y_0 \\ z_0 \end{pmatrix} + \begin{pmatrix} b_{\text{rand x}} \cos(\frac{2\pi t}{\tau_{\text{rand x}}} + \phi_x) \\ b_{\text{rand y}} \cos(\frac{2\pi t}{\tau_{\text{rand y}}} + \phi_y) \\ b_{\text{rand z}} \cos(\frac{2\pi t}{\tau_{\text{rand z}}} + \phi_z) \end{pmatrix} \tag{3.5}$$

where $b_{\text{rand x}}$, $b_{\text{rand y}}$ and $b_{\text{rand z}}$ are the random variables, calculated for each new breathing cycle, representing the motion amplitude along the three coordinate system axis. $\tau_{\text{rand x}}$, $\tau_{\text{rand y}}$, $\tau_{\text{rand z}}$ are the random variables, also calculated for each new breathing cycle, representing the motion period for each coordinate. The breathing cycles for each axis are calculated respectively by: $\lfloor \frac{t}{\tau_x} \rfloor$, $\lfloor \frac{t}{\tau_y} \rfloor$, $\lfloor \frac{t}{\tau_z} \rfloor$. All the random variables are associated to a normal distribution. $b_{\text{rand x}}$ is associated to the probability density function:

$$g_x(u) = \frac{1}{\sigma_{bx}\sqrt{2\pi}} e^{-0.5\times\left(\frac{u-b_x}{\sigma_{bx}}\right)^2}$$

where σ_{bx} is the standard deviation of the distribution set by the user. $b_{\text{rand y}}$ and $b_{\text{rand z}}$ are similarly defined . $\tau_{\text{rand x}}$ is associated to the probability density function:

$$h_x(u) = \frac{1}{\sigma_{\tau x}\sqrt{2\pi}} e^{-0.5\times\left(\frac{u-\tau_x}{\sigma_{\tau x}}\right)^2}$$

where $\sigma_{\tau x}$ is the standard deviation of the distribution set by the user. $\tau_{\text{rand y}}$ and $\tau_{\text{rand z}}$ are similarly defined. We will later refer to this model as "*irregular breathing model*". Figure 3.5 shows an illustration of the breathing model along one axis.

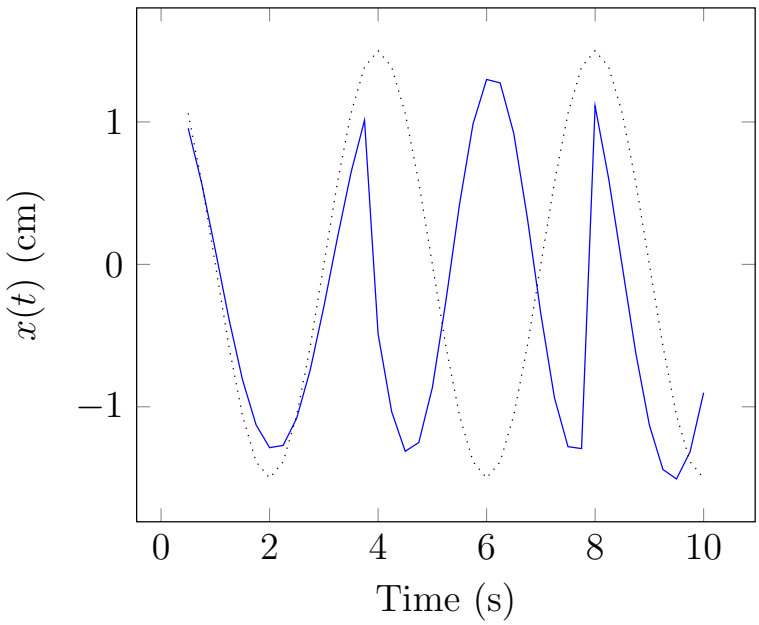

Figure 3.5 – Illustration of $x(t)$ for the irregular breathing model: $b_x = 1.5$ cm, $\sigma_{b_x} = 0.15$ cm, $\tau_x = 4.0$ s, $\sigma_{\tau_x} = 0.4$ s, $\phi_x = 0$ rad. Note: the peaks present at 4 s and 8 s are due to the random variations of $b_{\text{rand x}}$ and $\tau_{\text{rand x}}$ occurring every new cycle. The ideal breathing model is represented in dotted line.

To model unexpected events, we added variations to the motion amplitude at random dates during the delivery. These variations were applied to the *irregular breathing model*. The first event modeled, namely the *hiccup*, is considered as a periodical event starting at a random date t_{hic}, and occurring every τ_{hic} seconds during N_{hic} cycles, where t_{hic}, τ_{hic} and N_{hic} are random variables set at the motion initialization. Currently for testing, these random variables are respectively associated to a uniform distribution over $[0, 10[$ (*i.e*, the hiccup starts between 0 and 10 seconds after the beginning of the delivery), a uniform distribution over $[0, 3[$ (*i.e*, the hiccup period is between 0 and 3 seconds) and a discrete uniform distribution over $[0, 10[$ (*i.e*, the hiccup can occur between 1 and 10 times). The motion amplitude is the sum of the amplitude from the *irregular breathing model* and a random variable associated to a normal distribution of average $\frac{b_x}{2}$ (respectively $\frac{b_y}{2}$ and $\frac{b_z}{2}$) and standard deviation $\frac{\sigma_{bx}}{2}$ (respectively $\frac{\sigma_{by}}{2}$ and $\frac{\sigma_{bz}}{2}$). Figure 3.6 presents an illustration of hiccups. The second event modeled, namely the *cough*, is considered as a single event occurring at a random date obtained with a uniform distribution. For testing, this random date is currently comprised between 0 and 30 seconds. Figure 3.7 presents an illustration of a cough.

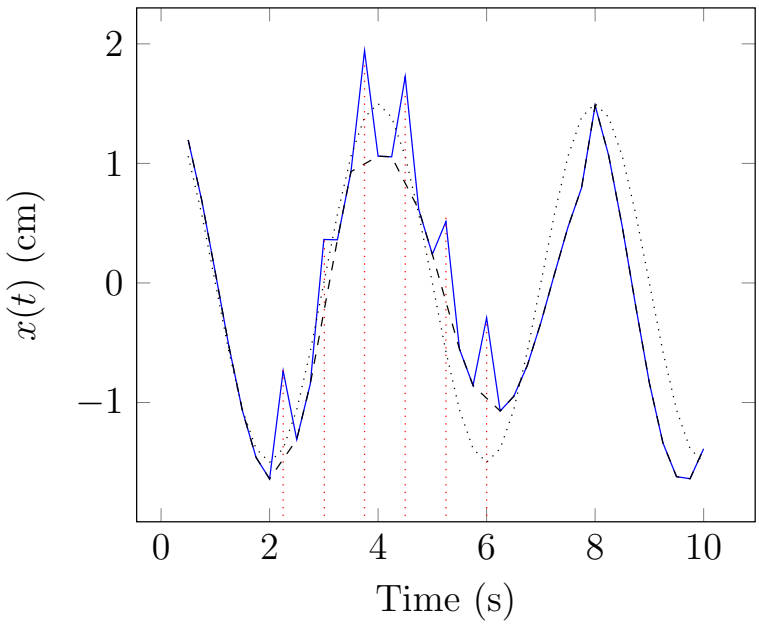

Figure 3.6 – Illustration of $x(t)$ with the hiccup model: $b_x = 1.5$ cm, $\sigma_{b_x} = 0.15$ cm, $\tau_x = 4.0$ s, $\sigma_{\tau_x} = 0.4$ s, $\phi_x = 0$ rad. Hiccups dates of hiccup are indicated by the red dotted lines. The motion without the hiccups is represented by the black dashed curve. The ideal breathing model is represented in dotted line.

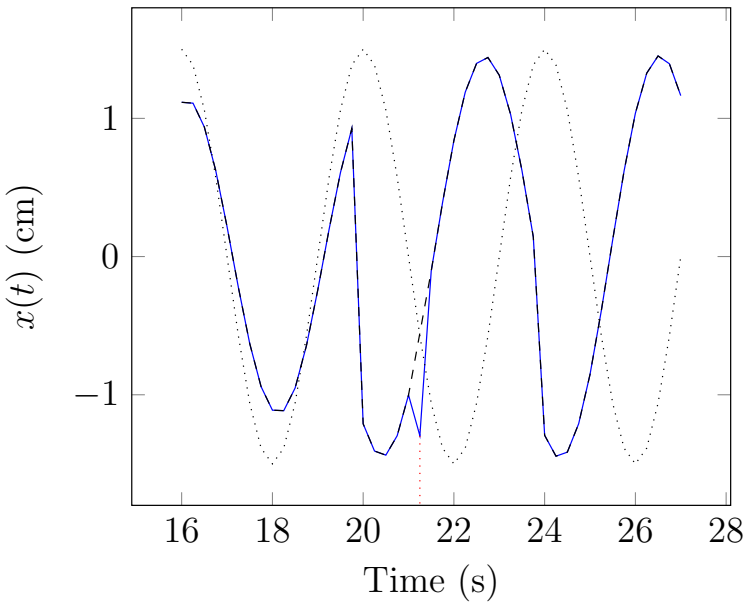

Figure 3.7 – Illustration of $x(t)$ with the cough model: $b_x = 1.5$ cm, $\sigma_{b_x} = 0.15$ cm, $\tau_x = 4.0$ s, $\sigma_{\tau_x} = 0.4$ s, $\phi_x = 0$ rad. Cough date of hiccup is indicated by the red dotted line. The motion without the cough is represented by the black dashed curve. The ideal breathing model is represented in dotted line.

Presently, the user can also import motion information as a list of dates and displacements from the initial position for each coordinate component. New motion functions

could be implemented by the user or be part of future developments of MSPT.

In order to simulate a motion monitoring system, we add to the displacement vector a "*measurement noise*" vector modeled by a random variable, for each coordinate component. Hence, the motion measured by the monitoring system is:

$$\begin{pmatrix} x_{\text{measure}}(t) \\ y_{\text{measure}}(t) \\ z_{\text{measure}}(t) \end{pmatrix} = \begin{pmatrix} x(t) \\ y(t) \\ z(t) \end{pmatrix} + \begin{pmatrix} \delta_{\text{rand x}} \\ \delta_{\text{rand y}} \\ \delta_{\text{rand z}} \end{pmatrix} \tag{3.6}$$

where $\delta_{\text{rand x}}$ is associated to the normal distribution of standard deviation $\sigma_{\delta x}$ and a mean value of 0. $\delta_{\text{rand y}}$ and $\delta_{\text{rand z}}$ are similarly defined. A new measurement noise vector is generated for each motion measurement. The parameters $\sigma_{\delta x}$, $\sigma_{\delta y}$, and $\sigma_{\delta z}$, which can be set in MSPT configuration file, model the monitoring system accuracy.

3.3 Dose calculation

We simulate the proton beams with the analytical beam model introduced by Hong et al. [1996]. As often in medical physics, the model is based on computations in water, a well-known uniform medium, and relies on a scaling procedure to another medium. The model can be presented as follows. Let us consider the Cartesian coordinate system whose origin is at the beam source and whose Z axis is along the beam. The beam source, $O(0,0,0)$ is defined by the virtual source-axis distance defined, for each beam rotation angle, in the treatment plan. This corresponds to the distance between the virtual beam source and the plan isocenter. Let $P(x,y,z)$ be a point in the patient in this coordinate system. Let $Q(0,0,z)$ be the orthogonal projection of P on the Z axis. Then, the dose d received at $P(x,y,z)$ is defined as:

$$\begin{aligned} d(x,y,z) = DD_w(rpl(z), E_0) \times \left(\frac{ssd + rpl_Q}{z}\right)^2 \\ \times \frac{1}{2\pi(\sigma_{tot_Q})^2} \times \exp\left(-\frac{x^2+y^2}{2(\sigma_{tot_Q})^2}\right) \end{aligned} \tag{3.7}$$

where:

- $rpl(z)$ corresponds to the radiological depth, at Q, defined as the thickness of water needed to obtain the same stopping power as the set of media encountered on the beam's trajectory in the patient, from the entrance point to Q. It is computed as the cumulative stopping power relative to water of each medium encountered along the beam [Szymanowski and Oelfke, 2002] using the ray-tracing algorithm presented in [Siddon, 1985]. It quantifies the energy lost by protons to reach point Q and the corresponding thickness of water needed to obtain the same energy loss.
- $DD_w(rpl(z), E_0)$ corresponds to the dose deposited in Q considering a water environment for a beam of protons of initial energy E_0.

- *ssd* is the distance from the source to the surface of the patient. It is computed using the ray-tracing algorithm previously mentioned. The distance is measured from the source to the first intersection between the ray and the patient's body surface.
- The beam's width is modeled by a two dimensional Gaussian which standard deviation is the radial emittance term σ_{tot_Q}. It corresponds to the sum of the beam's width at the patient entrance and the beam spreading function defined analytically in [Hong et al., 1996]. The beam's width at the patient entrance corresponds to the scanning spot size provided in the treatment plan, σ_{size}. The spreading function defined in [Hong et al., 1996] is:

$$\begin{aligned}\sigma_Q(rpl(z)) = (0.0275 \times R + 0.12085 \times 10^{-4} \times R^2) \\ \times (0.33 \times \left(\frac{rpl(z)}{R}\right) + 0.69 \times \left(\frac{rpl(z)}{R}\right)^2)\end{aligned} \tag{3.8}$$

  where R is the depth of the Bragg Peak for a proton beam of energy E_0. Hence, σ_{tot_Q} is computed as:

$$\sigma_{tot_Q} = \sqrt{\sigma_{size}^2 + \sigma_Q^2} \tag{3.9}$$

As previously mentioned, `MSTP` has the ability to model scanning pencil beam based on measured data or an existing beam model from other treatment planning systems. Currently, the beam was modeled after the model *"ProtonMachine"* from RayStation. In order to match the absolute dose of *ProtonMachine*'s dose distributions in water, we added a dose correction factor $\lambda(E_0)$ depending on the energy E_0, represented in Figure 3.8. Hence, Equation 3.7 becomes:

$$d_c(x, y, z) = \lambda(E_0) \times d(x, y, z) \tag{3.10}$$

where, $d_c(x, y, z)$ is the dose calculated by `MSPT` at P. Physically, the correction factor $\lambda(E_0)$ accounts of the change of Monitor Unit (MU) response at different proton energies, as the plan imported and computed in `MSPT` aims at performing absolute dose computation with input MU for each beam. Users can easily define the λ correction factor to match their proton machine.

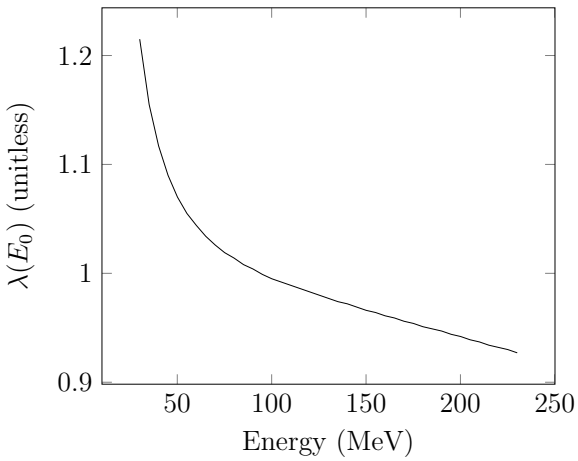

Figure 3.8 – Dose correction factor λ as a function of energy.

The dose correction factors are obtained through simulations of 1 MU pencil beams in a volume of water for different energy levels. A first simulation, for a given energy E_0, in *ProtonMachine* provides a dose distribution with an average dose of d_1. The same simulation in `MSPT`, with a dose correction factor of 1.0, provides an average dose of d_2. The dose correction factor for E_0 is calculated as: $\lambda(E_0) = \frac{d_1}{d_2}$.

In order to match the stopping power values used in *ProtonMachine* for various densities, we apply a multiplying factor to the stopping power obtained from PSTAR database. The multiplying factor depends on the density and is represented in Figure 3.9. It mainly has an impact on low densities up to 0.8 $g.cm^3$, after what it stays close to 1. Physically, this factor aims at correcting the approximation made when calculating the stopping power for tissues whose densities are comprised between the ones of air (1.2×10^{-3} $g.cm^3$) and adipose (0.9 $g.cm^3$), which were the only body media available in PSTAR for density lower than 0.9 $g.cm^3$. This correction factor can also be user-defined.

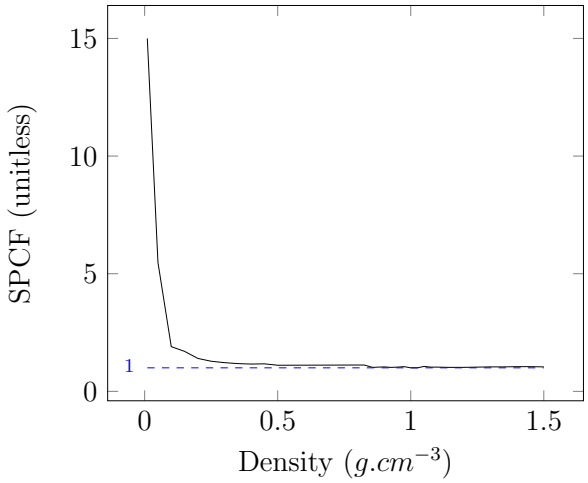

Figure 3.9 – Stopping power correction factor (SPCF) as a function of mass density.

The correction factor was obtained through simulations of a single proton pencil beam, of fixed energy, in an homogeneous medium, of a given density, using *ProtonMachine* and `MSPT` where the correction factor was set to 1.0. In both dose distribution computed, we measured the distance between the beginning of the ray in the medium and the Bragg Peak. Then, we calculated the ratio of these distances, which correspond to the scaling factor γ of the given density: $\gamma = \frac{d_1}{d_2}$, where d_1 and d_2 are respectively the distances measured in the dose grid obtained respectively from *ProtonMachine* and `MSPT`. γ corresponds also to the ratio of the radiological depth, which will be introduced in the next section. γ calculation relies on the assumption that the Bragg Peak occurs, for a given medium, at the same depth in *ProtonMachine* and in `MSPT`. We repeated this process for a set of densities in the range 1.205×10^{-3} $g.cm^{-3}$ to 1.85 $g.cm^{-3}$. In media of low density the Bragg Peak can occur outside the volume considered for the simulation if the medium m represented is not thick enough. Therefore, when the Bragg Peak is outside this volume a slab of water can be added such that the Bragg Peak occurs in water. Then,

$\gamma = 1 + \frac{d_{w2} - d_{w1}}{d_{m1} \times S_{mw}}$, where d_{w1} and d_{w2} are the depths in water where the Bragg Peak occurs respectively in the dose distribution of the *ProtonMachine* and `MSPT`. d_{m1} is the thickness of m penetrated by the beam which is the same in both dose distributions. Note that d_{m1} should be greater than the thickness of the slab of water for a better accuracy. Finally, S_{mw} is the relative proton stopping power of m.

The depth-dose curves of the energies of reference have been generated from simulations of mono-energetic proton beams in water using *ProtonMachine*. This dose computation was later also used to benchmark the accuracy of `MSPT`. To generate these integral depth dose curves, we integrated the 3D dose distribution obtained along the X and Y axis to obtain the dose along the depth, *i.e.*, Z axis. To obtain the integral depth-dose curves for other energies, later referred to as "*interpolated energies*", we interpolate between those already generated. The interpolation for a desired energy E_1, starts with finding the two consecutive energies E_0 and E_2 in the list of "*energies of reference*" such that $E_0 < E_1 < E_2$. Using a linear interpolation between the Bragg Peak positions BP_0 and BP_2, respectively for E_0 and E_2, we obtain the Bragg Peak location BP_1 for E_1. Then, we shift the depth-dose curve of E_2, along Z, by the difference between BP_2 and BP_1 and keep the portion of the curve where the depth is positive. Finally, we scale the curve by a factor α to ensure that the number of protons used in a 1MU beam of energy E_2 is preserved, as performed in *ProtonMachine*. To do so, we compute the number of protons (N_{E_2}) used to reach 1MU at E_2 as:

$$N_{E_2} = \frac{A_{E_2} \times \rho_{water}}{E_2} \tag{3.11}$$

where A_{E_2} is the area under the depth-dose curve in $[Gy.cm^3]$, ρ_{water} the water density in $[Kg.cm^{-3}]$ and E_2 the energy expressed in Joules. Then, we calculate the area under the current depth-dose curve for E_1 (*i.e*, $A_{E_1 curr}$). Finally, we calculate the scaling factor α between the expected area under the curve for E_1 (*i.e*, A_{E_1}) and $A_{E_1 curr}$, in order to have the same number of protons equals to N_{E_2}. Hence, we obtain:

$$\alpha = \frac{A_{E_1}}{A_{E_1 curr}} = \frac{N_{E_2} \times E_1}{\rho_{water} \times A_{E_1 curr}} \tag{3.12}$$

where E_1 is expressed in Joules. Depth-dose curves used by `MSPT` can also be user-defined.

3.4 Delivery process

To simulate the delivery, `MSPT` follows the order of beam angles, energy layers (delivered from the highest energy to the lowest), spot positions and delivery duration (*i.e.*, spot weights) provided by the plan. In order to be able to compute the dose distribution in 4D and to render its evolution in the entire volume at a low time scale, we divide the time spent by the beam at a position, *e.g.*, 10 ms, into units of time of, for example, 1 ms, between which we consider the patient as non-static. Therefore, every unit of time the patient position and the radiological depth are updated using the motion information.

The dose distribution corresponding to the new position is then computed.

In order to take the time into account during the delivery, we created a timer, representing the time during the delivery. This timer is updated based on events occurring during the delivery. Table 3.1 summarizes events having a fixed duration during the delivery. Through `MSPT` configuration file, the user can easily set new values for these events.

Action	Duration	Condition	Source
Gantry rotation	1 rpm	None	[Ding et al., 2007]
Energy transition	50 ms	Cyclotron	[Schippers et al., 2007]
Energy transition	2.1 s	Synchrotron	[Smith et al., 2009]
Spill duration	5s	Synchrotron	[Kraus et al., 2011]
Lateral scanning speed	10 $m.s^{-1}$	None	[Kraus et al., 2011], [Kang et al., 2007]
Vertical scanning speed	10 $m.s^{-1}$	None	[Kraus et al., 2011], [Kang et al., 2007]

Table 3.1 – Temporal values of some delivery's events.

Two other events, whose duration depends partly on the treatment plan, were also considered: the time needed to move the beam from one position to another and the time spent at a spot position. The former event's duration is calculated as follows:

$$t_{\text{move}} = max\left(\frac{\mid p_x^{i+1} - p_x^i \mid}{v_{lateral}}, \frac{\mid p_y^{i+1} - p_y^i \mid}{v_{vertical}}\right) \tag{3.13}$$

where $p^i = \binom{p_x^i}{p_y^i}$ is the current beam position, $p^{i+1} = \binom{p_x^{i+1}}{p_y^{i+1}}$ is the next position, $v_{lateral}$ is the lateral scanning speed, and $v_{vertical}$ is the vertical scanning speed. The time the beam needs to remain at a position is fixed, in the treatment plan, by the weight in MU:

$$t_{\text{spot}} = \frac{\text{weight } [MU] \ \times \text{number of protons per MU } [protons.MU^{-1}]}{\text{extraction rate } [protons.s^{-1}]} \tag{3.14}$$

The number of protons per MU used in *ProtonMachine* is 1×10^9. According to Grözinger et al. [2008] the typical time per beam position is around 5 to 10 ms. Hence we considered it to be 10 ms and using the average beam's weight of 0.073 MU obtained in a real treatment plan computed with *ProtonMachine*, we fixed the extraction rate to 7.3×10^{10} $protons.s^{-1}$. The number of protons per MU and the extraction rate are parameters that can be modified by the user in `MSPT` configuration file.

Chapter 4

Simulator evaluation

In order to assess the consistency of the dose calculations in `MSPT` we performed a series of evaluations using *ProtonMachine* as a benchmark.

A first part of the evaluation consists of simulations of single mono-energetic proton beams in a volume of water. Water, being a well-known medium, is often used as a reference for calculations or experiments in radiation therapy physics. For example, depth-dose curves of reference used for dose calculation in commercial TPS are obtained from analysis of beams in water. In calculations, the data in water is scaled or transformed to be used for other media. A second part of the evaluation consists of simulations for patient cases in order to assess the coherency of the dose calculation in environments more complex than water. The last part of the evaluation consists of a comparison between a static delivery and a dynamic delivery in `MSPT` to show the impact of motion.

4.1 Simulations in water

First we compared the dose distributions obtained in water for many energies using *ProtonMachine* and `MSPT`. We simulated in `MSPT` mono-energetic proton beams of 1 *MU* in a volume of water for the "*energies of reference*" (*i.e.*, energies ranging from 30 MeV to 230 MeV, with a 5 MeV step) and 19 "*interpolated energies*" in the range 39 MeV - 119 MeV, corresponding to the set of energies used in a patient treatment plan. Then, we computed the same beams in *ProtonMachine*. Finally, we compared the dose distributions considering, for each energy, the depth-dose curve, the location of the Bragg Peak and the lateral dose profiles at the Bragg Peak using the standard deviation σ of the Gaussian curves obtained.

Figure 4.1 shows examples of dose profiles obtained at 55, 130 and 210 MeV. The average ($\pm$ standard deviation) and the median of the dose errors observed for the energies of reference were 0.2% ($\pm$ 2.5%) and 0%. These statistics were 2.4% ($\pm$ 11.9%) and 0% for interpolated energies. In the former case, 99% of the sample points of the depth-dose profiles had a dose error smaller than 5% and 93% in the latter case.

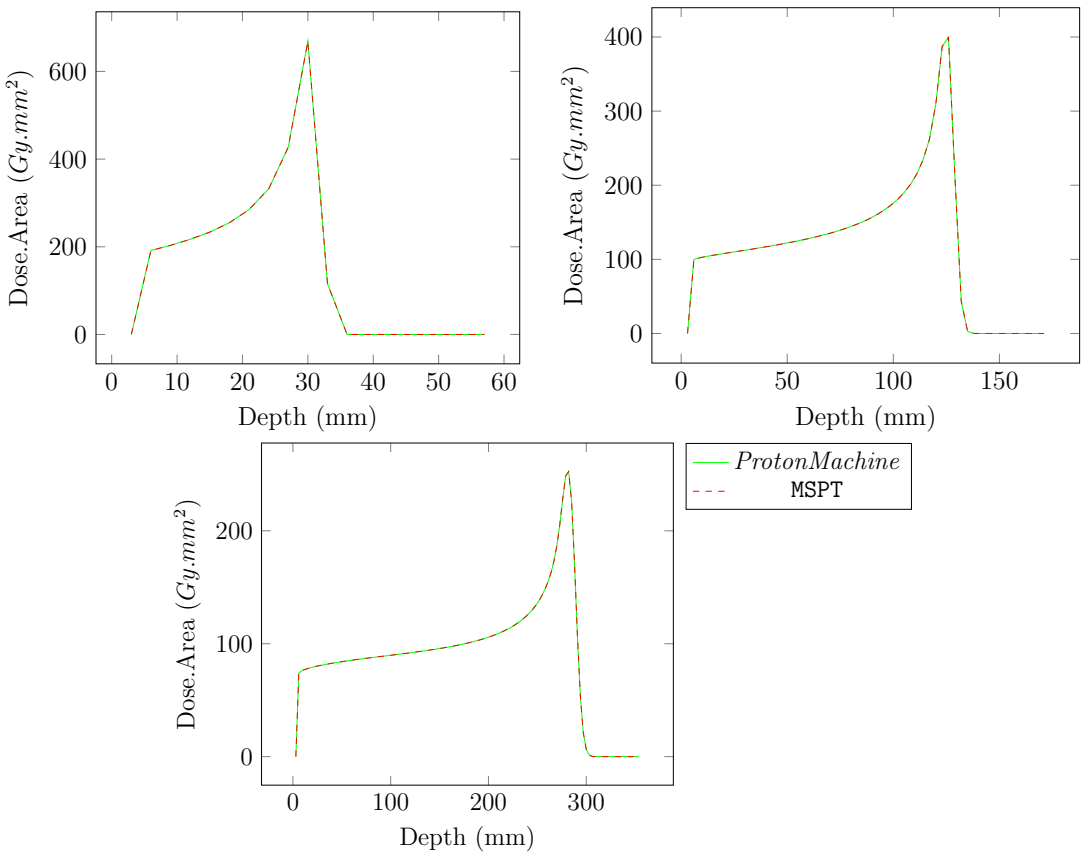

Figure 4.1 – Plot representing the depth dose curve for the beamlet dose distributions obtained at 55 MeV, 130 MeV and 210 MeV (respectively top left, top right and bottom) with *ProtonMachine* and `MSPT` in water, for the same monitor units.

We compared the Bragg Peak location for each energy level in the sets of energies of reference and interpolated energies (see Figure 4.2). One can notice that `MSPT` matches closely the depths of Bragg Peaks obtained with *ProtonMachine*. For the energies of reference, no difference was found in the Bragg Peak location. Regarding interpolated energies (39 - 119 MeV), an average error of 1.1 mm (± 1.5 mm) was found. This is acceptable considering the dose grid size of 3 mm.

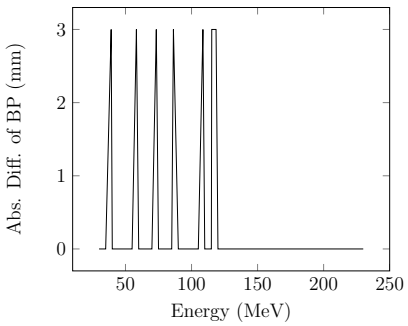

Figure 4.2 – Absolute difference of Bragg Peak depth for beamlets simulated with *ProtonMachine* and `MSPT` for energies ranging from 30 MeV to 230 MeV in water.

We further analyzed the lateral dose profiles at the Bragg Peak from *ProtonMachine* and `MSPT`. As illustrated in Figure 4.3 for given energies (55, 130 and 210 MeV), they are in agreement. In Figure 4.4, we plot the differences between the standard deviation, σ, computed from the lateral profiles being considered as Gaussian curves for each energy. The average difference of σ, for the energies of reference, is 0.17 mm ($\pm$ 0.16 mm). Regarding interpolated energies, the average difference found was 0.06 mm ($\pm$ 0.03 mm). In both sets, the error is smaller than the dose grid-resolution. The average difference is smaller for interpolated energies since these energies are only in the low and medium energy range ($<$ 119 MeV).

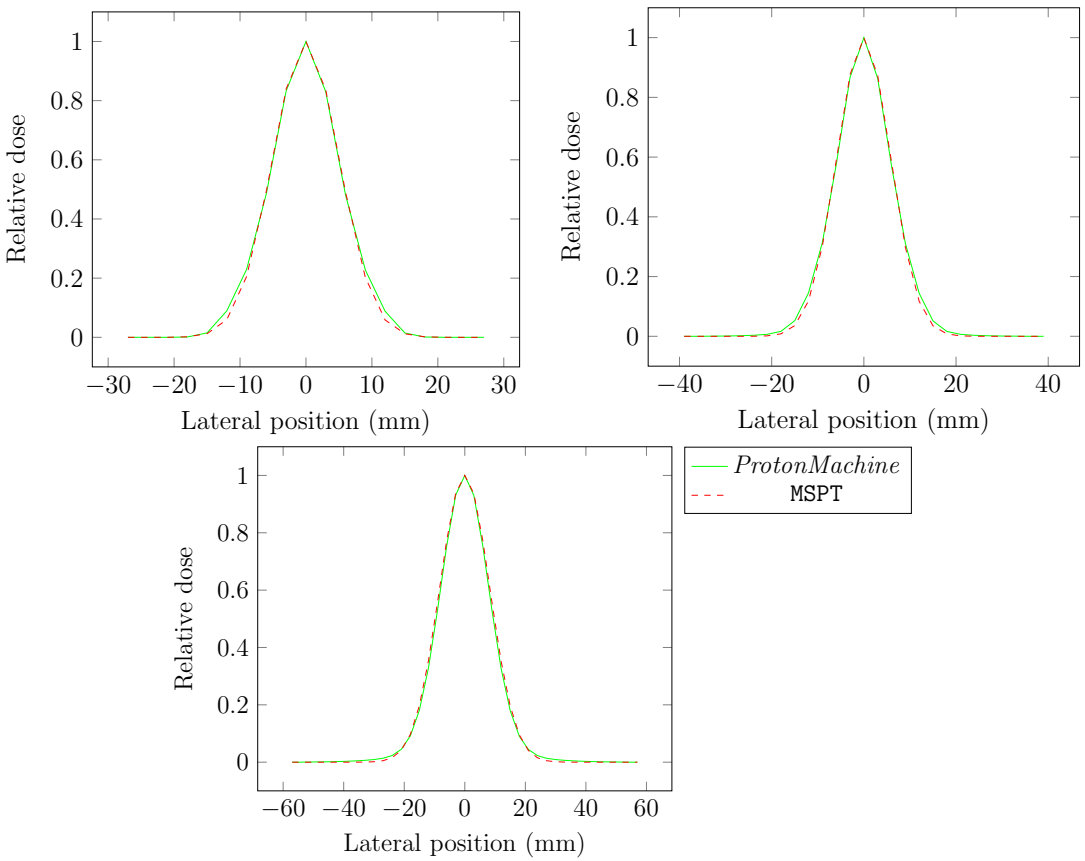

Figure 4.3 – Plot representing the lateral profiles at the Bragg Peak for the beamlet dose distributions obtained at 55, 130 and 210 MeV (respectively top left, top right and bottom) with *ProtonMachine* and `MSPT` in water.

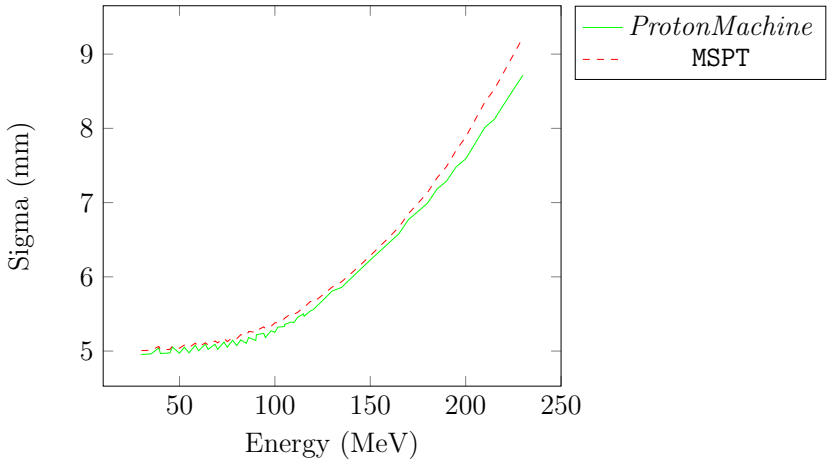

Figure 4.4 – Plot representing sigma for the dose distributions computed in *ProtonMachine* and `MSPT` for energies ranging from 30 MeV to 230 MeV in water.

In this verification process we observed that the dose distributions obtained for the energies of reference were matching closely the dose distribution obtained with *ProtonMachine*. For the interpolated energies, larger errors were observed at the Bragg Peak depth or the fall-off after the Bragg Peak. The evaluation of the Bragg Peak positions for this set of energies showed that the average error was 1 mm: 7 energies had an error of 3 mm, corresponding to the dose grid resolution, and 12 of them were correctly located. Moreover, the Bragg Peak location easily induces large dose errors especially when a slight shift of the depth of the Bragg Peak has occurred. This explains why the standard deviation of the dose error for interpolated energies is large while only 7% of the sample points used in the depth-dose profiles had an error larger than 5%. For both sets of energies, the error of σ stayed smaller than the grid resolution. The difference observed at high energies can be explained by the consideration of nuclear interactions in *ProtonMachine* beam's spreading model unlike `MSPT`. Overall, we can observe similar trends for both σ curves. Therefore, the `MSPT` model of the beam's spread is consistent with *ProtonMachine*'s. As `MSPT` aims at evaluating and comparing the effect of motion on different plans or different motion management/mitigation strategies, the absolute dose accuracy is not of highest concern; we consider the dosimetric accuracy achieved in `MSPT` as acceptable for its purpose.

4.2 Simulations on patient datasets

A second part of `MSPT` evaluation focused on the dose distributions simulated for 8 patient cases with different treatments summarized in Table 4.1.

Tumor Location	Patient Index	Tumor size (cm^3)	Beam angle(s) ($degrees$)	Prescription per fraction (Gy)
Head and neck	HN1	89	180	1.8
Lung	Lung1	143	220 / 320	1.8
Lung	Lung2	21	270	2
Lung	Lung3	89	180	1.8
Lung	Lung4	28	200	6
Lung	Lung5	21	15	10
Lung	Lung6	207	180	15
Pelvis	Pelvis1	1447	90 / 270	2.16

Table 4.1 – Patient cases summary

First, we will present the most representative cases: one case (Lung1) that shows an excellent match with *ProtonMachine*, and one case (Lung6) that highlights an artifact observed when comparing `MSPT` to *ProtonMachine*. Then we will present the overall comparisons.

4.2.1 Example of patient case simulation

The first example of a patient case simulation is for a lung tumor treatment (Lung1 in Table 4.1). We compare the dose distributions planned and calculated with *ProtonMachine* and re-computed in `MSPT`. We analyze, for both distributions, the dose-volume histogram, which is the principal tool used by clinicians to evaluate the quality of a treatment plan. The size of the lung tumor is $143cm^3$(GTV). It relies on 2 beams with gantry angles of 220° and 320°. The dose prescription is $180cGy$ per fraction. To compare the DVHs quantitatively, we consider dosimetric parameters, which are often used to assess the quality of a treatment plan: the dose delivered to 95% ($D_{95\%}$) and 5% ($D_{5\%}$) of the tumor volume and the normalized volume of different body tissues receiving a given percentage of the prescribed dose: 10% (V_{10}), 33%(V_{33}), 50%(V_{50}), 66%(V_{66}) and 90%(V_{90}). We also compare the mean dose received by these tissues (D_{mean}). In addition, we perform a 3D gamma test [Low et al., 1998] to analyze the differences between the distributions.

Figure 4.5 shows the resulting DVHs for *ProtonMachine* and `MSPT`. We can observe that they are similar. Tables 4.2 and 4.3, summarize the dosimetric parameters measured in dose distributions obtained in *ProtonMachine* and `MSPT`, respectively for the tumor and other body tissues.

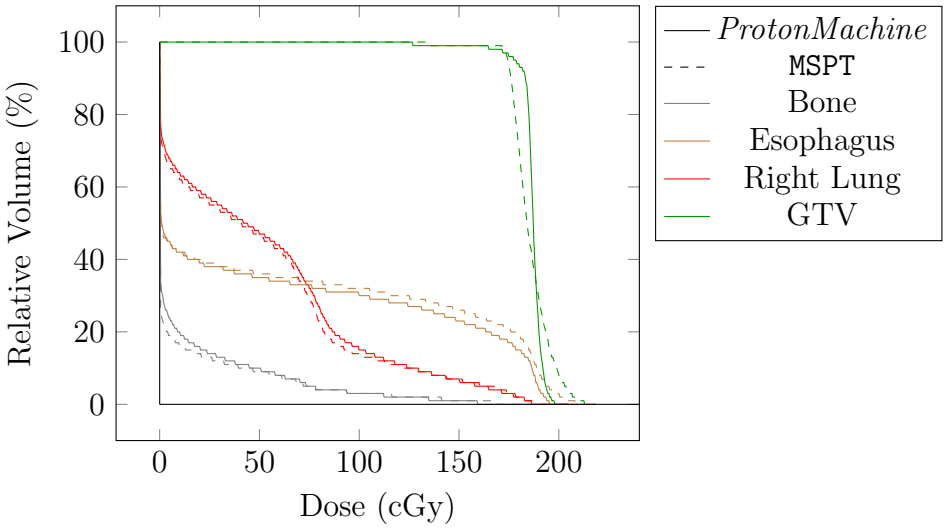

Figure 4.5 – DVH comparison between *ProtonMachine* and `MSPT` for the lung tumor case.

Tissue	$D_{95\%}$ (cGy)		$D_{5\%}$ (cGy)	
	ProtonMachine	`MSPT`	*ProtonMachine*	`MSPT`
GTV	178.5	174.5	193.5	203.5

Table 4.2 – Dose received by 95% and 5% of the tumor volume for simulations in *ProtonMachine* and in `MSPT`.

Tissue	Software	$V_{10}(\%)$	$V_{33}(\%)$	$V_{50}(\%)$	$V_{66}(\%)$	$V_{90}(\%)$	D_{mean}(cGy)
Bone	*ProtonMachine*	16	8	4	2	0	11.87
	`MSPT`	14	8	4	2	1	10.85
Right Lung	*ProtonMachine*	60	44	19	11	5	53.63
	`MSPT`	58	42	16	10	5	51.68
Esophagus	*ProtonMachine*	40	34	31	28	21	56.65
	`MSPT`	40	35	33	30	24	61.18

Table 4.3 – Volume receiving 10, 33, 50, 66 and 90 % of the prescribed dose and the average dose received by the OARs in *ProtonMachine* and in `MSPT`.

The tumor coverage between *ProtonMachine* and `MSPT` was comparable. The error was 2.24% for $D_{95\%}$ and 5.16% for $D_{5\%}$. Moreover, considering the other tissues, the average differences of relative volume were small: 1.3%, 1.0%, 1.7%, 1.0% and 1.3% respectively for V_{10}, V_{33}, V_{50}, V_{66} and V_{90}. The average difference of the mean dose received by the OARs (D_{mean}) was 6.7%. In addition, the 3D gamma analysis comparing the dose distributions from *ProtonMachine* and `MSPT` yielded a passing rate of 96% using a standard threshold of 3 mm / 3%; showing an excellent match between the computed data and the data used as a benchmark. The good agreement between them was also confirmed visually (see in Figure 4.6) when overlaying the dose distributions and the patient CT image.

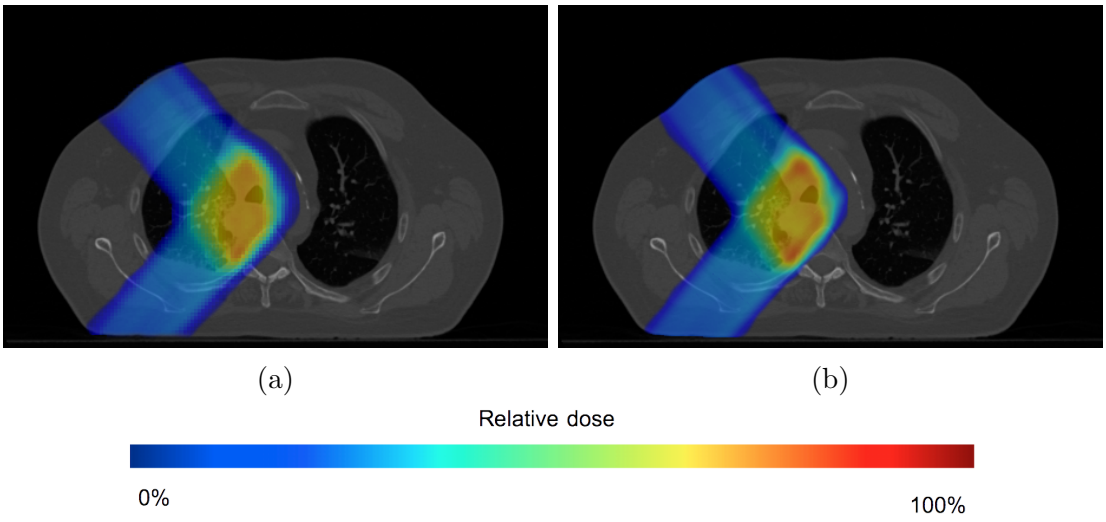

Figure 4.6 – Dose distributions computed in *ProtonMachine* (4.6a) and in `MSPT` (4.6b) overlaying the patient CT image (transverse plane located near the middle of the tumor).

The comparisons of the dose distributions in patient data sets showed that those computed in `MSPT` were in agreement with those from *ProtonMachine*. The differences are clinically acceptable based on the DVH distribution and a 3D Gamma passing rate of 96% using 3 mm / 3% criteria.

4.2.2 Artifact observed in the dose distribution

An artifact was observed when comparing the dose distributions obtained from the *ProtonMachine* and simulated in `MSPT`. We will present this artifact on the following Stereotactic Body Radiation Therapy (SBRT) lung tumor case (Lung6 in Table 4.1): the size of the tumor is 208 cm^3(PTV). It relies on a single beam with a gantry angle of 180°. The dose prescription is 1.5 Gy per fraction.

Figure 4.7 presents images of the resulting dose distributions. Figure 4.8 shows the DVHs obtained from *ProtonMachine* and `MSPT`. One can note that a part of the PTV received a higher dose in `MSPT` than in *ProtonMachine*, which corresponds to hot spots, and that a part of the right lung received a lower dose, which correspond to cold spots. These hot and cold spots can be located more clearly in Figure 4.9. This artifact was observable in the different data sets but was not always as clear as in this example.

Since this problem occurred in the different data sets, we can consider that this artifact is a systemic error. We investigated the source of this problem without finding a clear origin. However, the main assumption is that differences appear in the radiological depth between *ProtonMachine* and `MSPT`, which could result in a non exact matching of the stopping power values assigned to the density values in both software. If one, wanted to match exactly `MSPT` to *ProtonMachine*, a deeper study should be performed to assert or refute our assumption and obtain a more accurate stopping power correction factor (see

Section 3.3). In the context of our work, the goal being to compare static and dynamic situation, to render the impact of motion, this study was not decisive and therefore, we did not led further the investigation.

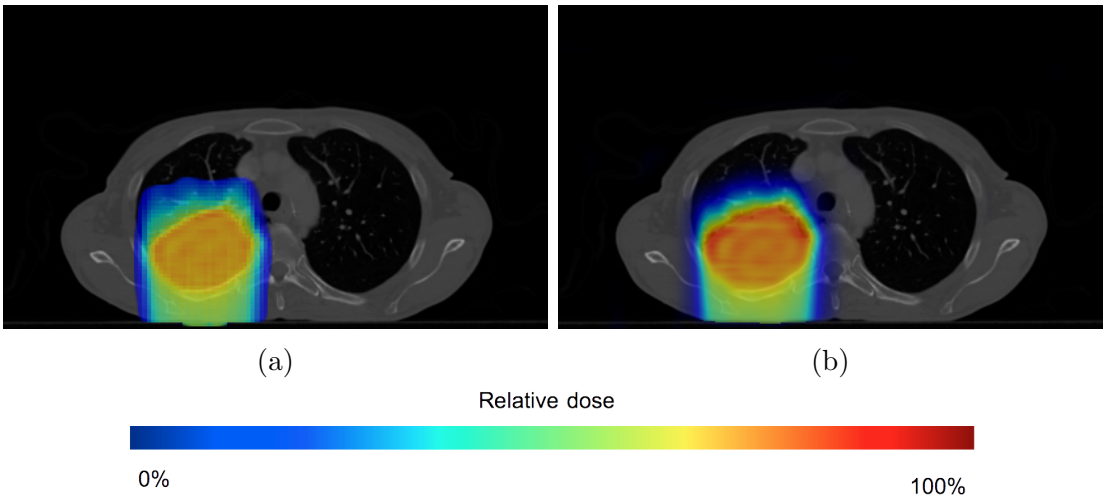

Figure 4.7 – Dose distributions computed in *ProtonMachine* (4.12e) and in `MSPT` (4.12f) overlaying the patient CT image (transverse plane located near the middle of the tumor).

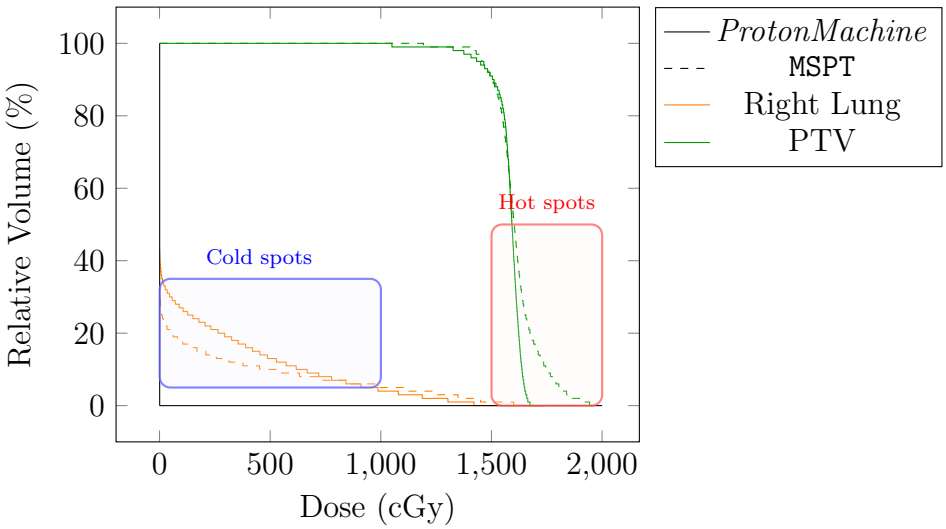

Figure 4.8 – DVH comparison between *ProtonMachine* and `MSPT`: observation of hot spots in the PTV and cold spots after the tumor (right lung) in `MSPT` dose distribution.

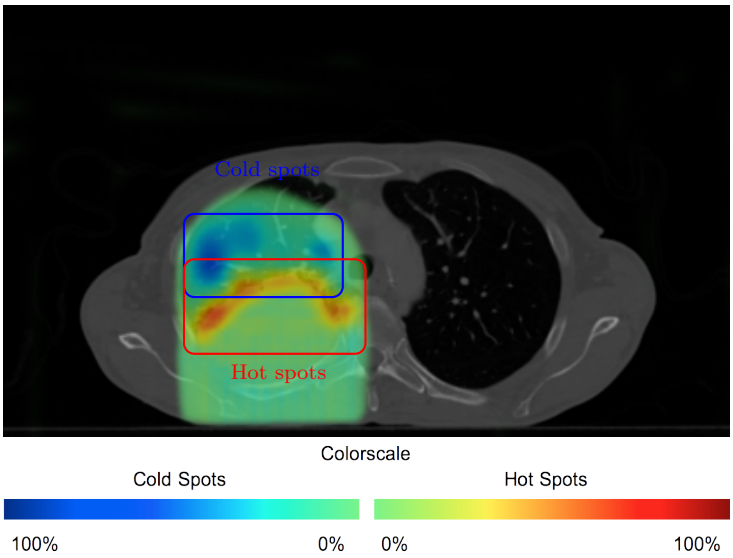

Figure 4.9 – Hot and cold spots (respectively located by the red and blue rectangles) present in the comparison of the dose distributions (Figure 4.7). They are overlaying the patient CT image. The rectangles correspond to the hot and cold spots indicated in Figure 4.8.

4.2.3 Overall comparison

To compare the dose distributions of all the patient cases we consider the following DVH dosimetric parameters: the dose delivered to 95% ($D_{95\%}$) and 5% ($D_{5\%}$) of the tumor volume and the normalized volume of different body tissues receiving a given percentage of the prescribed dose: 10% (V_{10}), 33%(V_{33}), 50%(V_{50}), 66%(V_{66}) and 90%(V_{90}). We also compare the mean dose received by these tissues (D_{mean}). The gamma analysis, requiring a lot of time and being carried out by our collaborators, is not performed on all the patient cases. Therefore, we don't use this criterion in our comparison. Figures 4.11 and 4.12 show the resulting dose distributions obtained for the different patients in *ProtonMachine* and in `MSPT`. Figure 4.10 presents the resulting DVHs. Tables 4.4 and 4.5 provide the dosimetric measures respectively for the tumor and the OARs.

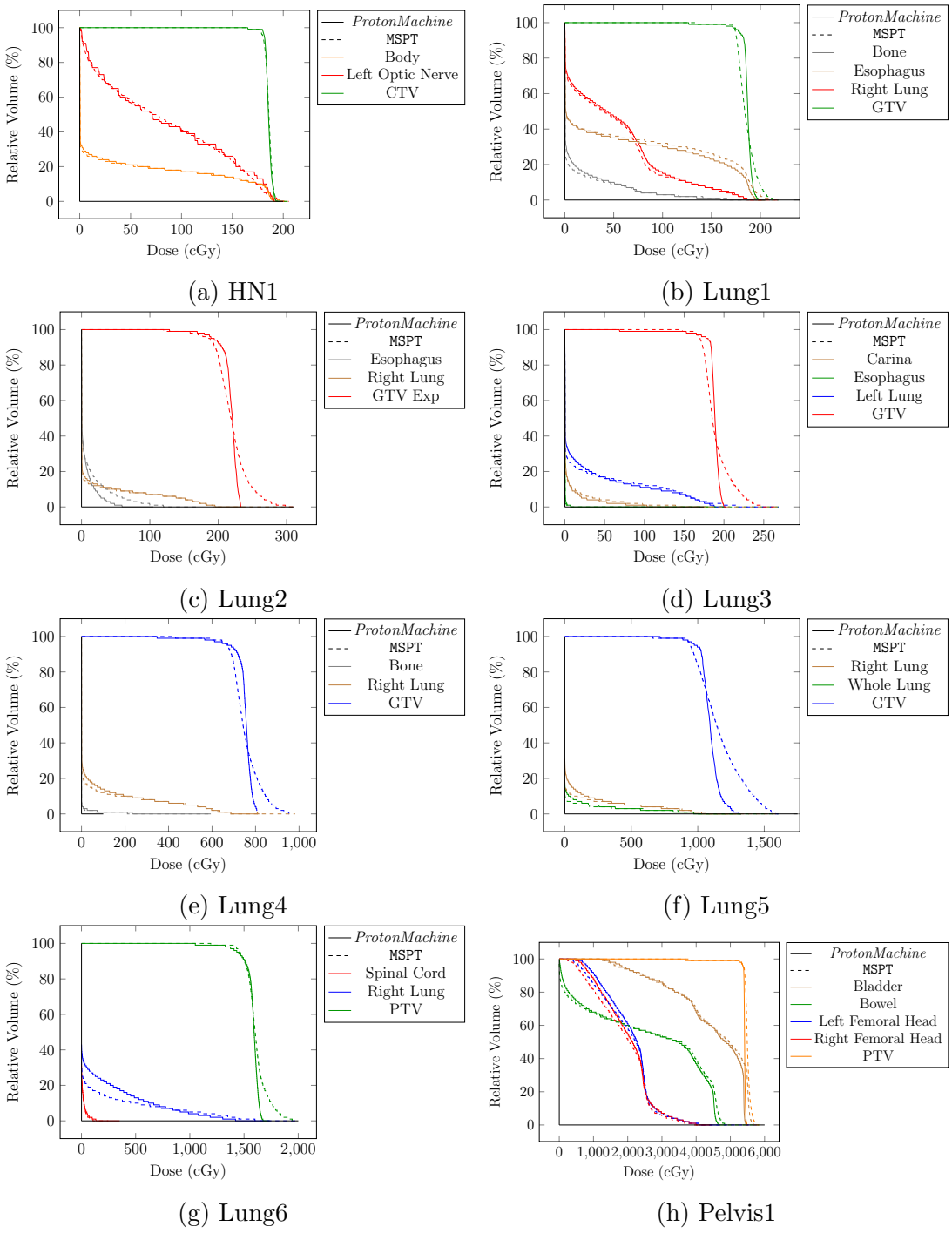

(a) HN1 (b) Lung1

(c) Lung2 (d) Lung3

(e) Lung4 (f) Lung5

(g) Lung6 (h) Pelvis1

Figure 4.10 – DVHs of the 8 patient cases for *ProtonMachine* and `MSPT`

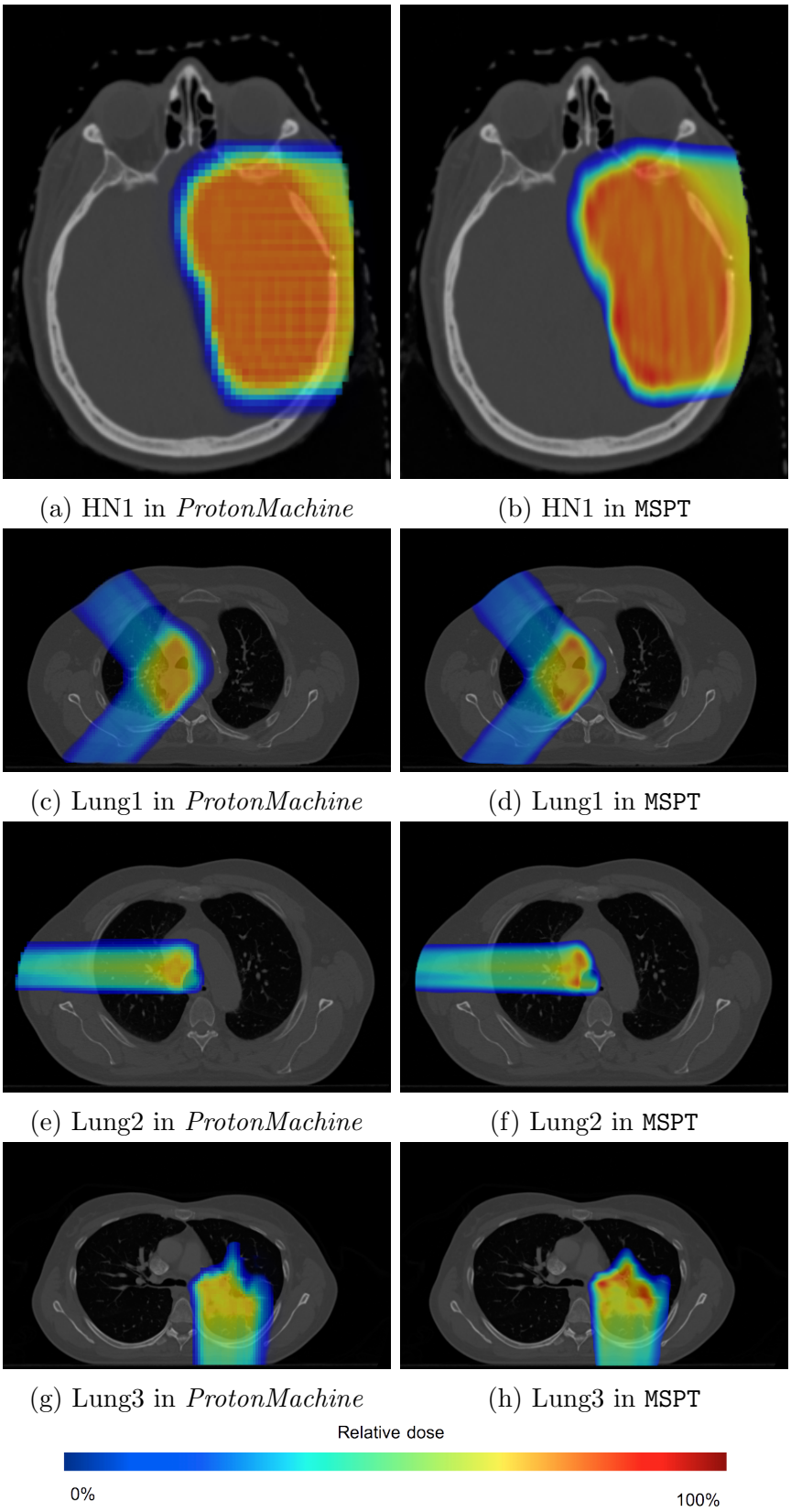

(a) HN1 in *ProtonMachine* (b) HN1 in `MSPT`

(c) Lung1 in *ProtonMachine* (d) Lung1 in `MSPT`

(e) Lung2 in *ProtonMachine* (f) Lung2 in `MSPT`

(g) Lung3 in *ProtonMachine* (h) Lung3 in `MSPT`

Figure 4.11 – Images of the dose distributions of patient cases HN1, Lung1, Lung2 and Lung3 for *ProtonMachine* (left column) and `MSPT` (right column).

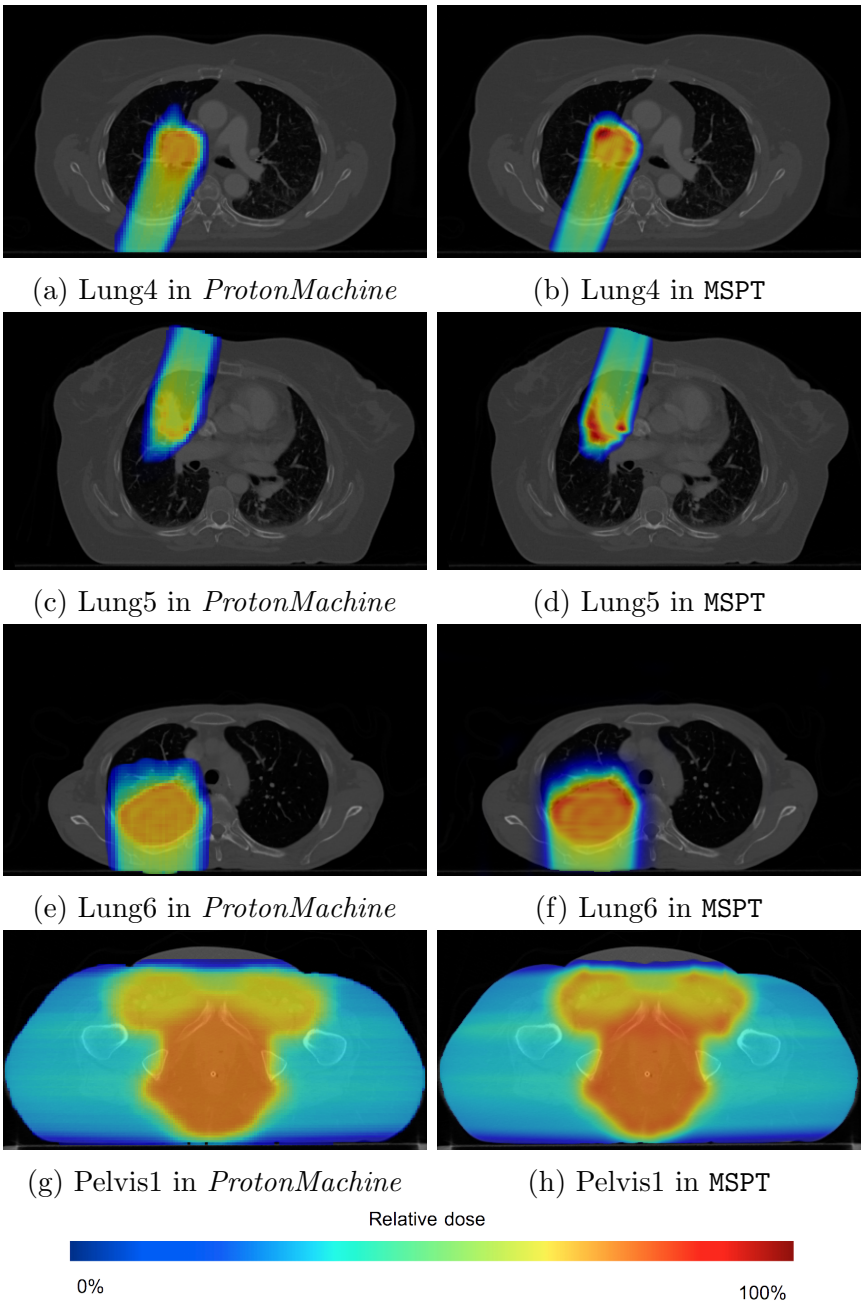

(a) Lung4 in *ProtonMachine* (b) Lung4 in `MSPT`

(c) Lung5 in *ProtonMachine* (d) Lung5 in `MSPT`

(e) Lung6 in *ProtonMachine* (f) Lung6 in `MSPT`

(g) Pelvis1 in *ProtonMachine* (h) Pelvis1 in `MSPT`

Figure 4.12 – Images of the dose distributions of patient cases Lung4, Lung5, Lung6 and Pelvis1 for *ProtonMachine* (left column) and `MSPT` (right column).

Patient	HN1	Lung1	Lung2	Lung3	Lung4	Lung5	Lung6	Pelvis1
$D_{95\%}$ error (%)	1.91	2.84	2.60	7.77	1.48	3.86	3.03	0.01
$D_{5\%}$ error (%)	0.51	3.86	9.68	15.96	8.38	42.23	9.77	0.16

Table 4.4 – Average error of the dosimetric parameters in the tumor volumes of the different patient cases. The error is relative to the maximum dose of the tumor volume.

Patient	V_{10} error (%)	V_{33} error (%)	V_{50} error (%)	V_{66} error (%)	V_{90} error (%)	D_{mean} error (%)
HN1	2.50	0.99	1.00	1.00	0.00	0.69
Lung1	1.33	1.00	1.67	0.99	1.33	6.74
Lung2	3.50	2.00	0.50	0.00	0.00	41.62
Lung3	1.33	0.67	0.67	0.67	0.00	30.38
Lung4	2.00	0.00	0.00	0.00	0.00	6.44
Lung5	2.50	0.50	0.00	0.00	0.00	8.09
Lung6	4.50	1.00	0.00	1.00	1.50	12.76
Pelvis1	2.25	2.25	1.25	1.00	0.50	2.90

Table 4.5 – Average error of the dosimetric parameters in the OARs of the different patient cases.

Visually, from Figures 4.11 and 4.12, we can say that dose distribution appear similar except at the border of the tumors where overdosed regions are visible (in red). The visual comparison of the DVHs (see Figure 4.10) indicates that in both software the dose-volume curves follow the same trend and the same order of magnitude. In addition, the error for the $D_{95\%}$ and $D_{5\%}$ values (see Table 4.4) are respectively 2.35% and 9.55%. The comparison of the dose distributions in the OARs (see Table 4.5) indicates that the average dose received differs by 13%. The large dose differences in the OARs, more specifically for cases Lung2 and Lung3, are located in organs filled with air: carina and esophagus. However, in Table 4.5 we can note that the differences of volume receiving a certain percentage of the prescribed dose are smaller than 5% and that the largest differences represent less than 10% of the dose prescription.

Based on the average error for the $D_{95\%}$ value, we can say that the dose coverage, which is the principal goal of the treatment, obtained in `MSPT` is comparable to the coverage in *ProtonMachine*. The main difference observed is at the border of the tumor, as described in Section 4.2.2. The $D_{5\%}$ error and the overdosed regions in the dose distribution images indicate this difference. In addition we can observe that the error is larger in lung cases. That is why we think that the presence of lungs on the beam's trajectory impacts the dose calculation. Lungs density lies in the range between air (1.2×10^{-3} $g.cm^{-3}$) and adipose (0.9 $g.cm^{-3}$), where the stopping power correction factor (see Section 3.3) is important. This factor improved significantly this problem but did not remove it entirely. That is why we think that the mass stopping power factor function could be refined to improve its accuracy. In addition, the stopping power being the key element of the radiological depth, this strengthens our assumption that the artifact is due to the radiological depth. The mean dose difference for the OARs represent is around 13%, which is higher than the 5% acceptability threshold. However this difference at the scale of the treatment represents less than 10% of the dose prescription. Than is why we can observe that the DVH curves of `MSPT` and *ProtonMachine* are close. Therefore, we can consider that the dose distributions of `MSPT`, while not being comparable, are coherent with the dose calculation in *ProtonMachine*. The source of the dose differences for the OARs has not been found, but might be the result of the overdose occurring in the tumor.

To conclude we can say that `MSPT` reproduces the expected dose coverage, but overdoses the border of the tumor especially in lung cases. This might impact the dose distribution

in the OAR and explain the dose differences but this has not yet been proven. However, DVHs present the same overall trend and the same order of magnitude as *ProtonMachine*. So we can we can consider that the dose distributions of `MSPT`, while not being comparable for all cases, are coherent with the dose calculation in *ProtonMachine*. Finally, as mentioned previously, in the context of our work the primary goal was to be able to compute as dose distribution coherent with the dose calculation performed by *ProtonMachine* in order to compare static and dynamic dose distributions in `MSPT`. Therefore, we consider the results as acceptable for our study.

4.3 Impact of motion

As previously mentioned, with `MSPT`, one can evaluate the robustness in regards to motion of a treatment plan by performing a first simulation for a static patient and a second simulation with a moving patient. To simulate the motion, we use the ideal breathing model described in Section 3.2.2. The motion amplitudes are 0.5, 1 and 1.5 cm for respectively, X, Y and Z axis. The respective motion periods are 5, 4 and 3 seconds. These values correspond to realistic amplitudes and periods of breathing motions Seco et al. [2009]. To show the impact of motion on the dose distribution we compare the dose distributions using the dosimetric parameters $D_{95\%}$ and $D_{50\%}$. We perform the experiment on the lung tumor case presented previously.

To present a concrete delivery example, we chose to model a synchrotron due a longer time delay for the energy transitions, even though the user could use a cyclotron model. We set different time and distance parameters based on data provided in the literature and in the treatment plan. The rotational speed of the gantry is set to 1 rotation per minute [Ding et al., 2007], the time to change the beam's energy is set to 2.1 s [Smith et al., 2009], the spill duration is set to 5 s [Kraus et al., 2011] and the lateral and vertical scanning speed are both set to 10 $m.s^{-1}$ [Kraus et al., 2011]. The number of protons per MU used in *ProtonMachine* is 1×10^9 protons per MU. The extraction rate was set to 7.3×10^{10} $protons.s^{-1}$. The time to move from one beam position to another is estimated as the maximum between the time for the lateral shift and for the vertical shift. The beam size used is read from the treatment plan and is equal to 5 mm. The distance between energy layers is approximately 3 mm at low energies and 7 mm at high energies.

To show the impact of the motion simulated in `MSPT`, we compared the resulting dose distributions of a treatment plan of a patient in a static and a moving situation. First, comparing the DVHs (see Figure 4.13), one can easily observe that the tumor coverage has been highly degraded due to the motion. This is validated by the dosimetric parameters (see Table 4.6) $D_{95\%}$ and $D_{50\%}$. Indeed, in the static patient, 95% of the tumor volume received 97% of the dose prescription (*i.e.*, 174.5 cGy) and 50% of the tumor volume received 102% of the prescription (*i.e.*, 184 cGy); whereas, in the moving patient 65% of the prescription (*i.e.*, 118.5 cGy) was delivered to 95% of the tumor and 89% (*i.e.*, 160.5 cGy) to 50% of the tumor.

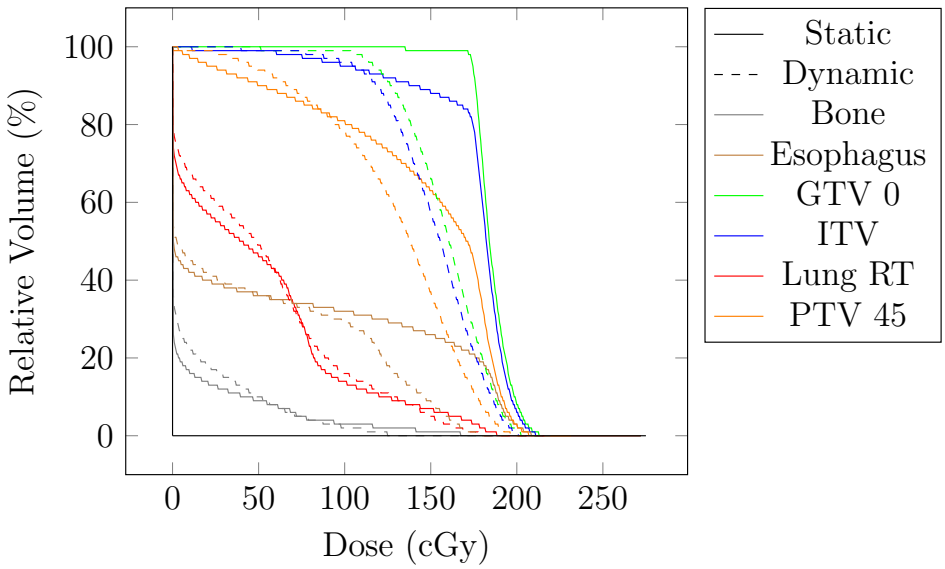

Figure 4.13 – Comparison of DVHs for a delivery on a static and dynamic patient.

	$D_{95\%}(cGy)$	$D_{50\%}(cGy)$
Static patient	174.5	184
Dynamic patient	118.5	160.5

Table 4.6 – Dose received by 95% and 50% of the tumor volume for the delivery of a treatment plan simulated, for a patient static and the same patient moving, in `MSPT`.

We visually compared dose distributions (see Figure 4.14), for transverse planes located near the middle and in the vicinity of a border of the tumor. First, we noted some dose heterogeneities in the target region (Figures 4.14a and 4.14b), which was validated by the cold spots present in Figure 4.15a corresponding to underdosed areas. Moreover, the comparison of Figures 4.14c and 4.14d exhibits a great difference in the delivery of the two target spots. As illustrated in Figure 4.15b the targets are missed (presence of cold spots) while other regions have been wrongly irradiated (hot and cold spots).

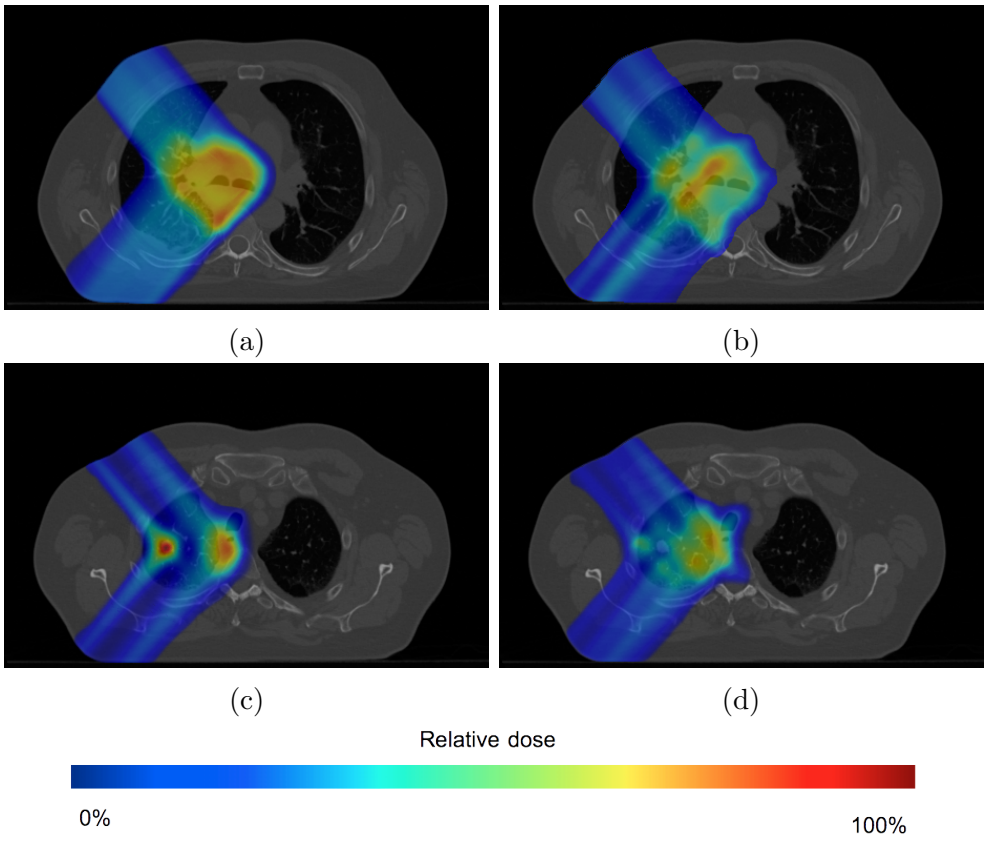

Figure 4.14 – Dose distributions computed overlaying a patient CT image (transverse planes), for a static (4.14a, 4.14c) and a moving patient (4.14b,4.14d). Slices 4.14a and 4.14b are located near the middle of the tumor and slices 4.14c and 4.14d are located near a border of the tumor.

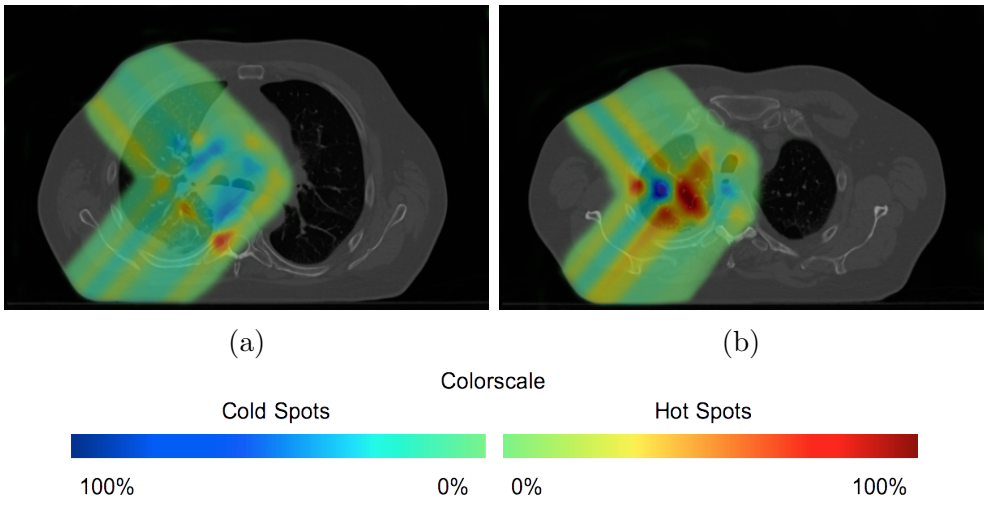

Figure 4.15 – Hot and cold spots present in the dose distribution of the moving patient overlaying the patient CT image (transverse planes). They correspond to the dose distributions in Figure 4.14. Slice 4.15a is located near the middle of the tumor and slice 4.15b is located at a border of the tumor.

The presence of cold spots in the tumor, the presence of hot spots in regions that were not supposed to be irradiated and the differences of 32% for the $D_{95\%}$ parameter and 13% for $D_{50\%}$ in the tumor indicate that the tumor is not properly targeted and healthy tissues are wrongly irradiated. Therefore, this treatment plan delivered to this dynamic patient did not achieve its goal: the tumor did not received enough dose and healthy tissues were not properly protected. These conclusions indicate that the plan used is not robust to the patient intra-fraction motions. One would have to consider another treatment plan or implement mitigation methods.

Chapter 5

Compensation technique

In order to improve the robustness to motion of the spot scanning technique we propose a new approach based on a beam weight compensation technique. This work on this mitigation strategy is preliminary study to show some interests and limitations of this approach.

Other mitigation strategies already exist. One of the most common techniques is the beam gating [Keall et al., 2006; Minohara et al., 2000], which consists of irradiating the patient only when the patient reaches a certain phase of the breathing motion (see Figure 5.2). Patient motions, such as breathing, can also be controlled through coaching [Hughes et al., 2008] by audio or visual feedback in order to limit the cycles variability. Motion can also be dealt with through breath-hold technique [Wong et al., 1999] or apnea and anesthesia [Eckermann et al., 2011]. These techniques are promising solutions but tend to be constraining for the patient since.

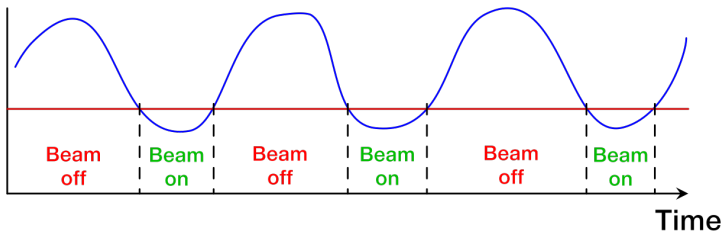

Figure 5.1 – Illustration of the beam gating delivery. Patient motions are represented in blue and threshold level for gating in green. The patient is being irradiated when the beam is "on" and the beam is "off" otherwise.

Other promising strategies more specific to the spot scanning techniques have been investigated: the repainting (also called re-scanning) [Zenklusen et al., 2010] and the beam tracking [Bert et al., 2012; Saito and Bert, 2012]. The repainting technique consists of delivering the planned dose into several cycles instead of a single pass. The goal is to obtain a high scanning speed by reducing the time spent at each spot position and reduce the risk of large localized dose discrepancies. While this technique is encouraging it does not take into account the patient motions during the delivery. The beam tracking method (see Figure 5.2) calculates the target displacement and uses this information

to adapt the beam position (lateral compensation: scanning magnets adapt the beam position) and beam energy (longitudinal compensation: adaptation of the thickness of material encountered by the beam to move the Bragg peak position) to aim the planned target point in the patient. This method is particularly promising, however, it requires the compensation both for the position and the energy. That is why we wanted to develop and study a technique that only adapts the beam's weights, that take into account the patient intra-fraction motion and that can be delivered without constraining the patient.

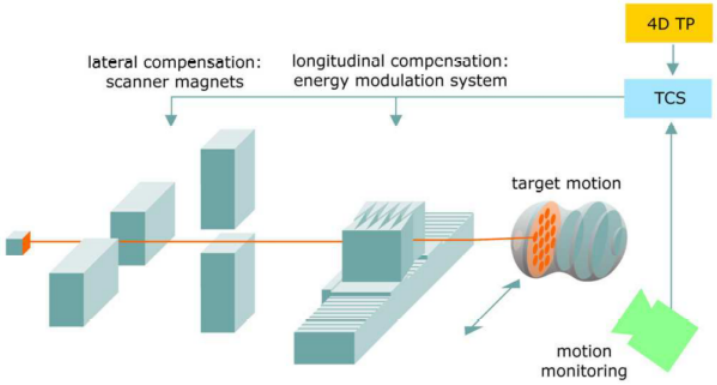

Figure 5.2 – Illustration of the beam tracking system. [Saito and Bert, 2012]. The motion monitoring system measures the patient displacement, the 4D treatment planning (4D TP) calculates the target displacement and the therapy control system (TCS) controls the compensation (*i.e.*, beam position and energy).

5.1 Principle of the compensation technique

The overall principle of our compensation strategy is to adapt the pencil beam's weight to the point in the patient targeted by the beam. The weight to be used is obtained from the patient displacement vector and the weight of the beam position that was originally planned for the irradiation of this target point.

More formally, let us consider an treatment plan, for which the beam positions for the beam energy E_n are represented by the points (b_i, w_i), where i indicates the beam index, b_i the beam position and w_i the corresponding planned weight. This plan induces the irradiation of respective (P_i), the target points of the energy layer associated to E_n in a static patient (see Figure 5.3) located at the depth of the Bragg peak. (P_i) is irradiated by the beam $(t = i, w = w_i)$ where t is the date and w the weight of the beam.

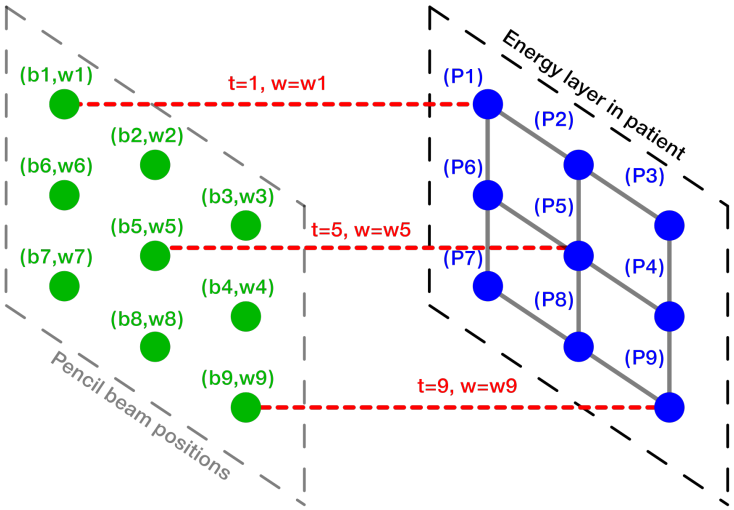

Figure 5.3 – Illustration of the delivery for a static patient. Beam positions are represented in green. Beams are represented in red. Target points in the patient are represented in blue.

One can now consider the same treatment plan delivered to a moving patient. The motion is considered in $2D$, in the plan orthogonal to the beam direction, as a displacement vector $v(t)$. As an example, at date $t = 2$, the beam will be at position b_2 and will deliver a weight w_2. However, because of $v(t)$ at $t = 2$, another target point than P_2 can be irradiated, *e.g.*, P_5, which would receive an irradiation corresponding to w_2 instead of w_5 (see Figure 5.4).

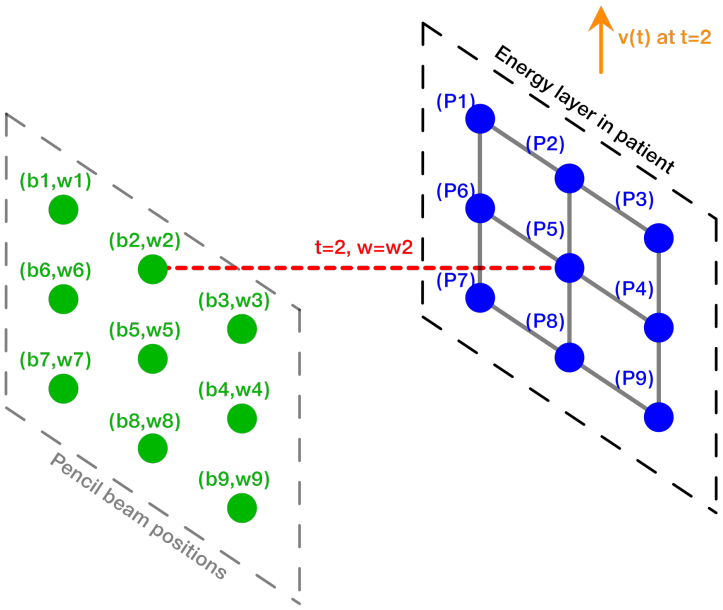

Figure 5.4 – Illustration of the delivery for a moving patient without the compensation technique. Beam positions are represented in green. Beams are represented in red. Target points in the patient are represented in blue. The 2D displacement vector is represented in orange.

Let us consider $v(t)$ being expressed as $v(t) = \begin{pmatrix} v_H(t) \\ v_V(t) \end{pmatrix}$, where $v_H(t)$ and $v_V(t)$ are respectively the horizontal and vertical components of $v(t)$. As previously explained in the example, at date $t = 2$, the beam is positioned at b_2 and targets P_5. The compensation technique relies on the adaptation of the beam weight w, which is set to w_5 instead of w_2 (see Figure 5.5).

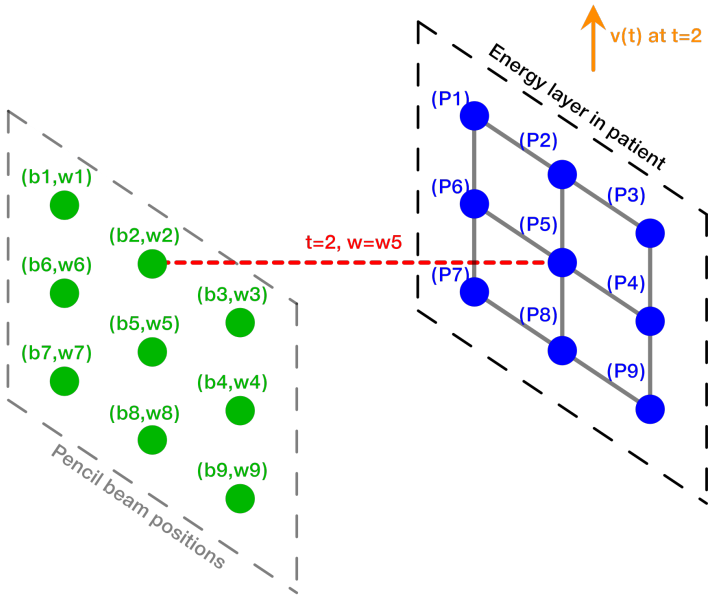

Figure 5.5 – Illustration of the delivery for a moving patient with the compensation technique. Beam positions are represented in green. Beams are represented in red. Target points in the patient are represented in blue. The 2D displacement vector is represented in orange.

For a given beam energy, E_n, we say that the beam position $b_i = \begin{pmatrix} b_{i_H} \\ b_{i_V} \end{pmatrix}$, where b_{i_H} and b_{i_V} are respectively the horizontal and vertical components of the beam position, can be compensated at the date t, if for a given displacement $v(t) = \begin{pmatrix} v_H(t) \\ v_V(t) \end{pmatrix}$ of the patient body, there exists $b_k = \begin{pmatrix} b_{k_H} \\ b_{k_V} \end{pmatrix}$, with $w_k > 0$, in the neighborhood of the positions $\begin{pmatrix} b_{i_H} - v_H(t) \\ b_{i_V} - v_V(t) \end{pmatrix}$ belonging to the beam positions planned for E_n. Hence, if b_i can be compensated at t, the beam's weight is set to w_k. The neighborhood, is defined by the rectangle centered at $\begin{pmatrix} b_{i_H} - v_H(t) \\ b_{i_V} - v_V(t) \end{pmatrix}$ of length Δ_H and width Δ_V, where Δ_H and Δ_V are respectively the minimum horizontal and vertical distances (> 0) between two consecutive beam positions.

5.2 Strategy of the compensation technique

5.2.1 Strategy presentation

The strategy used for the compensation of 2D motions orthogonal to the beam's directions relies on the non-volumetric re-scanning principle. For each energy level, the pencil beam moves at the positions in order. Once the beam is set at a position b_i, if it can be compensated (see previous section) the weight is adapted and the entire planned weight

w_k is delivered (*i.e.*, w_k is not divided as in the conventional re-scanning technique), and w_k will not be used for another future position. If the position cannot be compensated, the beam moves to the next position. When all the positions have been scanned once, the beam re-scans all the positions to deliver the weights that have not been used to irradiate the targets. The number of re-scans is not limited. However, if one needs to prevent from a high number of re-scans, it is possible to add a *margin* around the planned positions (see Figure 5.6).

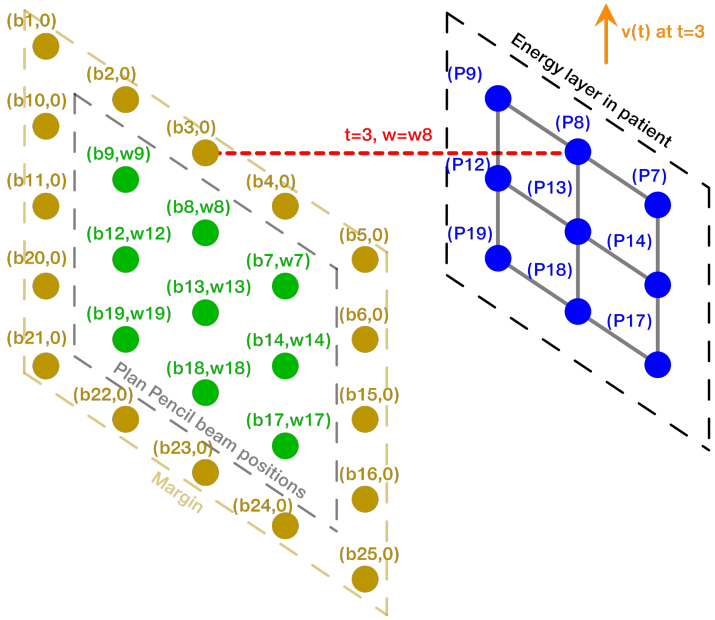

Figure 5.6 – Illustration of the delivery for a moving patient with the compensation technique where a margin is added around the planned positions. Beam positions are represented in green. Beams are represented in red. Target points in the patient are represented in blue. The 2D displacement vector is represented in orange.

To generate the margin we represent the initial spot positions of an energy layer in a 2D array as a binary image: 1 at the spot positions and 0 otherwise. We apply the dilation, a morphological operator, to this binary image to extend the region covered by the initial positions. The structuring element used for the dilation is a single pixel of the considered image. The dilation is repeated a number of times corresponding to the number of iterations needed to achieve the margin thickness parameter provided in the configuration file. To each pixel of the 2D representation, in the margin area, is associated a beam position, of weight $w = 0$, defined based on Δ_H and Δ_V previously introduced, which corresponds to the dimensions of a pixel. Figure 5.7 presents an example of the 2D representation of the initial beam positions and the margin.

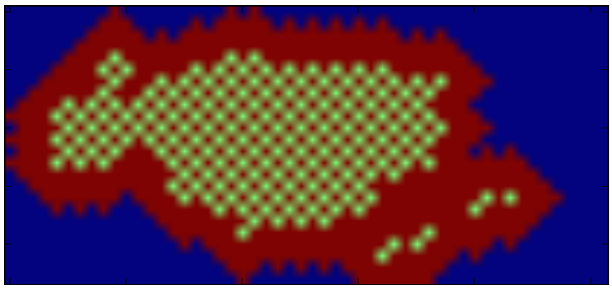

Figure 5.7 – Example of a 2D representation of the beam positions (in green), the margin region (in red) and the region where no beam position is defined (in blue) for a single energy layer.

The spot positions are updated at the end of each scan in order to keep only the initial beam positions whose weight has not been used for the irradiation. The margin is then recomputed.

The user can control the margin in the `MSPT` configuration file.

5.2.2 Compensation algorithm

In this section we will present the compensation algorithm. We will keep the notations introduced in Section 5.1. Variables used in Algorithm 2 correspond to variables defined in Algorithm 1. Algorithm 1 represents the overall process of the compensated delivery. The process of the function used to determine whether the compensation can be applied for a beam position is presented in Algorithm 2.

Algorithm 1: Algorithm of the compensated delivery. TP is the treatment plan provided by the user.

```
1  begin
2      foreach Gantry angle in TP do
3          foreach Energy level in TP do
4              Build l_pos the list of all the beam positions;
               // Note: if margin is used, include in l_pos the margin beam positions
                  with weight = 0 if margin is used.
5              Build l_plan the list of all the beam positions (weights > 0);
6              while l_plan is not empty do
7                  foreach Beam position b_i in l_pos do
8                      Set the beam position to b_i;
9                      Get the patient displacement vector v(t);
                       // Obtained from the motion monitoring system.
10                     if Compensation is possible then
                           // Compensation is possible: See Algorithm 2.
11                         Get the beam's weight w_k;
12                         Irradiate the target (b_i, w_k);
13                         Update l_plan: remove w_k from b_k;
                           // w_k being the weight associated to b_k in TP
14                     else
15                         do nothing;
16     return;
```

Algorithm 2: Algorithm to test whether the compensation is possible.

```
1  begin
2      foreach Beam position b_j in l_plan do
3          (dist_H,dist_V) ← Euclidean distance (b_j , b_i − v(t));
           // Calculate independently horizontal and vertical distances: resp.
              dist_H and dist_V .
4          if dist_H < Δ_H and dist_V < Δ_V then
               // i.e., b_j is in the rectangle centered on b_i − v(t) of length Δ_H and
                  width Δ_V
5              b_k ← b_j;
6              w_k ← w_j;
7              return True;
8          else
9              do nothing;
10     return False;
```

5.3 Evaluation of the compensation

To evaluate the compensation method we perform simulations on the SBRT lung tumor case presented in Section 4.2.2 and using the `MSPT` settings presented in Section 4.3. The simulations settings are summarized in Table 5.1. Dose distributions comparisons is based on the DVHs and the dosimetric parameters, which are often used to assess the quality of a treatment plan: the dose delivered to 95% ($D_{95\%}$) and 5% ($D_{5\%}$) of the tumor volume and the normalized volume of different body tissues receiving a given percentage of the prescribed dose: 10% (V_{10}), 33%(V_{33}), 50%(V_{50}), 66%(V_{66}) and 90%(V_{90}). We also compare the mean dose received by these tissues (D_{mean}). The body tissues considered are the OARs: *right lung* and *spinal cord*. Figure 5.8 locates the different volumes. Finally, to evaluate the quality of the compensation in Sections 5.3.1 and 5.3.1 we also refer to the clinical criterion used to ensure that a treatment plan achieves the desired tumor coverage: 95% of the tumor volume received 95% of the prescribed dose R_x ($D_{95\%} \geq 95\%$ R_x). For this treatment $R_x = 1.5$ cGy. In our situation the dose distribution used as a reference is the static delivery simulated in `MSPT`. Therefore,in order to consider that this dose distribution meets the plan requirement, $D_{95\%} \geq 95\%$ R_x, we will assume that the dose prescription is the $D_{95\%}$ value of this static dose distribution.

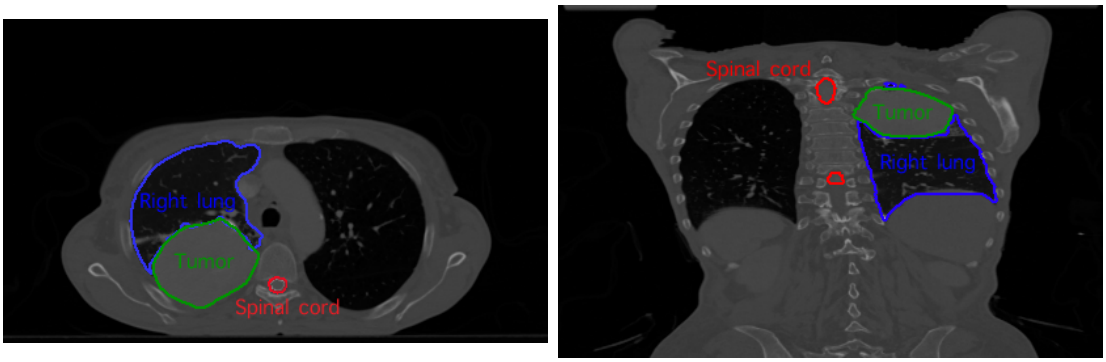

(a) (b)

Figure 5.8 – Delineation of the tumor and the OARs overlaying a patient CT image (left: transverse plane, right: coronal plane): in green the tumor, in red the spinal cord and in blue the right lung.

The motions are simulated with the irregular motion model with ϕ_x, ϕ_y, ϕ_z set to zero. Other motion parameters are presented in Table 5.1. We consider motions of moderate amplitude (*i.e.*, 0.5 cm) and of large amplitude (*i.e.*, 1.5 cm). The standard deviation of the Gaussian distribution applied to the variability of amplitude and the period is set to 20% of the amplitude or the period [Heath et al., 2009].

To highlight interests and limitations of the compensation strategy we study different motion amplitudes, we consider the use of a margin and finally we show the impact of the motion monitoring system accuracy.

Test index	Intra-fraction motion	Motion				Compen-sation	Motion monitoring $[\sigma_{\delta x}, \sigma_{\delta y}, \sigma_{\delta z}]$ in cm	Hiccup or Cough
		Amplitude $[b_x, b_y, b_z]$ in cm	Amplitude $[\sigma_{bx}, \sigma_{by}, \sigma_{bz}]$ in cm	Period $[\tau_x, \tau_y, \tau_z]$ in s	Period $[\sigma_{\tau x}, \sigma_{\tau y}, \sigma_{\tau y}]$ in s			
1	No	-	-	-	-	-	-	-
2	Yes	[0.5, 0.5, 0]	[0.1, 0.1, 0]	[4, 4, 0]	[0.8, 0.8, 0]	No	-	No
3	Yes	[1.5, 1.5, 0]	[0.3, 0.3, 0]	[4, 4, 0]	[0.8, 0.8, 0]	No	-	No
4	Yes	[0.5, 0.5, 0]	[0.1, 0.1, 0]	[4, 4, 0]	[0.8, 0.8, 0]	Yes	[0, 0, 0]	No
5	Yes	[1.5, 1.5, 0]	[0.3, 0.3, 0]	[4, 4, 0]	[0.8, 0.8, 0]	Yes	[0, 0, 0]	No
6	Yes	[1.5, 1.5, 0]	[0.3, 0.3, 0]	[4, 4, 0]	[0.8, 0.8, 0]	Yes	[0.3, 0.3, 0]	No
7	Yes	[1.5, 1.5, 0]	[0.3, 0.3, 0]	[4, 4, 0]	[0.8, 0.8, 0]	Yes	[0.75, 0.75, 0]	No
8	Yes	[1.5, 1.5, 0]	[0.3, 0.3, 0]	[4, 4, 0]	[0.8, 0.8, 0]	Yes	[1.5, 1.5, 0]	No

Table 5.1 – Table summarizing the tests performed to evaluate the compensation method. Note : '-' means that it doesn't apply to the corresponding test.

5.3.1 Evaluation of the compensation for moderate amplitude motions

In this section we evaluate the compensation strategy for a moderate motion amplitude (*i.e.*, 1.5 cm) using Tests 1, 2 and 4 (see Table 5.1). Figures 5.9 and 5.10 show the resulting dose distributions of the three experiments in transverse (parallel to the beam) and coronal planes (parallel to the motion plane and orthogonal to the beam) obtained near the center of the tumor. Figure 5.11 presents the resulting DVHs of the dose distributions for the three experiments. Tables 5.2 and 5.3 summarize the dosimetric parameters considered for the comparison.

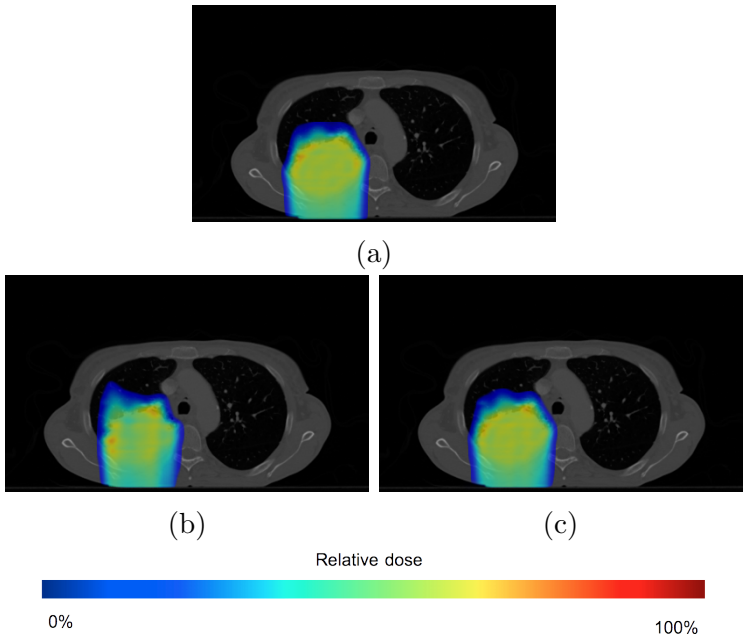

Figure 5.9 – Dose distributions computed overlaying a patient CT image (transverse planes), for a static (5.9a) and a moving patient without (5.9b) and with (5.9c) compensation.

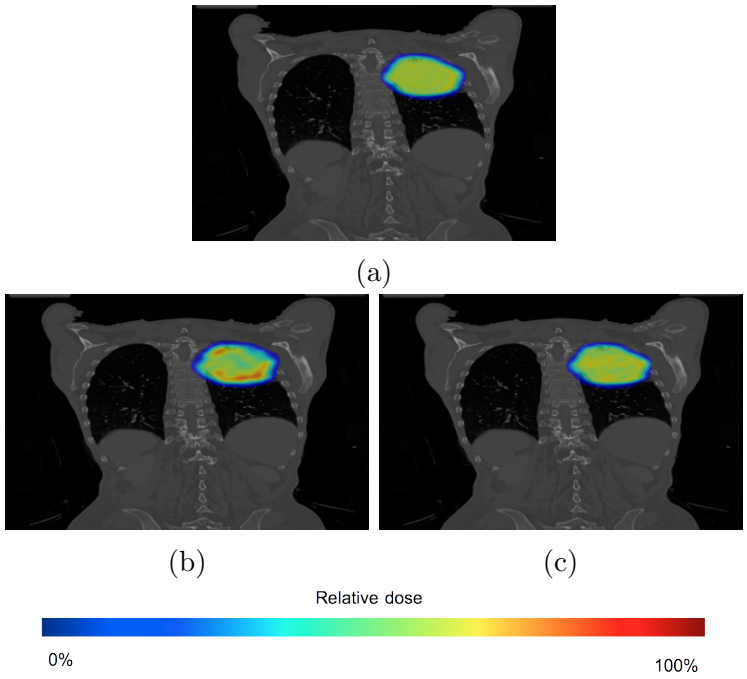

Figure 5.10 – Dose distributions computed overlaying a patient CT image (coronal planes), for a static (5.10a) and a moving patient without (5.10b) and with (5.10c) compensation.

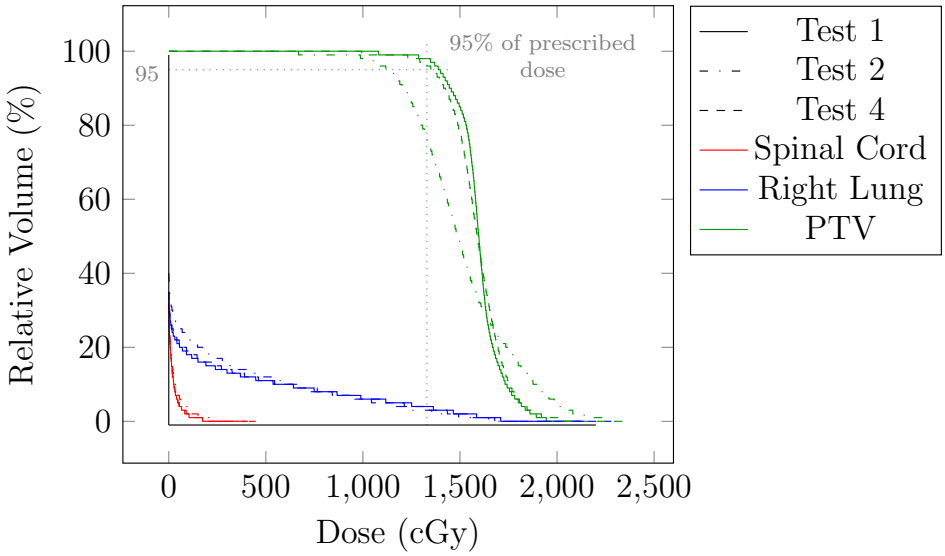

Figure 5.11 – Comparison of DVHs for a delivery on a static (Test 1) and dynamic patient with (Test 4) and without (Test 2) compensation for a 0.5 cm motion amplitude.

Test index	$D_{95\%}$ (cGy)	$D_{5\%}$ (cGy)
1	1399.5	1816
2	1141	2009.5
4	1367.5	1824.5

Table 5.2 – Dose received by 95% and 5% of the PTV on a static (Test 1) and dynamic patient with (Test 4) and without (Test 2) compensation for a 0.5 cm motion amplitude.

Tissue	Test index	$V_{10}(\%)$	$V_{33}(\%)$	$V_{50}(\%)$	$V_{66}(\%)$	$V_{90}(\%)$	$D_{mean\%}$(cGy)
Right Lung	1	17	11	8	6	4	158.33
	2	20	12	9	6	3	172.15
	4	17	11	8	6	3	159.31
Spinal Cord	1	1	0	0	0	0	9.28
	2	2	0	0	0	0	12.24
	4	1	0	0	0	0	9.81

Table 5.3 – Volume receiving 10, 33, 50, 66 and 90 % of the prescribed dose and the average dose received by the OARs in `MSPT` on a static (Test 1) and dynamic patient with (Test 4) and without (Test 2) compensation for a 0.5 cm motion amplitude.

Visually, from Figures 5.9 and 5.10, we can observe that the dose distributions of the static and the compensated delivery are close, whereas heterogeneities are visible in the tumor in the case of the non-compensated delivery. The observation of the DVHs and the dosimetric parameters show the similar results. Indeed, based on the DVHs, the tumor coverage is degraded without the compensation, whereas it stays close to the expected one with the compensation. The difference of $D_{95\%}$ and $D_{5\%}$ measurements are respectively 2.3% and 0.5% for the compensated delivery, and 18.5% and 10.7% without the strategy. Moreover, considering other body tissues, the average differences of relative volume between the static and compensated delivery were: 0%, 0%, 0%, 0% and 0.5%, respectively for $V_{10}(\%)$, $V_{33}(\%)$, $V_{50}(\%)$, $V_{66}(\%)$, $V_{90}(\%)$. The average difference of dose received by 50% of these tissues ($D_{50\%}$) is 0%. The differences between the static and non-compensated deliveries were: 2%, 0.5%, 0.5%, 0%, 0.5%, and 4.2% respectively for $V_{10}(\%)$, $V_{33}(\%)$, $V_{50}(\%)$, $V_{66}(\%)$, $V_{90}(\%)$ and $D_{50\%}$. The differences between the static and the compensated deliveries can be explained by the parameters Δ_H and Δ_V, defined in the compensation strategy. Indeed, these parameters allow small shifts from the planned beam position and can induce dosimetric errors similar to errors introduced by motions. Keeping Δ_H and Δ_V small enough (in the order of the distance between two consecutive spots) reduces greatly the errors. As explained in the introduction of Section 5.3, we consider prescribed dose being the $D_{95\%}$ value of the static dose distribution. Therefore, $R_x = 1399.5$. In order to be acceptable a dose distribution should achieve the criterion:$D_{95\%} \geq 95\%\ R_x$. From Table 5.2, we can claim that the compensated delivery, unlike the non compensated delivery, achieved this criterion.

Overall, the compensation improved significantly the dose distribution since the error to the static delivery for the $D_{95\%}$ parameter dropped from 18.5% to 2.3% of the dose

distribution. Moreover, the average difference of dose received by the OARs decreased from 4.2% to 0%. Therefore, this mitigation technique allows a better coverage of the tumor and a better sparing of OARs. Finally, the compensated delivery met the $D_{95\%} \geq 95\%$ R_x requirement to be clinically acceptable.

5.3.2 Evaluation of the compensation for large amplitude motions

In this section we evaluate the compensation strategy for a large motion amplitude (*i.e.*, 1.5 cm) using Tests 1, 3 and 5 (see Table 5.1). Figures 5.12 and 5.13 show the resulting dose distributions of the three experiments respectively in a transverse plane and in a coronal plane obtained near the center of the tumor. Figure 5.20 presents the resulting DVHs of the dose distributions for the three experiments. Tables 5.4 and 5.5 summarize the dosimetric parameters considered for the comparison.

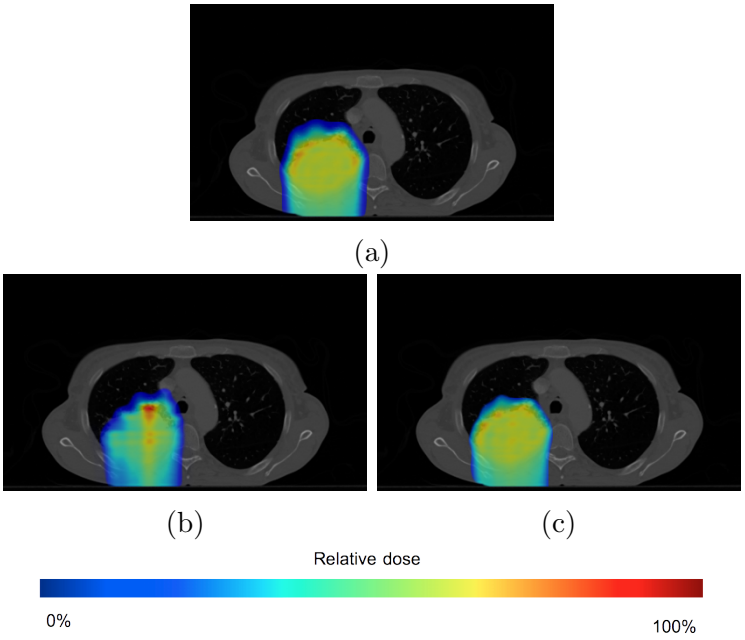

Figure 5.12 – Dose distributions computed overlaying a patient CT image (transverse planes), for a static (5.12a) and a moving patient without (5.12b) and with (5.12c) compensation.

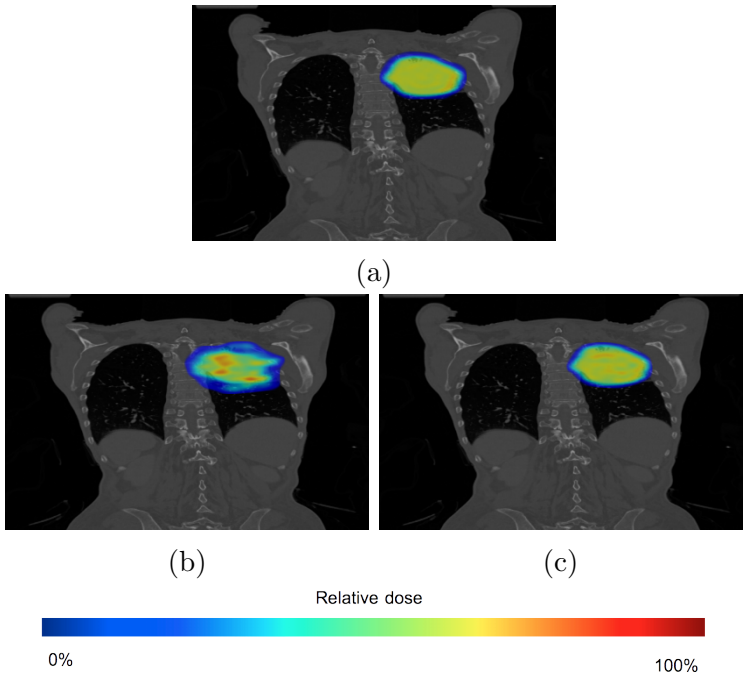

Figure 5.13 – Dose distributions computed overlaying a patient CT image (coronal planes), for a static (5.13a) and a moving patient without (5.13b) and with (5.13c) compensation.

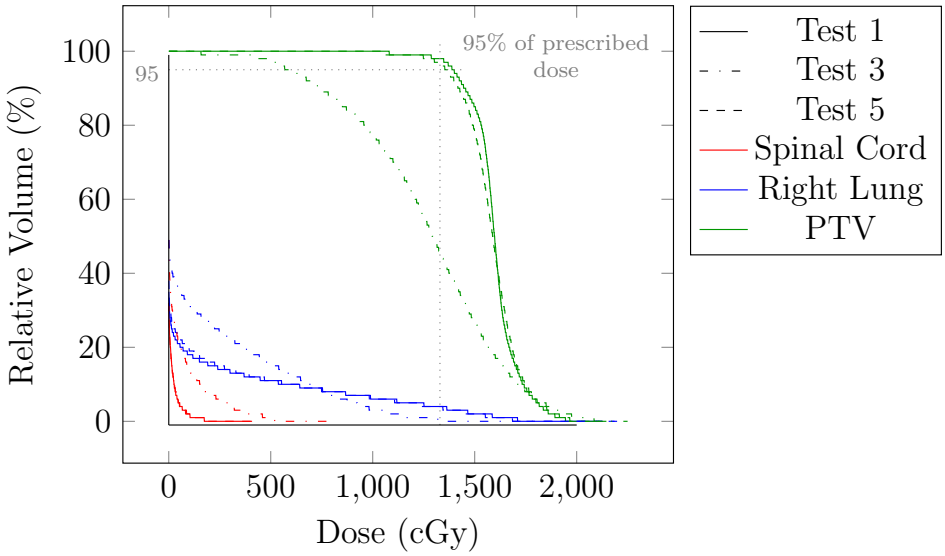

Figure 5.14 – Comparison of DVHs for a delivery on a static (Test 1) and dynamic patient with (Test 5) and without (Test 3) compensation for a 1.5cm motion amplitude.

Test index	$D_{95\%}$ (cGy)	$D_{5\%}$ (cGy)
1	1399.5	1816
3	600	1849.5
5	1367.5	1823.5

Table 5.4 – Dose received by 95% and 5% of the PTV on a static (Test 1) and dynamic patient with (Test 5) and without (Test 3) compensation for a 1.5 cm motion amplitude.

Tissue	Test index	$V_{10}(\%)$	$V_{33}(\%)$	$V_{50}(\%)$	$V_{66}(\%)$	$V_{90}(\%)$	$D_{mean\%}$(cGy)
Right Lung	1	17	11	8	6	4	158.33
	2	29	16	9	3	0	193.87
	5	18	11	9	6	3	161.43
Spinal Cord	1	1	0	0	0	0	9.28
	3	11	1	0	0	0	44.49
	5	1	0	0	0	0	9.69

Table 5.5 – Volume receiving 10, 33, 50, 66 and 90 % of the prescribed dose and the average dose received by the OARs in `MSPT` on a static (Test 1) and dynamic patient with (Test 5) and without (Test 3) compensation for a 1.5 cm motion amplitude.

Visually, from Figures 5.12 and 5.13, we can observe important heterogeneities in the dose distribution without the compensation strategy and notice that the tumor is not properly covered. On the contrary, the dose distribution using the mitigation technique provides a better tumor coverage and appears to be closer to the expected dose distribution of the static case. The DVHs and the dosimetric parameters confirm this visual observation. Indeed, based on the DVHs, the tumor coverage is highly degraded without the compensation, whereas it is close to the expected coverage with the compensation: the use of the compensation decreases $D_{95\%}$ error from 57% to 2.29% and the $D_{5\%}$ error from 1.8% to 0.41%, which indicates an significant improvement of the tumor coverage, especially when considering the $D_{95\%}$ parameter. Moreover, considering other body tissues, the average differences of relative volume between the static and compensated delivery were: 0.5%, 0%, 0.5%, 0% and 0.5%, respectively for $V_{10}(\%)$, $V_{33}(\%)$, $V_{50}(\%)$, $V_{66}(\%)$ and $V_{90}(\%)$. The average difference of dose received by 50% of these tissues ($D_{50\%}$) is 2.42%. The differences between the static and non-compensated deliveries were: 11%, 3%, 0.5%, 1.5%, 2%, and 30.40% respectively for $V_{10}(\%)$, $V_{33}(\%)$, $V_{50}(\%)$, $V_{66}(\%)$, $V_{90}(\%)$ and $D_{50\%}$. This shows that the compensation strategy helps preserve the OARs since the average error of the dose received decreases from 30.40% to 2.42%. As explained in the previous section, the differences between the static and the compensated deliveries can be explained by the parameters Δ_H and Δ_V. In addition, these parameters constraining the distance between the beam position (b_i in Algorithm 1) and the position being compensated (b_k in Algorithm 1) limit the dosimetric errors, which can explain why the doses received by 95% of the tumor in the compensated delivery for the moderate (Test 4) and the large (Test 5) motion are the same. From Table 5.4, we can claim that the compensated delivery, unlike the non compensated delivery, achieved the criterion $D_{95\%}$

$\geq 95\%$ R_x.

The delivery without the compensation strategy presents important differences in the dose distribution. As for the delivery applying the strategy, the errors are smaller than 5%. In addition, it achieved the tumor coverage criterion. Therefore, the compensated dose distribution can be considered as clinically acceptable. We can say that based on the results the compensation strategy mitigate greatly the impact of motion and improves the robustness of the treatment plan.

5.3.3 Compensation with and without margin

In this section, we study the use of margins for the beam positions in the compensation strategy by repeating Test 5 (see Table 5.1) with and without margin. The margin thickness was set to one half of the motion amplitude.

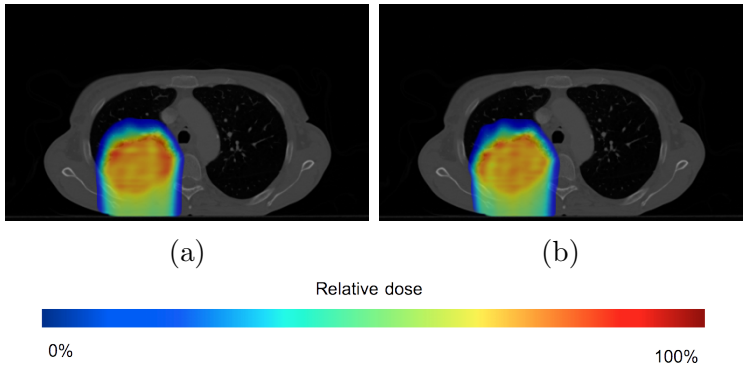

Figure 5.15 – Dose distributions computed overlaying a patient CT image (transverse planes), for a moving patient using the compensation strategy with (5.16a) and without (5.16b) margin.

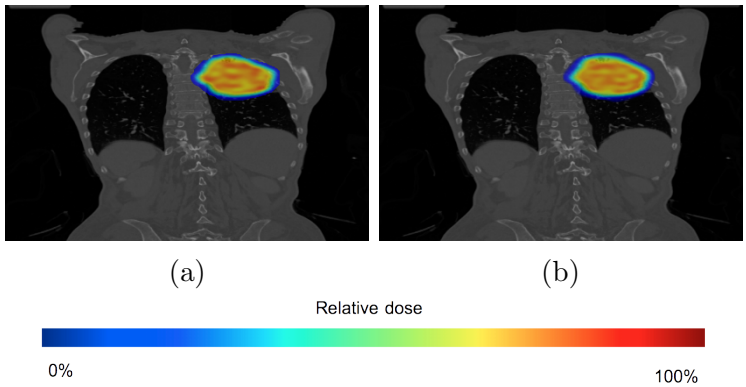

Figure 5.16 – Dose distributions computed overlaying a patient CT image (coronal planes), for a moving patient using the compensation strategy with (5.16a) and without (5.16b) margin.

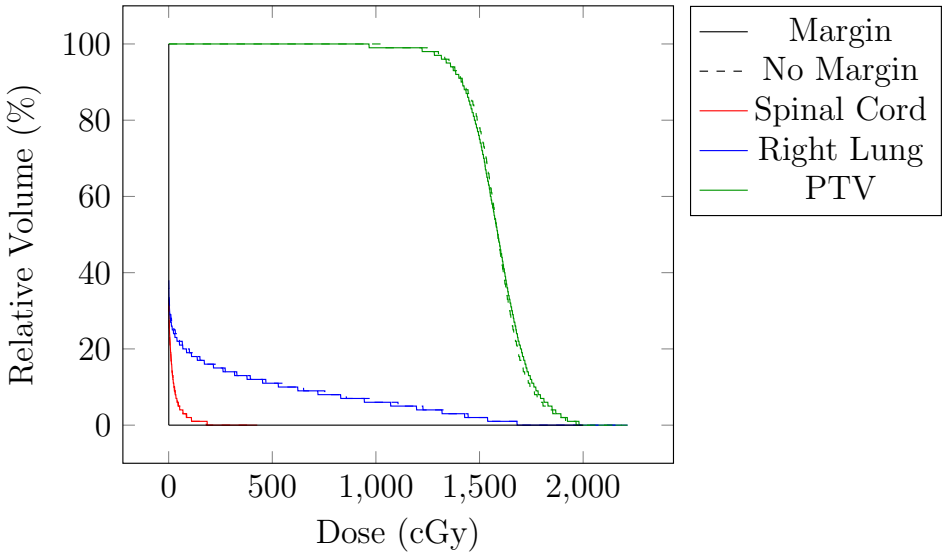

Figure 5.17 – Comparison of DVHs for a compensated delivery on a dynamic patient for a 1.5 cm motion amplitude with and without margin.

Test	$D_{95\%}$ (cGy)	$D_{5\%}$ (cGy)
Margin	1359.5	1849.5
No Margin	1367.5	1823.5

Table 5.6 – Dose received by 95% and 5% of the PTV on a dynamic patient for a delivery using the compensation strategy with and without margin for a 1.5 cm motion amplitude.

Tissue	Test	$V_{10}(\%)$	$V_{33}(\%)$	$V_{50}(\%)$	$V_{66}(\%)$	$V_{90}(\%)$	D_{mean}(cGy)
Right Lung	Margin	17	11	8	6	3	157.00
	No Margin	18	11	9	6	3	161.43
Spinal Cord	Margin	1	0	0	0	0	9.65
	No Margin	1	0	0	0	0	9.69

Table 5.7 – Volume receiving 10, 33, 50, 66 and 90 % of the prescribed dose and the average dose received by the OARs in `MSPT` on a dynamic patient for a delivery using the compensation strategy with and without margin for a 1.5 cm motion amplitude.

Visually, from Figures 5.15 and 5.16, the dose distributions appear to be similar even though we can observe small heterogeneity differences. Based on the DVHs both dose distribution are in agreement. The comparison of the dosimetric parameters shows that the tumor coverage is equivalent: the differences are 0.6% and 1.4% for the $D_{95\%}$ and the $D_{5\%}$ parameters (see Table 5.6). In other tissues (see Table 5.7), the average absolute differences for the dosimetric parameters V_{10}, V_{33}, V_{50}, V_{66}, V_{90} are respectively 0.5%, 0%, 0.5%, 0% and 0%. The difference of mean dose received by these tissues is 2.3%. These low differences show that both deliveries provide an equivalent dose distribution.

	Mean	Stdev	Min	Max	Median
Margin	7.4	2.9	2	13	7
No Margin	202	905	33	3299	565

Table 5.8 – Re-scanning statistics for a delivery using compensation with and without margin.

Even though, the dose distributions are equivalent, we also compared the delivery process in both cases (see Table 5.8). The treatment plan delivered 19 energy layers, comprised between 39 and 118 MeV, representing 3839 beam positions. The minimum, maximum, median and average number of beam position for this entire treatment plan were respectively 2, 373, 221 and 202 over all the energy layers. Considering the results in Table 5.8, the use of margins reduced significantly the number of re-scanning: from 202 to 7.4 in average. In addition, the number of re-scanning varies less than without the margin: the standard deviation decreases from 905 to 2.9. However, the improvement in the number of re-scanning induces a higher number of beam position changes: 89771 with a margin instead of 85618. Therefore, this strategy, if applied, would be more interesting if the cost of energy transition is high and must be avoided such as in the case of volumetric repainting using a synchrotron. In addition, parameters Δ_H and Δ_V have also an impact on both the number of re-scannings and the number of beam position changes. Reducing the value of Δ_H and Δ_V (respectively increasing their value) would reduce (respectively increase) the likelihood of possible compensations (*i.e.*, If statement being True in Algorithm 1), which would induce more (respectively less) re-scannings and beam position changes in order to deliver the planned dose.

5.3.4 Evaluate the impact of the monitoring system accuracy

In this section we compare Tests 5 ($\sigma_\delta = 0$ cm), 6 ($\sigma_\delta = 0.3$ cm), 7 ($\sigma_\delta = 0.75$ cm) and 8 ($\sigma_\delta = 1.5$ cm) - see Table 5.1 - to show the impact of the modeled accuracy of the motion monitoring system.

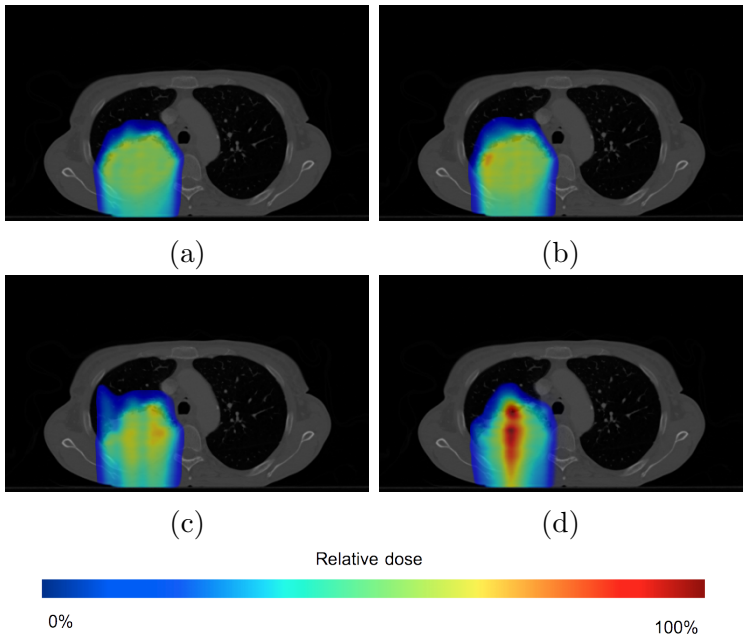

Figure 5.18 – Dose distributions computed overlaying a patient CT image (transverse planes), for a moving patient with compensation for different monitoring accuracy: $\sigma_\delta = 0$ cm (5.18a), 0.3 cm (5.18b), 0.75 cm (5.18c), 1.5 cm (5.18d).

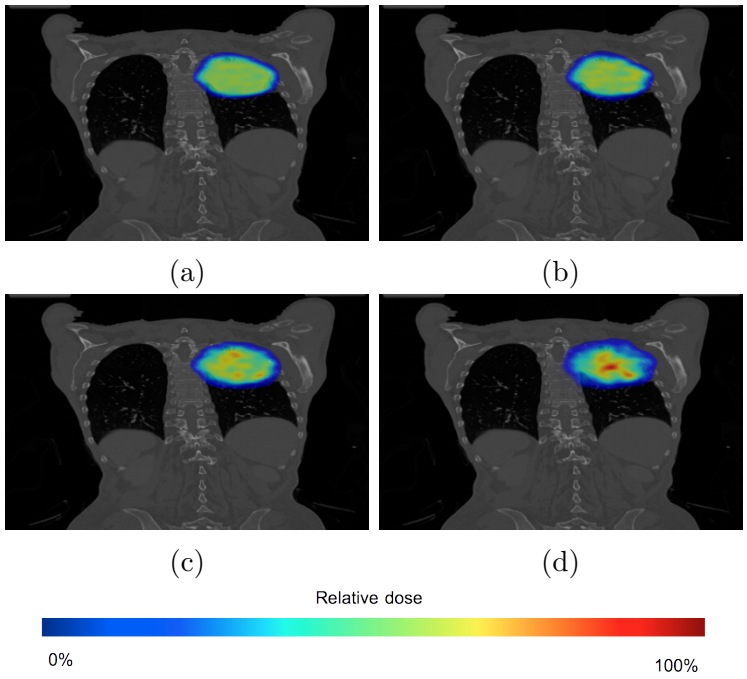

Figure 5.19 – Dose distributions computed overlaying a patient CT image (coronal planes), for a moving patient with compensation for different monitoring accuracy: $\sigma_\delta = 0$ cm (5.19a), 0.3 cm (5.19b), 0.75 cm (5.19c), 1.5 cm (5.19d).

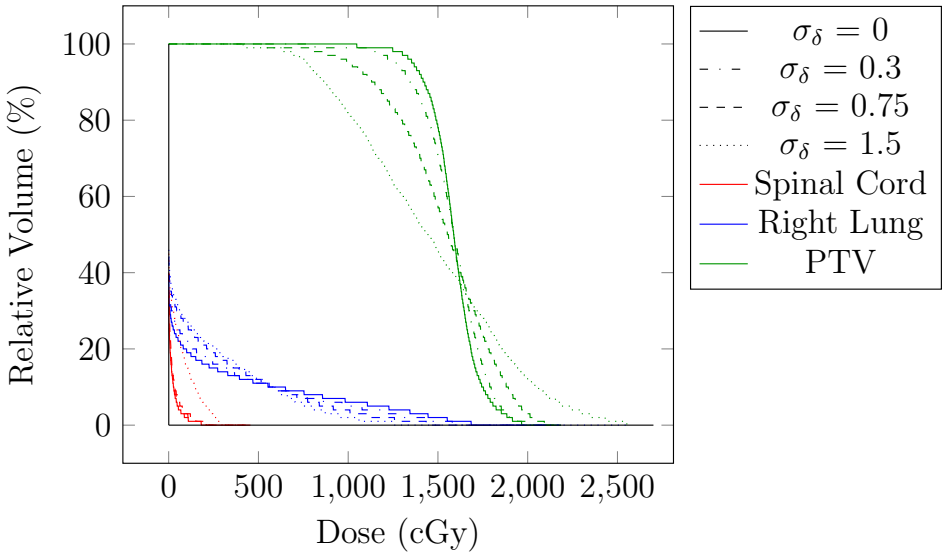

Figure 5.20 – Comparison of DVHs for a delivery on a dynamic patient with compensation for a 1.5 cm motion amplitude to evaluate the impact of the motion monitoring system accuracy.

σ_δ cm	$D_{95\%}$ (cGy)	$D_{5\%}$ (cGy)
0	1367.5	1823.5
0.3	1277	1852.5
0.75	1022.5	1966
1.5	779.5	2235.5

Table 5.9 – Dose received by 95% and 5% of the PTV on a dynamic patient for a delivery using the compensation strategy for different accuracy of the motion monitoring system.

Tissue	σ_δ cm	$V_{10}(\%)$	$V_{33}(\%)$	$V_{50}(\%)$	$V_{66}(\%)$	$V_{90}(\%)$	D_{mean}(cGy)
Right Lung	0	18	11	9	6	3	161.43
	0.3	20	11	8	5	2	157.62
	0.75	23	12	7	4	1	161.78
	1.5	25	12	6	2	0	157.51
Spinal Cord	0	1	0	0	0	0	9.69
	0.3	1	0	0	0	0	11.21
	0.75	1	0	0	0	0	12.96
	1.5	10	0	0	0	0	37.58

Table 5.10 – Volume receiving 10, 33, 50, 66 and 90 % of the prescribed dose and the average dose received by the OARs in `MSPT` on a dynamic patient with compensation for different accuracy of the motion monitoring system.

σ_δ cm	Difference $D_{95\%}(\%)$	Difference $D_{5\%}(\%)$
0.3	6.6	1.6
0.75	25.2	7.8
1.5	43.0	22.6

Table 5.11 – Table summarizing the average dosimetric differences, for the tumor, for different values of σ_δ, and where the delivery with $\sigma_\delta = 0$ cm is considered as the benchmark.

σ_δ cm	Difference $V_{10}(\%)$	Difference $V_{33}(\%)$	Difference $V_{50}(\%)$	Difference $V_{66}(\%)$	Difference $V_{90}(\%)$	Difference $D_{50\%}(\%)$
0.3	1.0	0	0.5	0.5	0.5	3.2
0.75	2.5	0.5	1.0	1.0	1.0	12.0
1.5	8.0	0.5	1.5	2	1.5	19.2

Table 5.12 – Table summarizing the average dosimetric differences, for the OARs, for different values of σ_δ, and where the delivery with $\sigma_\delta = 0$ mm is considered as the benchmark.

Visually, from Figures 5.18 and 5.19, we can see that the accuracy of the monitoring system has an impact of the quality of the final dose distribution. If we consider the dose distribution obtained at $\sigma_\delta = 0$ cm as a reference, we can observe that the dose distribution obtained with $\sigma_\delta = 0.3$ cm is in agreement with the reference. However, for other values of $\sigma_\delta =$ the dose distribution becomes highly heterogeneous in the tumor. The analysis of the DVHs and the dosimetric parameters confirms the visual observation. As summarized in Table 5.11, the error of the $D_{95\%}$ parameter increases with σ_δ from 6.6% to 43.0%, which indicates that the tumor coverage is greatly degraded. The sparing of OARs is also impacted by the change of σ_δ. The error of the average dose received by the OARs increases rapidly from 3.2%. These results show the impact of the σ_δ used to model the accuracy of the motion monitoring system. Moreover, it shows, as one could expect, that the quality of the dose distribution obtained with the compensation depends greatly on the accuracy of the monitoring system. Finally, the errors of the $D_{95\%}$ and $D_{50\%}$ parameters for $\sigma_\delta = 0.3$ cm being slightly greater than 5%, indicates that such compensation strategy would require that the system measuring the motion should have an accuracy smaller than 3 mm.

5.4 Discussion on the compensation

In this chapter we introduced a compensation strategy, which aims at mitigating the impact of motion on the dose distribution. We evaluated it based on a moderate and large motion. Moreover, we studied the use of the margins described in our strategy. Finally, we highlighted the impact of the accuracy modeled for the motion monitoring system used to provide the motion information for the compensation strategy.

The results obtained from the evaluation of the compensation technique for moderate and large motions, showed that it is able to reduce significantly the impact of the motion and provides a dose distribution close to the one obtained for a static delivery. From a clinical point of view, the difference between the compensated and the static dose distributions is clinically acceptable. Based on the study related to the use of margins for the strategy, applying margins provides an equivalent dose distribution and reduces greatly the number of re-scanning which would be interesting for applications where the number of re-scanning must be controlled or minimized. However, it requires more displacements of the beam, which has an impact on the overall treatment time. Finally, the consideration of the accuracy of the monitoring system showed, as one could expect, that the improvements brought by our mitigation strategy decrease with the accuracy.

As previously explained, the compensation strategy has been developed for $2D$ motions. However, it could be improved and more interesting clinically if extended to $3D$ motions by considering the radiological depth changes due to the motion. This could make it an interesting feature to consider in the treatment planning process to improve the robustness of treatment plans to motion. In addition, only rigid body transformation is considered in our implementation. The implementation of deformable body transformation could be part of future improvements.

Finally, our compensation strategy provides a new approach where the beam weights are adapted to the motion. It improves significantly the dose distribution in the patient. However, it would require further research to improve the compensation strategy and show if it could be clinically relevant.

Closing remarks on MSPT

MSPT's advantages

MSPT offers a new tool to study intra-fraction motions in proton-therapy treatments using the spot scanning technique. The first interest of MSPT is to render the impact of intra-fraction motions on the dose distribution for a given treatment plan. This is achieved by simulating the delivery with a low time scale (*e.g.*, 1 ms by default), which can be set by the user. Moreover, it can be used to compare different treatment plans or mitigation strategies, designed to treat a patient, and to observe what are the resulting dose distributions if the patient moves during the treatment in order to find the plan that would be best suited for the motions and the patient. This comparison can also consider different types of motions to improve the robustness of the plan. MSPT has also been developed in such a way that it imports directly the treatment plan and the patient data from DICOM files, which is the standard of the TPS's output data. In addition, MSPT has been designed such that the users could match it to their own proton machine, which make it an adaptable software. Finally, MSPT is an open-source software which make it a research tool that can evolve, be re-usable and be widely available.

MSPT's limitations

MSPT present some limitations. Indeed, the use of an analytical pencil beam model to compute the dose distribution provides a calculation less accurate than with Monte-Carlo simulations. However, this allows a faster calculation of a single pencil beam. The use of a low time scale for the motion simulation reduces the speed of the overall dose distribution calculation. The speed depends also linearly on the number of beam positions in the treatment plan and the size of the CT image being used to model the patient, which can lead to long simulation time and important memory space used if the plan contains a high number of spots or if the size of matrices modeling the patient is high. Finally, the systemic artifact highlighted in Section 4.2.2 can also be a limitation if one wants to compare dose distributions obtained in a patient from a TPS and from MSPT. Such situation would require a further study.

Part III

Some Results in Photon Therapy

Chapter 1

Algorithmic aspects of photon therapy

As mentioned in Part I Section 2.4.2, in photon therapy, a treatment plan provides a set of intensity maps representing a 2D grid for each beam angle of the local levels of intensities that must be achieved by a treatment. The radiation generated by the linac is uniform. Therefore, in order to achieve the varying intensities, this radiation needs to be modulated. For this purpose, each intensity matrix is delivered through an MLC. Radiation can either be blocked by the MLC leaves or pass through the gap between the endpoint of the leaves. Therefore, each intensity map is realized by a sequence of MLC configurations, each of which is maintained for a certain amount of time, corresponding to the intensity and measured in MU.

From an algorithmic point of view, 2D matrices can represent intensity maps where each intensity is given as a positive integer. Therefore, these matrices have to be decomposed into a weighted sum of binary matrices. Parts of the photon beam that are not blocked by the MLC are represented by '1' in the binary matrix and by '0' otherwise. Each binary matrix denotes an MLC configuration and the weight corresponds to the associated intensity. These binary matrices respect the consecutive 1 property (C1P - *i.e.*, the 1s occur consecutively as a single block in each row) to represent a gap between the endpoint of the leaves.

Of course, there are many ways of decomposing a given intensity matrix. So, the challenge is to select the decomposition that can be delivered the most efficiently. While the quality of the decomposition is evaluated based on dosimetric properties, two main criteria assess its efficiency:

- The total beam-on time: the total amount of time the patient is being irradiated. This metric is proportional to the sum of intensities used in the decomposition. It needs to be minimized to lower the excess of dose received.
- The total setup time: the total amount of time spent shaping the apertures. This metric is approximately proportional to the number of matrices used in the decomposition. It needs to be minimized to reduce the duration of a fraction.

Although closely related, these two efficiency criteria are not equivalent. From an algorithmic point of view, these efficiency criteria correspond to minimization problems later referred to as the beam-on time minimization problem and the total setup time minimization problem.

Chapter 2

Algorithmic results in photon therapy

In this chapter, we will present algorithmic results obtained for the minimization problems, introduced in the previous chapter. First, we will provide existing results for these problems obtained for the conventional MLC results that will be used in the following sections. Then, we will introduce new types of MLCs in order to present, in a third part, the results obtained for the minimization problems applied to these MLCs.

Before presenting existing results, let us define more formally the minimization problems as matrix decomposition problems:

- The total beam on time minimization problem:
  Let M be an integer matrix. Let us find a set $S = \{M_1, M_2, \dots M_n\}$ of binary C1P matrices and a set $\alpha = \{\alpha_1, \alpha_2, \dots \alpha_n\}$ of integer values, such that $M = \sum_{i=1}^{n} \alpha_i M_i$, and that minimizes $t_{on} = \sum_{i=1}^{n} \alpha_i$.
- The total setup time minimization problem:
  Let M be an integer matrix. Let us find a set $S = \{M_1, M_2, \dots M_n\}$ of binary C1P matrices and a set $\alpha = \{\alpha_1, \alpha_2, \dots \alpha_n\}$ of integer values, such that $M = \sum_{i=1}^{n} \alpha_i M_i$, and that minimizes $t_{setup} = card(S)$.

2.1 Previous algorithmic results

In this section, we will present existing algorithmic results that will be used in the next sections.

The total beam-on time minimization problem was proven to be solvable in linear time [Ahuja and Hamacher, 2005] for conventional MLCs (introduced in Part I Section 2.4.2). To illustrate this result we can look for an optimal decomposition minimizing the total beam-on time on the following example:

Let M be an integer matrix defined by:

$$\begin{bmatrix} 2 & 4 & 3 & 7 & 1 & 4 & 3 \\ 3 & 4 & 5 & 2 & 1 & 6 & 7 \\ 5 & 1 & 6 & 7 & 3 & 3 & 4 \end{bmatrix}$$

We consider that there are no interactions between the rows, since one row of the intensity map is achieved by one pair of MLC leaves and that the pairs are considered independent. Therefore, each row can be decomposed independently. Let us start for example with the first row R_1:

$$\begin{bmatrix} 2 & 4 & 3 & 7 & 1 & 4 & 3 \end{bmatrix}$$

We start the algorithm by searching for the minimum value of this vector. In R_1, the minimum value is 1. This value will be the weight of the first configuration of the first pair of leaves. Taking the minimum value ensures that a maximum number of positions in the row can be irradiated simultaneously. The binary vector (binary vectors and associated weights will be displayed in green to differentiate easily binary vectors and intensity vectors) corresponding to the configuration is:

$$\begin{bmatrix} 1 & 1 & 1 & 1 & 1 & 1 & 1 \end{bmatrix}$$

After applying the configuration with weight 1, the remaining intensities are:

$$\begin{bmatrix} 1 & 3 & 2 & 6 & 0 & 3 & 2 \end{bmatrix}$$

The value 0 appears in the intensity vector at the 5^{th} position. In order to respect the consecutive 1 property, we must consider independently the left segment ($\begin{bmatrix} 1 & 3 & 2 & 6 \end{bmatrix}$), later referred to as l, and the right segment ($\begin{bmatrix} 3 & 2 \end{bmatrix}$), later referred to as r. This corresponds to using the left or right MLC leave to block the beam at the 5^{th} position. This divides the initial problem into two sub-problems where the same algorithm will be applied. If we start with l, the intensity vector is:

$$\begin{bmatrix} 1 & 3 & 2 & 6 & X & X & X \end{bmatrix}$$

where X, corresponds to positions that must be blocked by the MLC leaves. The minimum value is 1. The binary vectors corresponding to the leaves configuration is:

$$\begin{bmatrix} 1 & 1 & 1 & 1 & 0 & 0 & 0 \end{bmatrix}$$

Once this configuration is applied with the weight 1 the value 0 appears at the first position. Therefore it must be blocked in the future configuration. The remaining intensity vector is:

$$\begin{bmatrix} X & 2 & 1 & 5 & X & X & X \end{bmatrix}$$

The minimum value is 1 and the associated binary vector is:

$$\begin{bmatrix} 0 & 1 & 1 & 1 & 0 & 0 & 0 \end{bmatrix}$$

This results in the following intensity vector:

$$\begin{bmatrix} X & 2 & X & 5 & X & X & X \end{bmatrix}$$

Again, the problem to decompose l is divided into two sub-problems: l_1 to irradiate the 2^{nd} position and l_2 to irradiate the 4^{th} one. The first intensity vector considered is:

$$\begin{bmatrix} X & 2 & X & X & X & X & X \end{bmatrix}$$

The minimum weight is 2 and the associated binary vector is:

$$\begin{bmatrix} 0 & 1 & 0 & 0 & 0 & 0 & 0 \end{bmatrix}$$

Similarly, the weight used for l_2 is 5, and the associated binary vector is:

$$\begin{bmatrix} 0 & 0 & 0 & 1 & 0 & 0 & 0 \end{bmatrix}$$

Then, we repeat the algorithm for r. The intensity vector is:

$$\begin{bmatrix} X & X & X & X & X & 3 & 2 \end{bmatrix}$$

The minimum value is 2. The binary vector associated to this weight 2 is:

$$\begin{bmatrix} 0 & 0 & 0 & 0 & 0 & 1 & 1 \end{bmatrix}$$

The final intensity vector is:

$$\begin{bmatrix} X & X & X & X & X & 1 & X \end{bmatrix}$$

The final weight is 1 and is associated to the binary vector:

$$\begin{bmatrix} 0 & 0 & 0 & 0 & 0 & 1 & 0 \end{bmatrix}$$

Hence, R_1 results from the weighted sum of these configurations:

$$\begin{array}{rl} 1 \times & \begin{bmatrix} 1 & 1 & 1 & 1 & 1 & 1 & 1 \end{bmatrix} \\ +1 \times & \begin{bmatrix} 1 & 1 & 1 & 1 & 0 & 0 & 0 \end{bmatrix} \\ +1 \times & \begin{bmatrix} 0 & 1 & 1 & 1 & 0 & 0 & 0 \end{bmatrix} \\ +2 \times & \begin{bmatrix} 0 & 1 & 0 & 0 & 0 & 0 & 0 \end{bmatrix} \\ +5 \times & \begin{bmatrix} 0 & 0 & 0 & 1 & 0 & 0 & 0 \end{bmatrix} \\ +2 \times & \begin{bmatrix} 0 & 0 & 0 & 0 & 0 & 1 & 1 \end{bmatrix} \\ +1 \times & \begin{bmatrix} 0 & 0 & 0 & 0 & 0 & 1 & 0 \end{bmatrix} \end{array}$$

The resulting beam-on time for R_1 is: $1 + 1 + 1 + 2 + 5 + 2 + 1 = 13$.
Similarly we obtain the following decomposition for the second row R_2:

$$\begin{array}{rl} 1 \times & \begin{bmatrix} 1 & 1 & 1 & 1 & 1 & 1 & 1 \end{bmatrix} \\ +1 \times & \begin{bmatrix} 1 & 1 & 1 & 1 & 0 & 0 & 0 \end{bmatrix} \\ +1 \times & \begin{bmatrix} 1 & 1 & 1 & 0 & 0 & 0 & 0 \end{bmatrix} \\ +1 \times & \begin{bmatrix} 0 & 1 & 1 & 0 & 0 & 0 & 0 \end{bmatrix} \\ +1 \times & \begin{bmatrix} 0 & 0 & 1 & 0 & 0 & 0 & 0 \end{bmatrix} \\ +5 \times & \begin{bmatrix} 0 & 0 & 0 & 0 & 0 & 1 & 1 \end{bmatrix} \\ +1 \times & \begin{bmatrix} 0 & 0 & 0 & 0 & 0 & 0 & 1 \end{bmatrix} \end{array}$$

The resulting beam-on time for R_2 is: $1 + 1 + 1 + 1 + 1 + 5 + 1 = 11$.
The weighted sum of the configuration vectors for the third row R_3 is:

$$\begin{array}{r} 2\times \\ +3\times \\ +1\times \\ +1\times \\ +3\times \\ +1\times \end{array} \begin{bmatrix} 1 & 1 & 1 & 1 & 1 & 1 & 1 \\ 1 & 0 & 0 & 0 & 0 & 0 & 0 \\ 0 & 0 & 1 & 1 & 1 & 1 & 1 \\ 0 & 0 & 0 & 0 & 0 & 0 & 1 \\ 0 & 0 & 1 & 1 & 0 & 0 & 0 \\ 0 & 0 & 0 & 1 & 0 & 0 & 0 \end{bmatrix}$$

The resulting beam-on time for R_3 is: $2+3+1+1+3+1=11$.

According to Ahuja and Hamacher [2005], the optimal beam-on time is the maximum of the rows beam on time. Therefore, in our example the optimal beam-on time $t_{opt} = \max\{13, 11, 11\} = 13$. The construction of the optimal matrix decomposition follows the process: for each row in $\{R_1, R_2, R_3\}$, select a configuration vector: $\{R_{1_1}, R_{2_1}, R_{3_1}\}$ with respective beam-on time $\{w_{1_1}, w_{2_1}, w_{3_1}\}$. Then, construct the matrix:

$$S_1 = \begin{bmatrix} R_{1_1} \\ R_{2_1} \\ R_{3_1} \end{bmatrix}$$

and set the beam-on time of S_1 to $w_{min_1} = \min\{w_{1_1}, w_{2_1}, w_{3_1}\}$. Then reduce the beam-on time of $R_{1_1}, R_{2_1}, R_{3_1}$ by w_{min_1}. If the beam-on time of one of these configuration vectors becomes zero, remove it from the configuration vectors of the corresponding row. For example, if the beam-on time of R_{2_1} becomes zero, remove R_{2_1} from the configuration vectors of R_2. Then repeat the process until no configuration vector remains to obtain the matrices of an optimal decomposition.

Let us apply this iterative process to the rows of M. For example:

$$S_1 = \begin{bmatrix} R_{1_1} \\ R_{2_1} \\ R_{3_1} \end{bmatrix} = \begin{bmatrix} 1 & 1 & 1 & 1 & 1 & 1 & 1 \\ 1 & 1 & 1 & 1 & 1 & 1 & 1 \\ 1 & 1 & 1 & 1 & 1 & 1 & 1 \end{bmatrix}$$

where $w_{1_1} = 1$, $w_{2_1} = 1$, $w_{3_1} = 2$. The beam-on time for S_1 is $w_{min_1} = 1$. After reducing the beam-on time of R_{1_1}, R_{2_1} and R_{3_1} by w_{min_1}, the beam-on times associated to R_{1_1} and R_{2_1} become null. Hence, R_{1_1} and R_{2_1} are removed from the possible configuration vectors, but R_{3_1} can still be used with a beam-on time of 1. If we repeat this process until all the configuration vectors have been removed, a possible optimal solution to minimize the beam-on time is:

$$M = 1\times S_1 + 1\times S_2 + 1\times S_3 + 1\times S_4 + 1\times S_5 + 3\times S_6 + 2\times S_7 + 1\times S_8 + 2\times S_9$$

where:

$$S_2 = \begin{bmatrix} 1 & 1 & 1 & 1 & 0 & 0 & 0 \\ 1 & 1 & 1 & 1 & 0 & 0 & 0 \\ 1 & 1 & 1 & 1 & 1 & 1 & 1 \end{bmatrix}; S_3 = \begin{bmatrix} 0 & 1 & 1 & 1 & 0 & 0 & 0 \\ 1 & 1 & 1 & 0 & 0 & 0 & 0 \\ 0 & 0 & 1 & 1 & 1 & 1 & 1 \end{bmatrix};$$

$$S_4 = \begin{bmatrix} 0 & 1 & 0 & 0 & 0 & 0 & 0 \\ 0 & 1 & 1 & 0 & 0 & 0 & 0 \\ 0 & 0 & 0 & 0 & 0 & 0 & 1 \end{bmatrix} ; S_5 = \begin{bmatrix} 0 & 1 & 0 & 0 & 0 & 0 & 0 \\ 0 & 0 & 1 & 0 & 0 & 0 & 0 \\ 0 & 0 & 0 & 1 & 0 & 0 & 0 \end{bmatrix} ;$$

$$S_6 = \begin{bmatrix} 0 & 0 & 0 & 1 & 0 & 0 & 0 \\ 0 & 0 & 0 & 0 & 0 & 1 & 1 \\ 1 & 0 & 0 & 0 & 0 & 0 & 0 \end{bmatrix} ; S_7 = \begin{bmatrix} 0 & 0 & 0 & 1 & 0 & 0 & 0 \\ 0 & 0 & 0 & 0 & 0 & 1 & 1 \\ 0 & 0 & 1 & 1 & 0 & 0 & 0 \end{bmatrix} ;$$

$$S_8 = \begin{bmatrix} 0 & 0 & 0 & 0 & 0 & 1 & 0 \\ 0 & 0 & 0 & 0 & 0 & 0 & 1 \\ 0 & 0 & 1 & 1 & 0 & 0 & 0 \end{bmatrix} ; S_9 = \begin{bmatrix} 0 & 0 & 0 & 0 & 0 & 1 & 1 \\ 0 & 0 & 0 & 0 & 0 & 0 & 0 \\ 0 & 0 & 0 & 0 & 0 & 0 & 0 \end{bmatrix}$$

Finally, the beam-on time of this optimal solution is: $t_{opt} = 1+1+1+1+1+3+2+1+2 = 13$ as expected.

The second minimization problem, namely the total setup time minimization problem, was proven NP-hard for matrices with at least two rows [Burkard, 2002]. This NP-hardness result was strengthened by Baatar et al. [2005] who proved that even for matrices with a single row the problem is strongly NP-hard.

2.2 Technological variants of MLCs

The conventional MLC, introduced in Part I Section 2.4.2, consists of a set of parallel pairs of leaves that can move towards or apart from each other. However, different MLC settings have been introduced during the last decade: the rotating MLC and the multi-layer MLC.

2.2.1 Rotating MLC

Some recent contributions tackle the use of collimator rotation in the decomposition of a given intensity matrix (*i.e.*, for a given fixed linac angle) [Broderick et al., 2009; Dou et al., 2006; Milette, 2008; Milette et al., 2006; Otto, 2005; Otto et al., 2005; Schmuland, 2006; Wang et al., 2006] (see schematic in Figure 2.1). This technology has been built on delivery machines and the practical efficiency of this technique was stated in [Webb, 2010]. From a Consecutive 1 Property (C1P) point of view, a rotating collimator allows each intensity matrix to be decomposed in both row C1P or column C1P configurations. For example, decomposing the following intensity matrix with only row C1P configurations requires at least 7 of them whereas only 6 configurations are needed if rotation is allowed (the last two configurations are column C1P).

$$\begin{bmatrix} 1 & 4 & 2 & 5 \\ 1 & 3 & 3 & 2 \\ 1 & 3 & 5 & 5 \\ 6 & 4 & 6 & 0 \end{bmatrix} = \begin{bmatrix} 0 & 0 & 0 & 1 \\ 0 & 0 & 1 & 1 \\ 0 & 0 & 1 & 1 \\ 1 & 1 & 1 & 0 \end{bmatrix} + \begin{bmatrix} 0 & 0 & 0 & 1 \\ 0 & 1 & 1 & 1 \\ 0 & 0 & 1 & 1 \\ 1 & 1 & 1 & 0 \end{bmatrix} + \begin{bmatrix} 0 & 1 & 1 & 1 \\ 1 & 1 & 1 & 0 \\ 0 & 1 & 1 & 1 \\ 1 & 1 & 1 & 0 \end{bmatrix} + \begin{bmatrix} 1 & 1 & 1 & 1 \\ 0 & 0 & 0 & 0 \\ 1 & 1 & 1 & 1 \\ 1 & 1 & 1 & 0 \end{bmatrix}$$

$$+ \circlearrowleft$$

$$+\begin{bmatrix}0&1&0&1\\0&0&0&0\\0&0&0&0\\1&0&1&0\end{bmatrix}+\begin{bmatrix}0&1&0&0\\0&1&0&0\\0&1&1&1\\1&0&1&0\end{bmatrix}$$

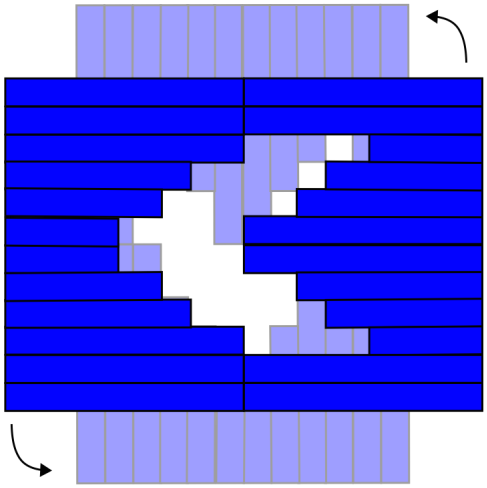

Figure 2.1 – Schematic of a rotating MLC.

2.2.2 Multi-Layer MLC

A Multi-Layer MLC is composed of multiple layers of leaves. It was originally patented by Yao [1997] in 1997 and has been intensively studied since 2003. Most studies consider two orthogonal layers, referred to in the literature as the dual-MLC [Hughes, 2003; Jarray and Picouleau, 2012; Liu et al., 2009, 2008; Oh et al., 2007] (see schematic in Figure 2.2), which has already been tested in some delivery machines [Liu et al., 2009]. Topolnjak et al. investigated the use of three layers placed every 60 degrees [Topolnjak et al., 2005, 2004]. The state-of-the-art is presented in Webb [2012] which claims the efficiency of the gear. For example, decomposing the following intensity matrix with only C1P matrices (even allowing MLC rotations) requires a linear number of configurations whereas only 2 are needed when using a dual-MLC ($\uparrow$ and $\rightarrow$ represent respectively vertical and horizontal blocking leaves).

$$\begin{bmatrix}1&0&1&0&1&\dots&0\\0&1&0&1&0&\dots&1\\1&0&1&0&1&\dots&0\\0&1&0&1&0&\dots&1\\1&0&1&0&1&\dots&0\\\vdots&\vdots&\vdots&\vdots&\vdots&\ddots&\vdots\\0&1&0&1&0&\dots&1\end{bmatrix}=\begin{bmatrix}1&\uparrow&1&\uparrow&1&\dots&\uparrow\\\leftarrow&+&\leftarrow&+&\leftarrow&\dots&+\\1&\uparrow&1&\uparrow&1&\dots&\uparrow\\\leftarrow&+&\leftarrow&+&\leftarrow&\dots&+\\1&\uparrow&1&\uparrow&1&\dots&\uparrow\\\vdots&\vdots&\vdots&\vdots&\vdots&\ddots&\vdots\\\leftarrow&+&\leftarrow&+&\leftarrow&\dots&+\end{bmatrix}+\begin{bmatrix}+&\rightarrow&+&\rightarrow&+&\dots&\rightarrow\\\uparrow&1&\uparrow&1&\uparrow&\dots&1\\+&\rightarrow&+&\rightarrow&+&\dots&\rightarrow\\\uparrow&1&\uparrow&1&\uparrow&\dots&1\\+&\rightarrow&+&\rightarrow&+&\dots&\rightarrow\\\vdots&\vdots&\vdots&\vdots&\vdots&\ddots&\vdots\\\uparrow&1&\uparrow&1&\uparrow&\dots&1\end{bmatrix}$$

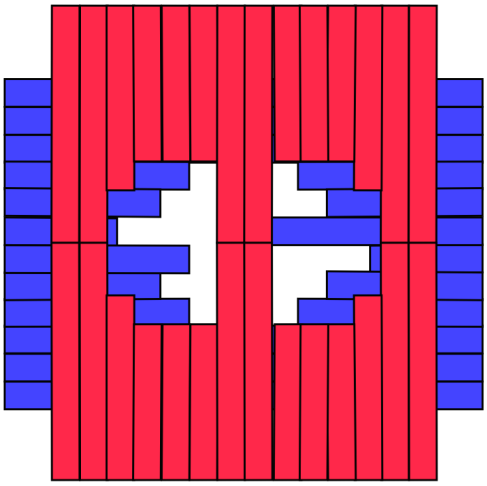

Figure 2.2 – Schematic of a dual-MLC.

2.3 Algorithmic results for new MLC variants

These new variants of MLCs were conjectured to increase the complexity of the total beam on time and total setup time minimization problems, as mentioned in the articles cited previously. However, to the best of our knowledge, this has not been proven. That is why, in the next sections we formally show the algorithmic hardness of these problems. More precisely, we study the Dual-MLC Decomposition (DMD) problem that considers two orthogonal layers of MLCs and the Matrix Orthogonal Decomposition (MOD) problem introduced in [Dou et al., 2006] that considers the decomposition problem of an intensity matrix using a unique 90° rotation. The following results were published in Blin et al. [2014].

2.3.1 Algorithmic results for Dual MLC

In order to prove the hardness of the total setup time minimization problem, we will use the construction of Baatar et al. [2005] as a starting point. Therefore, let us first briefly present a slightly modified version of their proof. As a reminder, they originally proved the hardness of total setup time decomposition even for matrices with a single row by a reduction from the NP-complete 3-Partition problem. This problem asks to partition $3Q$ positive numbers – say $S = (b_1, b_2, \ldots, b_{3Q})$ – (allowing duplicates) into Q triples – say $\{T_1, T_2, \ldots, T_Q\}$, such that each triple has the same sum. Considering that all $3Q$ numbers sum to N, then every triple should have a sum of $B = \frac{N}{Q}$ (we may assume that $\frac{B}{4} < b_i < \frac{B}{2}$ for every $b_i \in S$).

From any instance S of the 3-Partition problem, one can construct in polynomial time an integer vector $A = x_1\ x_2\ \ldots x_{3Q}\ y_Q\ y_{Q-1} \ldots y_1\ z_0$ such that $x_i = \sum_{j=1}^{i} b_j$, $y_i = i \cdot B$ and $z_0 = b_1$[1]. Then, one can ask for a decomposition with at most $3Q$ MLC configurations. As

1. We added z_0 to the original construction for ease of the demonstration

a reminder, any solution of the problem is a set of C1P vectors (*i.e.*, configurations) provided with corresponding intensities. Therefore, for each configuration, we will denote, in the corresponding row vector, by left (respectively right) endpoint the first (respectively last) position of a 1.

First, notice that since $\{x_i | 1 \leq i \leq 3Q\}$ is a set of $3Q$ different values, any decomposition of A will need at least $3Q$ configurations and thus $3Q$ corresponding intensities (among which one is b_1 due to x_1) each having their left endpoint disjointly in one of $\{x_i | 1 \leq i \leq 3Q\}$ positions. Moreover, the configuration with the intensity b_1 is defined as a totally open configuration (*i.e.*, a vector of $4Q + 1$ $1's$). Among the at most $Q \cdot B$ intensity units that can go through x_{3Q}, exactly B of them are needed to irradiate y_1. To respect the consecutiveness of the $1's$, whatever the left endpoints of the configurations used, the corresponding configurations will contribute exactly B to each of $\{y_i | 2 \leq i \leq Q\}$. Repeating this last argument over $\{y_i | 2 \leq i \leq Q\}$, one can prove that each y_i is the right endpoint of some configurations, whose overall contribution sums to B. Furthermore, by construction, z_0 needs b_1 intensity units that has to be included into the B needed by y_1. Consequently, since one of the configurations contributed b_1 to all positions of A, x_2 now only needs an extra b_2 contribution, which should be delivered at once. Repeating this argument over $\{x_i | 3 \leq i \leq 3Q\}$, one can prove that the set of configuration intensities is indeed $\{b_i | 1 \leq i \leq 3Q\}$.

Since, for any $1 \leq i \leq 3Q$, $\frac{B}{4} < b_i < \frac{B}{2}$, any y_i will need to be the right endpoint of exactly 3 configurations to get an overall irradiation summing to B (recall that there are at most $3Q$ configurations). Provided with these properties, one can easily prove that ($\Leftarrow$) given a solution to the 3-Partition problem such that, w.l.o.g., $b_1 \in T_1$, for all $2 \leq i \leq 3Q$, irradiating the interval $[x_i, y_q]$ with intensity b_i, if $b_i \in T_q$, and irradiating the full vector with b_1, leads to a valid decomposition of exactly $3Q$ configurations. Moreover, ($\Rightarrow$) considering any solution of the decomposition problem, defining the triples $\{T_i | 1 \leq i \leq Q\}$ such that $b_j \in T_q \Leftrightarrow$ there exists a configuration of intensity b_i with respectively left and right endpoints x_i and y_q leads to a solution to 3-Partition.

Back to our original problem, we will use a slightly similar reduction using A as a starting point. We, thus now consider the decomposition of a matrix. For ease, in the rest of the paper, $[x]^k$ will denote a sequence of k copies of element x. The reduction is again from the 3-Partition problem. From any instance S, one can construct in polynomial time a matrix $M = (R_1, R_2, \dots R_{6Q+3})$ (illustrated in Figure 2.3) composed of $6Q+3$ rows, where for all $1 \leq i \leq 3Q$, $R_i = R_{6Q+4-i} = [x_{3Q+1-i}]^{4Q+1}$, $R_{3Q+1} = R_{3Q+3} = [0]^{4Q+1}$ and R_{3Q+2} is the vector A designed in the previous proof and ask again for a decomposition with at most $3Q$ Dual-MLC configurations. In other words, the vector A is vertically surrounded by two opposed sorted heaps of vectors (increasing, when going away from A) filled with the $\{x_i | 1 \leq i \leq 3Q\}$ values defined in the previous proof and two null rows.

$$M = \begin{bmatrix} x_{3Q} & x_{3Q} & \dots & x_{3Q} & x_{3Q} & x_{3Q} & \dots & x_{3Q} & x_{3Q} \\ \vdots & \vdots & \vdots & \vdots & \vdots & \vdots & \vdots & \vdots & \vdots \\ x_2 & x_2 & \dots & x_2 & x_2 & x_2 & \dots & x_2 & x_2 \\ x_1 & x_1 & \dots & x_1 & x_1 & x_1 & \dots & x_1 & x_1 \\ 0 & 0 & \dots & 0 & 0 & 0 & \dots & 0 & 0 \\ x_1 & x_2 & \dots & x_{3Q} & y_Q & y_{Q-1} & \dots & y_1 & z_0 \\ 0 & 0 & \dots & 0 & 0 & 0 & \dots & 0 & 0 \\ x_1 & x_1 & \dots & x_1 & x_1 & x_1 & \dots & x_1 & x_1 \\ x_2 & x_2 & \dots & x_2 & x_2 & x_2 & \dots & x_2 & x_2 \\ \vdots & \vdots & \vdots & \vdots & \vdots & \vdots & \vdots & \vdots & \vdots \\ x_{3Q} & x_{3Q} & \dots & x_{3Q} & x_{3Q} & x_{3Q} & \dots & x_{3Q} & x_{3Q} \end{bmatrix}$$

Figure 2.3 – Illustration of Matrix M

The correctness of the proof relies on proving that, whereas one may use the vertical leaves to make a different set of configurations for realizing the peculiar row A, this would not lead to a valid solution. Indeed, the rows R_{3Q+1} and R_{3Q+3} ensures that if a vertical leaf was used to tune the irradiation configuration used for A – say the one in column j – then the corresponding intensity could not be used for any element of column j except in A. Again, since by construction, exactly $3Q$ configurations are required, there will exist at least one row in the end with a non-null value on the column j. This property ensures that if the vertical leaves are used, this is not to disturb the configurations plan of row R_{3Q+2}.

Provided with these properties, one can easily prove that ($\Leftarrow$) given a solution to the 3-Partition problem such that, w.l.o.g., $b_1 \in T_1$, for all $2 \leq j \leq 3Q$, irradiating the interval $R_{3Q+2}[x_j, y_q]$ and fully the rows R_{3Q-j} and R_{6Q+3-j} with intensity b_j if $b_j \in T_q$ and irradiating the full rows R_{3Q}, R_{3Q+2} and R_{3Q+4} with b_1 leads to a valid decomposition of exactly $3Q$ configurations. Moreover, ($\Rightarrow$) considering any solution of the decomposition problem, defining the triples $\{T_i | 1 \leq i \leq Q\}$ such that $b_j \in T_q \Leftrightarrow$ there exists a configuration of intensity b_j with respectively left and right endpoints at x_j and y_q in row R_{3Q+2} leads to a solution to 3-partitioning. This concludes the proof of the following theorem.

Theorem 2.3.1. *The Dual-MLC Decomposition problem is NP-hard when minimizing the total setup time.*

2.3.2 Algorithmic results for Rotating MLC

This section is dedicated to proving a stronger result for the MOD problem: minimizing the total setup time is NP-hard even if the intensity matrix is binary. This result shows that the problem is also NP-hard when one wants to minimize the beam-on time (whereas it is polynomial when the MLC angle is not changed during decomposition). However, we will also prove that the problem can be approximated in this later case. For ease of presentation, we will first introduce a construction using a positive integer

matrix and show afterwards how to make it binary. In order to prove the hardness of the problem, we define a reduction from the NP-complete 3-Hitting Set problem: given a collection $C = \{C_1, \ldots, C_m\}$ of m subsets of size at most three of a finite set $S = \{x_1, \ldots x_n\}$ of n elements and a positive integer k, the problem asks for a subset $S' \subseteq S$ with $|S'| \leq k$ such that S' contains at least one element from each C_i's.

From any instance (C, k) of the 3-Hitting Set problem, one can construct in polynomial time a square matrix M composed of two rows and columns of independent sub-matrices. A sub-matrix of $2n + 9$ columns and $2n + 8$ rows, referred to as M_{DHV}, defined below, is placed top-right of M. Another sub-matrix of $3n + 2$ columns and $m + 4$ rows named M_{3HS}, and defined later on, is placed bottom-left. The rest of the matrix M is filled with 0's in order to obtain a square matrix. One can ask for a decomposition of M with at most $n + 3$ MLC configurations.

The sub-matrix M_{DHV} is designed in such a way that it will ensure that any solution to the decomposition problem will use only one vertical configuration and $(n+2)$ horizontal ones. Indeed, by construction:

- there are $(n + 4)$ horizontal blocks of single $1's$ in the first row.
- all the $2(n + 2)$ last columns are each composed of $(n + 4)$ vertical blocks of single $1's$.

Therefore, any solution (*i.e.*, not inducing more than $(n+3)$ configurations) must have at least one horizontal and one vertical configurations. Moreover, any solution has to use exactly one vertical configuration. Suppose the following contradiction, that a given solution uses more – say k' vertical configurations, then at most k' $1's$ from each column can be irradiated by those k' configurations. Unfortunately, since $k' \leq (n + 2)$, at least two $1's$ per column (except the five leftmost ones) will subsist. In order for the solution to be correct, one would then have to irradiate the remaining $1's$ with a unique horizontal configuration. To do so, the remaining $1's$ should be placed in order to have no more than one 1 per row: presenting a contradiction since we have at least $2 \times (2n + 4)$ $1's$ and at most $2n + 8$ rows. We just proved that the sub-matrix M_{DHV} will force any solution to use exactly one vertical configuration and $(n + 2)$ horizontal ones, each with an intensity of 1.

$$M = \begin{bmatrix} 0 & M_{DHV} \\ M_{3HS} & 0 \end{bmatrix} \texttt{with}$$

$$M_{DHV} = \left[\begin{array}{cccccccccccc} 0 & \mathbf{1} & 0 & \mathbf{1} & 0 & \mathbf{1} & 0 & \mathbf{1} & 0 & \ldots & \mathbf{1} & 0 \\ & & & & 0 & 0 & \mathbf{1} & 0 & \mathbf{1} & \ldots & 0 & \mathbf{1} \\ & & & & 0 & \mathbf{1} & 0 & \mathbf{1} & 0 & \ldots & \mathbf{1} & 0 \\ & & & & \vdots & \vdots & \vdots & \vdots & \vdots & \ldots & \vdots & \vdots \\ & & 0 & & 0 & \mathbf{1} & 0 & \mathbf{1} & 0 & \ldots & \mathbf{1} & 0 \\ & & & & 0 & 0 & \mathbf{1} & 0 & \mathbf{1} & \ldots & 0 & \mathbf{1} \\ & & & & 0 & \mathbf{1} & 0 & \mathbf{1} & 0 & \ldots & \mathbf{1} & 0 \end{array}\right] \texttt{and}$$

$$
M_{3HS} = \left[\begin{array}{lcccccccccccc}
 & & & & & & & & & & & & \\
CTRL_U^V\{ & \mathbf{(n+3)} & 0 & \mathbf{1} & \mathbf{1} & 0 & \mathbf{1} & \mathbf{1} & 0 & \ldots & \mathbf{1} & \mathbf{1} & 0 \\
GATE\{ & 0 & 0 & 0 & 0 & 0 & 0 & 0 & 0 & \ldots & 0 & 0 & 0 \\
CTRL_D^V\{ & \mathbf{(n+2)} & 0 & 0 & 0 & \mathbf{1} & 0 & 0 & \mathbf{1} & \ldots & 0 & 0 & \mathbf{1} \\
CTRL^{max}\{ & \mathbf{(n+2\text{-}k)} & 0 & 0 & \mathbf{1} & \mathbf{1} & \mathbf{1} & \mathbf{1} & \mathbf{1} & \ldots & \mathbf{1} & \mathbf{1} & \mathbf{1} \\
C_1\{ & c_1 & 0 & 0 & \mathbf{1} & x_1^1 & 0 & \mathbf{1} & x_1^2 & \ldots & 0 & \mathbf{1} & x_1^n \\
C_2\{ & c_2 & 0 & 0 & \mathbf{1} & x_2^1 & 0 & \mathbf{1} & x_2^2 & \ldots & 0 & \mathbf{1} & x_2^n \\
 & \vdots & & & & \vdots & & & & & & & \\
C_m\{ & c_m & 0 & 0 & \mathbf{1} & x_m^1 & 0 & \mathbf{1} & x_m^2 & \ldots & 0 & \mathbf{1} & x_m^n \\
 & & & & & \underbrace{\quad} & & & \underbrace{\quad} & & & & \underbrace{\quad} \\
 & & & & & x_1 & & & x_2 & \ldots & & & x_n
\end{array}\right] \} C
$$

Let us now describe the sub-matrix M_{3HS} which is totally independent of M_{DHV} but which will inherit the repartition of the vertical and horizontal configurations that we just showed. M_{3HS} is defined as pictured above and where $x_i^j = \mathbf{2}$ if $x_j \in C_i$; $x_i^j = \mathbf{1}$ otherwise and $c_i = 0$ if $|C_i| = 3$; $c_i = \mathbf{1}$ otherwise. The sub-matrix M_{3HS} is designed to encode the 3-Hitting Set instance. In other words, each subset C_i of C is encoded by a row whereas each element x_i of S is encoded by a column. Let us now prove some interesting properties about this construction.

Let us have a look at the constraints of the unique vertical configuration. Since $CTRL_U^V[0]$ is set to $(n+3)$ – that is both the maximal number of configurations and intensity. The first column of the vertical configuration will have to irradiate $CTRL_U^V[0]$ and so does the corresponding row (*i.e.*, $(2n+9)^{\text{th}}$ of M) of all the horizontal configurations. It has many consequences:

- all the $1's$ of $CTRL_U^V$ will have to be irradiated during the vertical configuration. This yields that no other $1's$ in the corresponding columns can be irradiated during the vertical configuration – namely columns in $\{3j-1, 3j | 1 \leq j \leq n\}$.
- $CTRL_D^V[0]$, $CTRL^{max}[0]$ and any $C_i[0]$ will all only be irradiated by horizontal configurations[2].

Since $CTRL_D^V[0]$ is set to $(n+2)$, all the horizontal configurations for this specific row $CTRL_D^V$ will need to be dedicated to $CTRL_D^V[0]$. This implies, that all remaining $1's$ of $CTRL_D^V$ – that is $\{CTRL_D^V[i] | i = 2+3j, 1 \leq j \leq n\}$ – would have to be vertically irradiated. With the exception of the set of bottom leaves for the columns $\{i = 2+3j | 1 \leq$

2. For ease, in the above description of M_{3HS} matrix, all the cells which will not have a contribution from the vertical configuration have been put in gray.

$j \leq n\}$, we know exactly what is the endpoint position of each leave (top and bottom) of the vertical configuration in M_{3HS}:

- for all $i \in \{0, 3j, 3j-1 | 1 \leq j \leq n\}$ the i^{th} top leave (respectively bottom one) precisely blocks all the rows preceding (respectively succeeding) $CTRL_U^V$.
- column 1 is totally blocked.
- for all $i \in \{3j+1 | 1 \leq j \leq n\}$ the i^{th} top leave precisely blocks all the rows preceding $CTRL_D^V$.

One can observe that any C_i needs at least $(n+3)$ configurations to be realized. This implies that any C_i should be irradiated at least in one of its column by the vertical configuration. By construction, this irradiation can only occur in $(x_i^j)'s$ positions (*i.e.*, $\{3j+1 | 1 \leq j \leq n\}$) moreover set to **2** (otherwise it will not help decreasing the total irradiation needed to realize C_i) – later referred to as target positions. The $CTRL^{max}$ row is designed to ensure that at least $n-k$ cells among $\{CTRL^{max}[3j+1] | 1 \leq j \leq n\}$ will be blocked by bottom leaves. In other words, at least $n-k$ bottom leaves will block all the succeeding rows of $CTRL^{max}$. Thus, at most k bottom leaves will be able to allow vertical irradiation contribution for the target positions. As we just prove, the only difference between both solutions to the decomposition problem is the position of bottom leaves endpoints for positions in $\{3j+1 | 1 \leq j \leq n\}$. Thus, we will characterize any such solution as a set of n positions in $[2n+13, 2n+m+14]$ (corresponding to all possible solutions – $2n+m+14$ being a leave not used at all).

Given these properties, one can easily prove that ($\Leftarrow$) given a solution ($S' \subseteq S$) to 3-Hitting Set problem, for each $1 \leq i \leq n$, if $x_i \in S'$, $P[i] = 2n+m+14$; $P[i] = 2n+13$ otherwise. We claim that P corresponds to valid positions for the bottom leaves in $\{3j+1 | 1 \leq j \leq n\}$. Since S' is a Hitting Set of size at most k, we can ensure that at least one element of each subset in C belongs to S'. This guarantees that all $C_i's$ rows and $CTRL^{max}$ are realized. Moreover, ($\Rightarrow$) considering any solution to the decomposition problem, one can define the Hitting Set S' such that $x_j \in S' \Leftrightarrow$ the position of the $(3j+1)^{\text{th}}$ bottom leaf is strictly greater than $2n+13$.

Let us now try to transform the construction in order to obtain a binary matrix with the same property. First, one can encode the $x_i's$ using two columns rather than one as follows. Insert a column just before each actual column representing an x_i, fill it with $0's$ except on the $CTRL_U^V$ row which has to be set to **1** and the $C_j's$ rows where the corresponding columns have to be set to 0 **1** if $x_i \in C_j$; **1** **1** otherwise. This update is clearly not changing the original proof. The delicate part stands in the replacement of $CTRL_U^V[0]$. Indeed, it should still requires all the horizontal configurations and the vertical one. To do so, one can design a sub-matrix of $2(n+4)$ rows defined as follows:

- each odd row is filled with $0's$.
- the i^{th} even row is defined as $[0]^{i-1}$ **1** $0[1\ 0]^{n+2}[0]^{n+3-i}$.

In other words, the block representing $(n+3)$ (*i.e.*, $[\mathbf{1}\ 0]^{n+3}$) is shifted right of one position every new even row. This ensures that no one under the position of this sub-matrix will be able to have a vertical contribution. Moreover, in any of the corresponding rows, all

the remaining $1's$ will need to be irradiated vertically. We just showed that the properties of the original matrix are preserved. Both $CTRL_D^V[0]$ and $CTRL^{max}[0]$ can be easily replaced by resp. $[0\ 1]^{n+2}[0]^{3n+7}$ and $[0\ 1]^{n+2-k}[0]^{3n+7}$. Again, the properties of the original matrix are preserved. This concludes the proof of the following theorem.

Theorem 2.3.2. *The Matrix Orthogonal Decomposition problem is NP-hard when minimizing either the total setup or the total beam-on time.*

Now, let us prove that there exists an algorithm based on linear programming and rounding techniques that produces an approximate solution for minimizing the total beam-on time. First, recall that for horizontal configurations, rows can be dealt with separately. It is also the case for vertical configurations and columns. Indeed, an intensity matrix is realized by a sequence of MLC configurations each of which is maintained for a certain amount of time (corresponding to the intensity). Since the problem is to minimize the sum of intensities and not the number of configurations, one can always consider that configurations can be changed every unit of time. This implies that any row (column) can be processed independently of the others and that the overall beam-on time will be deduced by the (most) expensive row (column). The problem can be phrased, as an Integer Linear Programming, as defined in Figure 2.4.

$$
\begin{aligned}
&\texttt{minimize} && H + V \\
&\texttt{subject to} && \forall 1 \leq k \leq m, && \sum_{i \leq j} H_{ij}^k \leq H && (2.1)\\
& && \forall 1 \leq k \leq m, && \sum_{i \leq j} V_{ij}^k \leq V && (2.2)\\
& && \forall k, k' \in \{1, \dots m\}^2, && \sum_{i \leq k' \leq j} H_{ij}^k + \sum_{i' \leq k \leq j'} V_{i'j'}^{k'} = M[k][k'] && (2.3)\\
& && \forall i, j, k, && H_{ij}^k \geq 0, V_{ij}^k \geq 0 &&
\end{aligned}
$$

$$1 \leq i \leq j \leq m, 1 \leq i' \leq j' \leq m, H \geq 0, V \geq 0.$$

Figure 2.4 – Integer Linear Program minimizing the total beam-on time for MOD

For any row of the intensity matrix M, let H_{ij}^k be a variable indicating the amount of time the following horizontal configuration is maintained: considering the k^{th} pair of leaves, the left one's endpoint is at position $i-1$ and the right one's endpoint is at position $j+1$. This configuration irradiates any position between i and j in row k. Similarly, for any column of the intensity matrix M, let V_{ij}^k be a variable indicating the amount of time the following vertical configuration is maintained: considering the k^{th} pair of leaves, the left one's endpoint is at position $i-1$ and the right one's endpoint is at position $j+1$. This configuration irradiates any position between i and j in column k. Finally, variables H and V are respectively horizontal and vertical costs of a solution computed respectively as $\max_k \sum_{i \leq j} H_{ij}^k$ and $\max_k \sum_{i \leq j} V_{ij}^k$ (which is encoded by constraints (1) and (2)).

Constraint (3) ensures that the desired intensity matrix is realized. Indeed, $\sum_{i \leq k' \leq j} H_{ij}^k$ (respectively $\sum_{i' \leq k \leq j'} V_{i'j'}^{k'}$) represents the overall contribution of all the horizontal (respectively vertical) configurations contributing to the entry $M[k][k']$. There are about $2m^3+2$ variables, $2n$ inequalities and n^2 equalities. Our linear programming problem can be rewritten with only inequalities. Indeed, each equality constraint may be removed by solving it for variable $H_{0k'}^k$ and substituting this solution into the corresponding form of constraint (1) (*i.e.*, for the corresponding k).

Of course Integer Linear Programming is NP-hard. Therefore, we relax the integrality constraint, that is, allowing all variables to take a non-integral but still positive value. We end-up with a fractional linear program that can be solved in polynomial time. Notice that the solution provided by this linear program cannot be greater than the optimal integer one, since we only allow more solutions to become feasible. We apply a rounding of the fractional solution to obtain an integral feasible solution not too far from optimal.

Assume that $f_L : \{V, H, H_{ij}^k, V_{ij}^k | 1 \leq i \leq j \leq m, 1 \leq k \leq m\} \to \mathbb{R}$ is an optimal fractional solution of the relaxed version of our problem. If one slightly modifies the values of H_{ij}^k 's then due to constraint (3) the values of $V_{i'j'}^{k'}$'s will need to be modified accordingly and with a comparable amount. The basic idea is to provide an integral rounding of the horizontal configurations and compute in polynomial time the corresponding vertical configurations while guaranteeing that the corresponding solution is a good approximation of the optimal one.

Let us present the rounding technique for a single row – say the k^{th}. Considering all the corresponding variables $\{H_{ij}^k | 1 \leq i \leq j \leq m\}$, one can represent each non-null variable H_{ij}^k by an interval $[i, j]$ over the real line on $[1, m]$ weighted by H_{ij}^k. To illustrate the process we will use the k^{th} row presented in Figure 2.5.

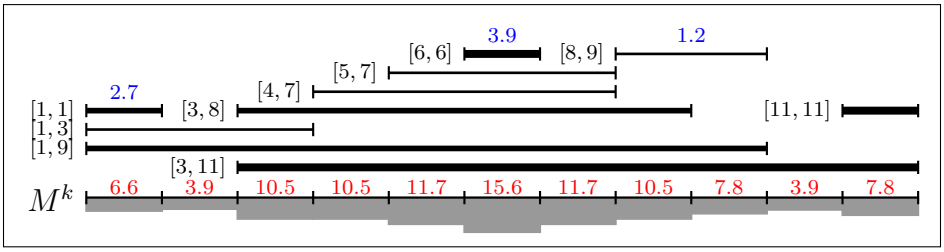

Figure 2.5 – Initial state of the rounding technique: the k^{th} row of the horizontal configurations. A segment $[x, y]$ of weight w (in blue) is represented by a line which thickness corresponds to the weight. For each column, the resulting weight is in red.

Let us transform this set of intervals $\mathcal{I}$ into a set $\mathcal{I}'$, where given any pair of intervals either one is included into the other or they are disjoint. To do so, we process $\mathcal{I}$ with the following algorithm:

1. While there exists two intervals $[i, j]$ and $[k, l]$ with respective weights w_1 and w_2 such that $i < k < j < l$ (*i.e.*, crossing) remove $[i, j]$ and $[k, l]$ from $\mathcal{I}$ and add

$[i, k-1]$, $[k, j]$ and $[j+1, l]$ with respective weights w_1, $w_1 + w_2$ and w_2. This aims at transforming the set of interval into a set where intervals are either nested or independent. For example, in Figure 2.5, the interval $[1, 9]$ of weight 2.7 and $[3, 11]$ of weight 3.9: we remove them from the initial set. Then we add 3 intervals (see Figure 2.6): $[1, 2]$ of weight 2.7, $[3, 9]$ of weight $3.9 + 2.7 = 6.6$ and $[10, 11]$ of weight 3.9.

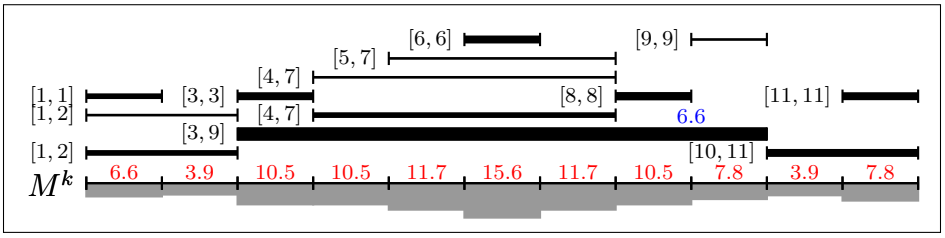

Figure 2.6 – First step: Transform the original set into a set where intervals are either nested or independent.

2. Now that all intervals are nested or independent:
   - given two copies of an interval $[i, j]$ with respective weights w_1 and w_2, remove them and add an interval $[i, j]$ with weight $w_1 + w_2$. For example (see Figure 2.7), the intervals $[1, 2]$ of weight w_1 and $[1, 2]$ of weight w_2 are removed from the original set and the interval $[1, 2]$ of weight $w_1 + w_2$ is added.

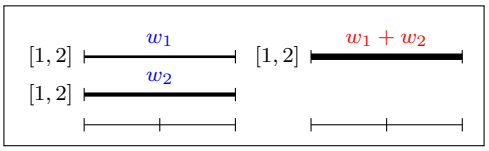

Figure 2.7 – Second step - first possible transformation: copy of an interval. (Left : initial interval set, right: resulting interval set)

   - while there exists three intervals $[x, y]$, $[i, j]$ and $[k, l]$ with respective weights w_1, w_2 and w_3 such that $x \leq i < j \leq k < l \leq y$:
     - if $j < k$ then remove $[x, y]$ from $\mathcal{I}$ and add $[x, j]$ and $[j + 1, y]$ both weighted by w_1.For example (see Figure 2.8), the interval $[1, 5]$ of weight w_1 is removed and the intervals $[1, 3]$ and $[4, 5]$ of weight w_1 are added.

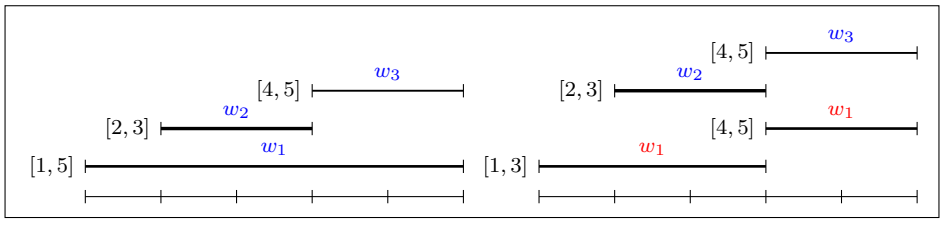

Figure 2.8 – Second step - second possible transformation. (Left : initial interval set, right: resulting interval set)

– Otherwise ($j = k$) remove $[i, j]$ and $[k, l]$ from $\mathcal{I}$. If $w_2 < w_3$ then add $[i, l]$ and $[k, l]$ with respective weights w_2 and $w_3 - w_2$. Otherwise ($w_2 \geq w_3$) add $[i, l]$ and $[i, j]$ with respective weights w_3 and $w_2 - w_3$. For example (see Figure 2.9), the intervals $[3, 4]$ of weight w_3 and $[2, 3]$ of weight w_2 are removed and the intervals $[3, 4]$ of weight $w_3 - w_2$ and $[2, 4]$ of weight w_2 are added.

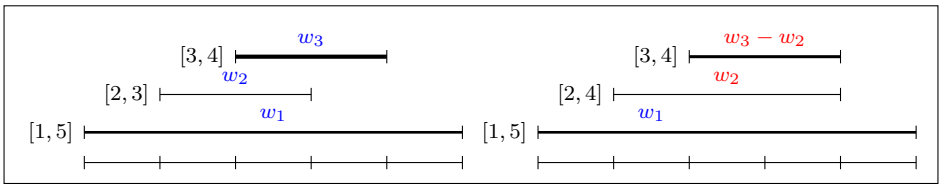

Figure 2.9 – Second step - third possible transformation. (Left : initial interval set, right: resulting interval set)

We end up with a set of independent subsets of nested intervals (later referred to as a *stack*) as illustrated in Figure 2.10. Note that there are at most m such stacks. We will proceed to the rounding of each stack separately. We will do so while ensuring that the sum of the original weights is smaller than the sum of the rounded ones with a gap of at most 1. This will induce that for a given row of the horizontal configuration, we manage to get an integral solution with an at most m extra cost. For ease, considering the stack as increasingly sorted by interval size and let w_i and w'_i denote respectively the original and rounded weights of the i^{th} interval of the stack. The rounding algorithm proceeds as follows: start from the wider interval and round up w_1[3]. Then consider iteratively each remaining interval – say the j^{th}, round it down if possible – that is if $\lfloor w_j \rfloor + \sum_{i=1}^{j-1} w'_i \geq \sum_{i=1}^{j} w_i$ – round it up otherwise.

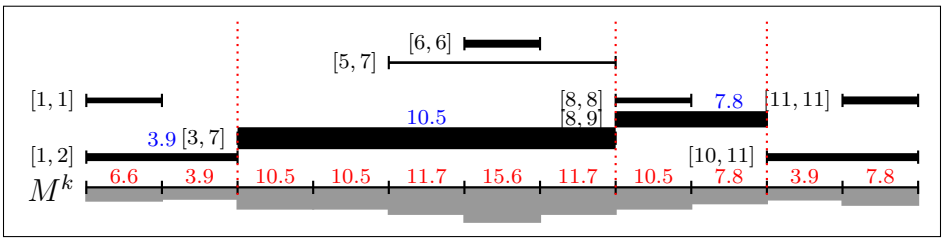

Figure 2.10 – Set of stacks delimited by red dotted lines.

Let us proceed to the rounding of the stacks in Figure 2.10:

- 1^{st} stack:
  1. Round up $[1, 2]$: $3.9 \Rightarrow 4$ (since it's the first stack interval).
  2. Round up $[1, 1]$: $2.7 \Rightarrow 3$ (since $(2 + 4) < (2.7 + 3.9)$).
- 2^{nd} stack:

3. One cannot do differently since there exists at least one position not covered by another interval.

1. Round up $[3, 7]$: $10.5 \Rightarrow 11$
2. Round down $[5, 7]$: $1.2 \Rightarrow 1$ (since $(1 + 11) \geq (1.2 + 10.5)$).
3. Round up $[6, 6]$: $3.9 \Rightarrow 4$

- 3^{rd} stack:
  1. Round up $[8, 9]$: $7.8 \Rightarrow 8$
  2. Round up $[8, 8]$: $2.7 \Rightarrow 3$
- 4^{th} stack:
  1. Round up $[10, 11]$: $3.9 \Rightarrow 4$
  2. Round up $[11, 11]$: $3.9 \Rightarrow 4$

Finally, we obtain the following rounded solution for the k^{th} row: see Figure 2.11.

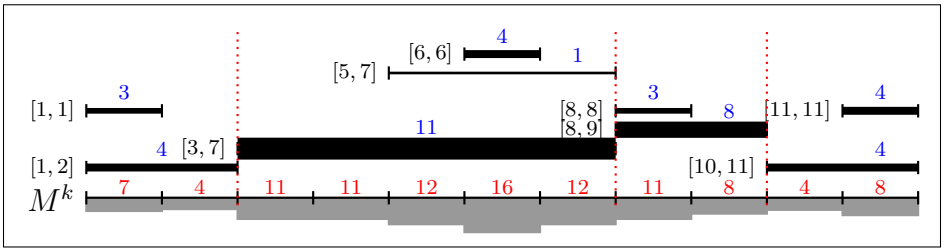

Figure 2.11 – Resulting rounded solution.

Applying the rounding to each row of the horizontal configurations leads to an integral solution for the horizontal configurations that we can subtract for the original intensity matrix. Then, we compute in polynomial time the vertical configurations on the resulting matrix. We claim that the overall solution is at most $2m$ from the optimal solution. Indeed, in the resulting matrix, each cell is at most greater by one than the fractional matrix. This means that the sum of the elements in any column is at most greater by m than the fractional matrix. Thus, we loose at most m with the rounding of the horizontal configurations plus at most m for adjusting the vertical configurations, for a total of a $2m$ additional cost.

This approximation algorithm could yield new interests in the use of rotating MLCs in order to reduce the duration of the patient irradiation and the unnecessary dose to preserve healthy tissues.

Conclusion and future directions

Conclusion

The primary goal of this thesis was to improve the robustness to motion of proton therapy treatments using the spot scanning technique. Due to the limited availability of 4D treatment planning system to simulate these treatments we developed `MSPT`, an open-source software able to perform a 4D simulation of the treatment delivery while considering patient motions during the delivery (*i.e.*, intra-fraction motions).

A series of tests was performed to evaluate `MSPT`'s dose calculation. A first set simulating the delivery of single proton beams of energies varying between 30 MeV and 230 MeV with a step of 5 MeV in a volume of water showed an excellent agreement with the corresponding dose distributions simulated with the beam model *ProtonMachine* from the commercial software RayStation (RaySearch Laboratories). In a second set we simulated the delivery of treatments planned for patient cases. The dose distributions obtained in `MSPT` and in *ProtonMachine* were coherent, however a systemic artifact was observed in `MSPT`'s calculation. This artifact results in higher dose on the distal border of the tumor and a lower dose after the tumor. The cause of this artifact was investigated but couldn't be found. The main assumption is that it is linked to the radiological depth calculation. Therefore, `MSPT` couldn't be used to perform comparison with dose distributions obtained from a treatment planning system in order to study intra-fraction motions. Such motions must be studied between simulations performed in `MSPT`.

We proposed a new strategy to reduce the impact of motion on the dose distribution in the patient body due to intra-fraction motions. This strategy aims at compensating the motion by an adaptation of pencil beam weights used in the treatment based on patient motions and by several re-scanning of each energy layer. We also added a feature to add beam new beam positions with a weight null. This ensures a larger number of beam positions that can be used for the compensation. These new positions are called *margin*. Moreover, the compensation strategy relies on the assumption that the patient position is obtained during the delivery via a motion monitoring system. The accuracy of the monitoring system can be modified for the simulation but is not taken into account in the mitigation technique.

To show some interests and limitations of our motion compensation strategy we performed a series of tests. A first set of simulations aimed at showing the difference between the dose distribution for a static patient and a dynamic patient being treated with and without the compensation technique for a moderate and a large motion amplitude. These simulations showed that for both motion amplitudes the impact of motion was greatly

reduced and provided a dose distribution close to the static situation and clinically acceptable. The accuracy of the compensated dose distribution relies on the spatial parameters controlling whether the compensation is possible or not for a specific beam position. The larger these parameters are the larger the errors are. A second set of simulations was performed to compare compensated deliveries with and without margin. These simulations showed that dose distributions are comparable with and without a margin. However, we showed that the use of a margin allows reducing greatly the number of re-scanning per energy layer but increases the number of beam shifts. This greater number of transition results in a longer delivery. Therefore, a margin could be used when the number of repainting must be controlled and must be minimized. A last set of simulations was achieved to evaluate the impact of the accuracy of the motion monitoring system on the compensation strategy. These last experiments revealed that the accuracy of the motion monitoring system plays an important role in the quality of the resulting dose distribution and that the standard deviation of the measurement error should be less than 3 mm.

`MSPT` and the compensation technique provide new possibilities and a new approach both for the study of intra-fraction and the improvement of the treatment robustness to these motions.

A secondary study focused on the study of new technologies of MLCs for the delivery of photon therapy treatments from an algorithmic point of view. The underlying problem is to find a set of MLC configurations achieving the treatment, which minimizes the total setup time (*i.e.*, minimize the number of configuration), and which minimizes the total beam-on time (*i.e.*, minimize the sum of intensities used for the configurations). The new MLCs are namely the rotating MLC and the dual-layer MLC. These new variants were conjectured to increase the complexity of the minimization problems. However, to the best of our knowledge, this has not been demonstrated. We proved the hardness of the decomposition for these MLCs. In addition, we proposed a polynomial time approximation algorithm to obtain a decomposition, of the rotating MLC, minimizing the total beam-on time.

Future work

Throughout the development of MSPT we simulated the patient motions with rigid body transformations. Motions such as breathing are not applied to the entire body in a same way. For example, upper regions of the lungs tend to move less than lower regions. The use of deformable transformations could provide more accurate simulations and more accurate dose distributions. Moreover, other MSPT improvements could be achieved such as the capability of loading 4D CT dataset that could be used both for the patient and motion modeling. This feature could bring more interest to MSPT and would facilitate simulations of real patient cases.

In Part II Section 4.2.2, we showed the MSPT systemic artifact that tends to overdose the border of the tumor when comparing the dose distributions obtained from the TPS, which computed the treatment plan MSPT uses, and the one computed in MSPT. Despite an investigation, the exact cause was not found and we assume it to be related to the radiological depth calculation in the patient. Therefore, if one were to use MSPT to compare the dose distributions computed by our software and by a TPS, a deeper investigation would be necessary.

As previously mentioned, MSPT could be improved with motions relying on deformable transformations. If such transformation was implemented, the compensation technique could be evaluated which could lead to new improvements of the strategy. Moreover, extending the strategy to 3D motions and taking into account the radiological depth would allow a more general application of our approach.

Finally, further algorithmic research on the non-conventional MLCs could be led to try to find efficient decomposition methods for the problems that are not solvable with the approximation algorithm proposed. In addition, if such algorithm were found, their application could be the topic of other studies to measure the improvements brought by these MLCs combined with these algorithms.

Bibliography

Agostinelli, S., Allison, J., Amako, K., Apostolakis, J., Araujo, H., Arce, P., Asai, M., Axen, D., Banerjee, S., Barrand, G., Behner, F., Bellagamba, L., Boudreau, J., Broglia, L., Brunengo, A., Burkhardt, H., Chauvie, S., Chuma, J., Chytracek, R., Cooperman, G., Cosmo, G., Degtyarenko, P., Dell'Acqua, A., Depaola, G., Dietrich, D., Enami, R., Feliciello, A., Ferguson, C., Fesefeldt, H., Folger, G., Foppiano, F., Forti, A., Garelli, S., Giani, S., Giannitrapani, R., Gibin, D., Gómez Cadenas, J., González, I., Gracia Abril, G., Greeniaus, G., Greiner, W., Grichine, V., Grossheim, A., Guatelli, S., Gumplinger, P., Hamatsu, R., Hashimoto, K., Hasui, H., Heikkinen, A., Howard, A., Ivanchenko, V., Johnson, A., Jones, F., Kallenbach, J., Kanaya, N., Kawabata, M., Kawabata, Y., Kawaguti, M., Kelner, S., Kent, P., Kimura, A., Kodama, T., Kokoulin, R., Kossov, M., Kurashige, H., Lamanna, E., Lampén, T., Lara, V., Lefebure, V., Lei, F., Liendl, M., Lockman, W., Longo, F., Magni, S., Maire, M., Medernach, E., Minamimoto, K., Mora de Freitas, P., Morita, Y., Murakami, K., Nagamatu, M., Nartallo, R., Nieminen, P., Nishimura, T., Ohtsubo, K., Okamura, M., O'Neale, S., Oohata, Y., Paech, K., Perl, J., Pfeiffer, A., Pia, M., Ranjard, F., Rybin, A., Sadilov, S., Di Salvo, E., Santin, G., Sasaki, T., Savvas, N., Sawada, Y., Scherer, S., Sei, S., Sirotenko, V., Smith, D., Starkov, N., Stoecker, H., Sulkimo, J., Takahata, M., Tanaka, S., Tcherniaev, E., Safai Tehrani, E., Tropeano, M., Truscott, P., Uno, H., Urban, L., Urban, P., Verderi, M., Walkden, A., Wander, W., Weber, H., Wellisch, J., Wenaus, T., Williams, D., Wright, D., Yamada, T., Yoshida, H., and Zschiesche, D. (2003). Geant4 — a simulation toolkit. *Nuclear Instruments and Methods in Physics Research Section A: Accelerators, Spectrometers, Detectors and Associated Equipment*, 506(3):250–303.

Ahuja, R. and Hamacher, H. (2005). A network flow algorithm to minimize beam-on time for unconstrained multileaf collimator problems in cancer radiation therapy. *Networks*, 45(1):36–41.

Allison, J., Amako, K., Apostolakis, J., Araujo, H., Dubois, P. A., Asai, M., Barrand, G., Capra, R., Chauvie, S., Chytracek, R., Cirrone, G. A. P., Cooperman, G., Cosmo, G., Cuttone, G., Daquino, G. G., Donszelmann, M., Dressel, M., Folger, G., Foppiano, F., Generowicz, J., Grichine, V., Guatelli, S., Gumplinger, P., Heikkinen, A., Hrivnacova, I., Howard, A., Incerti, S., Ivanchenko, V., Johnson, T., Jones, F., Koi, T., Kokoulin, R., Kossov, M., Kurashige, H., Lara, V., Larsson, S., Lei, F., Link, O., Longo, F., Maire, M., Mantero, A., Mascialino, B., McLaren, I., Lorenzo, P. M., Minamimoto, K., Murakami, K., Nieminen, P., Pandola, L., Parlati, S., Peralta, L., Perl, J., Pfeiffer, A., Pia, M. G., Ribon, A., Rodrigues, P., Russo, G., Sadilov, S., Santin, G., Sasaki, T., Smith, D., Starkov, N., Tanaka, S., Tcherniaev, E., Tome, B., Trindade, A., Truscott,

P., Urban, L., Verderi, M., Walkden, A., Wellisch, J. P., Williams, D. C., Wright, D., and Yoshida, H. (2006). Geant4 developments and applications. *IEEE Transactions on Nuclear Science*, 53(1):270–278.

Archambault, L. and Beaulieu, L. (2003). Overview of Geant4 applications in medical physics. *IEEE Nuclear Science Symposium Conference Record 2003*, 3:1743–1745.

Baatar, D., Hamacher, H., Ehrgott, M., and Woeginger, G. (2005). Decomposition of integer matrices and multileaf collimator sequencing. *Discrete Applied Mathematics*, 152(1-3):6–34.

Baumrind, S. (2011). The road to three-dimensional imaging in orthodontics. *Seminars in Orthodontics*, 17(1):2–12.

Berger, M., Coursey, J., Zucker, M., and Chang, J. (2005). ESTAR, PSTAR, and ASTAR: Computer Programs for Calculating Stopping-Power and Range Tables for Electrons, Protons, and Helium Ions (version 1.2.3). http://physics.nist.gov/Star.

Bert, C. and Durante, M. (2011). Motion in radiotherapy: particle therapy. *Physics in Medicine and Biology*, 56(16):R113.

Bert, C., Gemmel, A., Saito, N., Chaudhri, N., Schardt, D., Durante, M., Kraft, G., and Rietzel, E. (2010). Dosimetric precision of an ion beam tracking system. *Radiation Oncology*, 5:61.

Bert, C., Richter, D., Durante, M., and Rietzel, E. (2012). Scanned carbon beam irradiation of moving films: comparison of measured and calculated response. *Radiation Oncology*, 7(1):55–67.

Blin, G., Morel, P., Rizzi, R., and Vialette, S. (2014). Towards Unlocking the Full Potential of Multileaf Collimators. In Geffert, V., Preneel, B., Rovan, B., Štuller, J., and Tjoa, A., editors, *SOFSEM 2014: Theory and Practice of Computer Science SE - 13*, volume 8327 of *Lecture Notes in Computer Science*, pages 138–149. Springer International Publishing.

Brahme, a., Roos, J. E., and Lax, I. (1982). Solution of an integral equation encountered in rotation therapy. *Physics in medicine and biology*, 27(10):1221–1229.

Broderick, M., Leech, M., and Coffey, M. (2009). Direct aperture optimization as a means of reducing the complexity of Intensity Modulated Radiation Therapy plans. *Radiation Oncology*, 4:8.

Bryant, P. J. (2010). History and Applications of Accelerators. Lecture at CERN Accelerator School, Varn (Bulgaria), from http://cas.web.cern.ch/cas/Bulgaria-2010/Talks-web/Bryant-web.pdf.

Burkard, R. (2002). Open problem session, Oberwolfach Conference on Combinatorial Optimization. November 24-29.

Chan, A. W. and Liebsch, N. J. (2008). Proton radiation therapy for head and neck cancer. *Journal of Surgical Oncology*, 97(8):697–700.

Clair, W. H. S., Adams, J. A., Bues, M., Fullerton, B. C., Shell, S. L., Kooy, H. M., Loeffler, J. S., and Tarbell, N. J. (2004). Advantage of protons compared to conventional X-ray or IMRT in the treatment of a pediatric patient with medulloblastoma. *International Journal of Radiation Oncology, Biology, Physics*, 58(3):727–734.

Connell, P. P. and Hellman, S. (2009). Advances in radiotherapy and implications for the next century: a historical perspective. *Cancer Research*, 69(2):383–392.

Ding, X., Bues, M., Zhu, M., Gaza, R., and Smith, A. (2007). Su-ff-t-291: Measurement of the mechanical isocenter of a proton gantry. *Medical Physics*, 34(6):2468–2468.

Dou, X., Wu, X., Bayouth, J., and Buatti, J. (2006). The matrix orthogonal decomposition problem in intensity-modulated radiation therapy. In Chen, D. and Lee, D., editors, *Computing and Combinatorics*, volume 4112 of *Lecture Notes in Computer Science*, pages 156–165. Springer Berlin Heidelberg.

Eckermann, M., Hillbrand, M., Herbst, M., and Rinecker, H. (2011). Scanning proton beam radiotherapy under functional apnea. *In Proceedings of the 50th Conference of the Particle Therapy Co-Operative Group (PTCOG)*.

Eley, J. G., Newhauser, W. D., Lüchtenborg, R., Graeff, C., and Bert, C. (2014). 4D optimization of scanned ion beam tracking therapy for moving tumors. *Physics in Medicine and Biology*, 59(13):3431–3452.

Fuss, M., Hug, E. B., Schaefer, R. a., Nevinny-Stickel, M., Miller, D. W., Slater, J. M., and Slater, J. D. (1999). Proton radiation therapy (PRT) for pediatric optic pathway gliomas: comparison with 3D planned conventional photons and a standard photon technique. *International Journal of Radiation Oncology, Biology, Physics*, 45(5):1117–1126.

Fuss, M., Poljanc, K., Miller, D. W., Archambeau, J. O., Slater, J. M., Slater, J. D., and Hug, E. B. (2000). Normal tissue complication probability (NTCP) calculations as a means to compare proton and photon plans and evaluation of clinical appropriateness of calculated values. *International journal of cancer. Journal international du cancer*, 90(6):351–358.

George, R., Vedam, S. S., Chung, T. D., Ramakrishnan, V., and Keall, P. J. (2005). The application of the sinusoidal model to lung cancer patient respiratory motion. *Medical Physics*, 32(9):2850–2861.

Goethals, P.-E. and Zimmermann, R. (2013). Proton therapy world market report. Technical report, MED rays intell.

Goitein, M. and Chen, G. T. Y. (1983). Beam scanning for heavy charged particle radiotherapy. *Medical Physics*, 10(6):831–840.

Grözinger, S. O., Bert, C., Haberer, T., Kraft, G., and Rietzel, E. (2008). Motion compensation with a scanned ion beam : a technical feasibility study. *International Journal of Radiation Oncology, Biology, Physics*, 3(1):34–40.

Grunder, H. A. and Leemann, C. W. (1977). Present and future sources of protons and heavy ions. *International Journal of Radiation Oncology, Biology, Physics*, 3(0):71–80.

Gupta, V. K. (1995). Brachytherapy - Past, Present And Future YR. *Journal of Medical Physics*, 20(2):31–38.

Hamacher, H. and Küfer, K.-H. (2002). Inverse radiation therapy planning - a multiple objective optimization approach. *Discrete Applied Mathematics*, 118(1-2):145–161.

Hansen, E. K., Bucci, M. K., Quivey, J. M., Weinberg, V., and Xia, P. (2006). Repeat CT imaging and replanning during the course of IMRT for head-and-neck cancer. *International Journal of Radiation Oncology, Biology, Physics*, 64(2):355–362.

Heath, E., Unkelbach, J., and Oelfke, U. (2009). Incorporating uncertainties in respiratory motion into 4D treatment plan optimization. *Medical Physics*, 36(7):3059.

Hong, L., Goitein, M., Bucciolini, M., Comiskey, R., Gottschalk, B., Rosenthal, S., Serago, C., and Urie, M. (1996). A pencil beam algorithm for proton dose calculations. *Physics in medicine and biology*, 41(8):1305–1330.

Hughes, J. (2003). US Patent 6600810: Multiple layer multileaf collimator design to improve resolution and reduce leakage.

Hughes, S., McClelland, J., and Tarte, S. (2008). Assessment of respiratory cycle variability with and without training using a visual guide. *Cancer Therapy*, 6:945–954.

Hunter, J. D. (2007). Matplotlib: A 2D Graphics Environment. *Computing in Science & Engineering*, 9(3):90–95.

International Commission on Radiation Units and Measurements (2008). 5 Geometric Terms, and Dose and Dose-Volume Definitions. *Journal of the ICRU*, 7(2):83–94.

International Electrotechnical Commission (2011). IEC 61217 Radiotherapy equipment - Coordinates, movements and scales. Technical report, International Electrotechnical Commission.

Ising, G. (1924). Prinzip einer methode zur herstellung von kanalstrahlen hoher voltzahl. *Arkiv Fuer Matematik, Astronomi Och Fysik, Band*, 18(30):1–4.

Jarray, F. and Picouleau, C. (2012). Minimum decomposition into convex binary matrices. *Discrete Applied Mathematics*, 160(7–8):1164 – 1175.

Jones, E., Oliphant, T., and Peterson, P. (2001). SciPy: Open source scientific tools for Python.

Kang, J. H., Wilkens, J. J., and Oelfke, U. (2007). Demonstration of scan path optimization in proton therapy. *Medical Physics*, 34(9):3457–3464.

Keall, P. J., Mageras, G. S., Balter, J. M., Emery, R. S., Forster, K. M., Jiang, S. B., Kapatoes, J. M., Low, D. a., Murphy, M. J., Murray, B. R., Ramsey, C. R., Van Herk, M. B., Vedam, S. S., Wong, J. W., and Yorke, E. (2006). The management of respiratory motion in radiation oncology report of AAPM Task Group 76. Technical Report 10, Amercian Association of Physicists in Medicine.

Khan, F. M. (2010). *The Physics of Radiation Therapy*. Lippincott Williams & Wilkins.

Kirsch, D. G. and Tarbell, N. J. (2004). Conformal radiation therapy for childhood CNS tumors. *The oncologist*, 9(4):442–450.

Kobayashi, H., Kodaira, T., Yamada, T., Horikawa, Y., Ito, Y., Murao, T., Obata, Y., and Ishigaki, T. (1996). 18 years of conformation radiotherapy at Nagoya University Hospital. *Nagoya journal of medical science*, 59(1-2):17–24.

Kraus, K. M., Heath, E., and Oelfke, U. (2011). Dosimetric consequences of tumour motion due to respiration for a scanned proton beam. *Physics in medicine and biology*, 56(20):6563–6581.

Lawrence, J. H. (1957). Proton irradiation of the pituitary. *Cancer*, 10(4):795–798.

Lee, M., Wynne, C., Webb, S., Nahum, a. E., and Dearnaley, D. (1994). A comparison of proton and megavoltage X-ray treatment planning for prostate cancer. *Radiotherapy and oncology : journal of the European Society for Therapeutic Radiology and Oncology*, 33(3):239–253.

Lin, R., Hug, E. B., Schaefer, R. a., Miller, D. W., Slater, J. M., and Slater, J. D. (2000). Conformal proton radiation therapy of the posterior fossa: a study comparing protons with three-dimensional planned photons in limiting dose to auditory structures. *International Journal of Radiation Oncology, Biology, Physics*, 48(4):1219–1226.

Liu, Y., Shi, C., Lin, B., and Ha, C. (2009). Delivery of four-dimensional radiotherapy with TrackBeam for moving target using a dual-layer MLC: dynamic phantoms study. *Journal of Applied Clinical Medical Physics*, 10(2):1–21.

Liu, Y., Shi, C., Tynan, P., and Papanikolaou, N. (2008). Dosimetric characteristics of dual-layer multileaf collimation for small-field and intensity-modulated radiation therapy applications. *Journal of Applied Clinical Medical Physics*, 9(2):2709.

Low, D. A., Harms, W. B., Mutic, S., and Purdy, J. a. (1998). A technique for the quantitative evaluation of dose distributions. *Medical Physics*, 25(5):656–661.

Lujan, A., Larsen, E., Balter, J., and Haken, R. T. (1999). A method for incorporating organ motion due to breathing into 3D dose calculations. *Medical Physics*, 26(5):715–720.

Mason, D. (2012). PyDICOM 0.9.7. Python package for DICOM files: http://code.google.com/p/pydicom/.

Medical Imaging and Technology Alliance (2011). Ps 3.3-2011 digital imaging and communications in medicine (dicom) part 3: Information object definitions. Technical report, National Electrical Manufacturers Association.

Milette, M. (2008). *Direct optimization of 3D dose distributions using collimator rotation*. PhD thesis, University Of British Columbia.

Milette, M., Rolles, M., and Otto, K. (2006). TU-C-224A-06: Exploiting the Full Potential of MLC Based Aperture Optimization Through Collimator Rotation. *Medical Physics*, 33(6):2191.

Minohara, S., Kanai, T., Endo, M., Noda, K., and Kanazawa, M. (2000). Respiratory gated irradiation system for heavy-ion radiotherapy. *International Journal of Radiation Oncology, Biology, Physics*, 47(4):1097–1103.

Oh, S., Jung, W., and Suh, T. (2007). SU-FF-T-28: A New Concept of Multileaf Collimator (dual-Layer MLC). *Medical Physics*, 34(6):2407.

Otto, K. (2005). US Patent 6907105: Methods and apparatus for planning and delivering intensity modulated radiation fields with a rotating multileaf collimator.

Otto, K., Milette, M., and Schmuland, M. (2005). SU-FF-T-104: Rotating Aperture Optimization - Planning and Delivery Characteristics. *Medical Physics*, 32(6):1973.

Paganetti, H., Bert, C., Clasie, B. M., Craft, D., Engelsman, M., Flampouri, S., Flanz, J. B., Gottschalk, B., Ipe, N. E., Kooy, H. M., Li, Z., Lomax, A. J., Lu, H.-M., Palmans, H., Palta, J. R., Parodi, K., Schippers, M., Slopsema, R., Trofimov, A. V., Unkelbach, J., Van Luijk, P., and Yeung, D. K. (2012). *Proton Therapy Physics*. Taylor & Francis Group, LLC, series in medical physics and biomedical engineering edition.

Paganetti, H. and Bortfeld, T. (2005). Proton Beam Radiotherapy - The State of the Art. Technical report, Massachusetts General Hospital, Boston, MA.

Pedroni, E., Bearpark, R., Böhringer, T., Coray, A., Duppich, J., Forss, S., George, D., Grossmann, M., Goitein, G., Hilbes, C., Jermann, M., Lin, S., Lomax, A., Negrazus, M., Schippers, M., and Kotle, G. (2004). The PSI Gantry 2: a second generation proton scanning gantry. *Zeitschrift für medizinische Physik*, 14(1):25–34.

Peeters, A., Grutters, J. P. C., Pijls-Johannesma, M., Reimoser, S., De Ruysscher, D., Severens, J. L., Joore, M. a., and Lambin, P. (2010). How costly is particle therapy? Cost analysis of external beam radiotherapy with carbon-ions, protons and photons. *Radiotherapy and oncology : journal of the European Society for Therapeutic Radiology and Oncology*, 95(1):45–53.

Peeters, F., Verbeeten, B., Venema, H. W., Cormack, A. M., and Hounsfield, G. N. (1979). Nobel Prize for medicine and physiology 1979 for A.M. Cormack and G.N. Hounsfield. *Ned Tijdschr Geneeskd*, 123(51):2192–2193.

Perl, J., Shin, J., Schümann, J., Faddegon, B., and Paganetti, H. (2012). Topas: An innovative proton monte carlo platform for research and clinical applications. *Medical Physics*, 39(11):6818–6837.

Raju, T. N. K. (1999). The Nobel Chronicles. *The Lancet*, 354(9190):1653.

Röntgen, W. K. (1896). On a new kind of rays. *Nature*, 53:274–276.

Saito, N. and Bert, C. (2012). Scanned Ion Beam Therapy of Moving Targets with Beam Tracking. In Natanasabapathi, G., editor, *Modern Practices in Radiation Therapy*, pages 69–84. InTech Published.

Sawant, A., Smith, R. L., Venkat, R. B., Santanam, L., Cho, B., Poulsen, P., Cattell, H., Newell, L. J., Parikh, P., and Keall, P. J. (2009). Toward Submillimeter Accuracy in the Management of Intrafraction Motion: The Integration of Real-Time Internal Position Monitoring and Multileaf Collimator Target Tracking. *International Journal of Radiation Oncology, Biology, Physics*, 74(2):575–582.

Schippers, J. M., Dölling, R., Duppich, J., Goitein, G., Jermann, M., Mezger, A., Pedroni, E., Reist, H. W., and Vrankovic, V. (2007). The SC cyclotron and beam lines of PSI's new protontherapy facility PROSCAN. *Nuclear Instruments and Methods in Physics Research Section B: Beam Interactions with Materials and Atoms*, 261(1-2):773–776.

Schmuland, M. (2006). *Dose verification of rotating collimator intensity modulated radiation thearpy*. PhD thesis, University Of British Columbia.

Science (1957). Pioneer in X-Ray Therapy. *American Association for the Advancement of Science*, 125(3236):18–22.

Seco, J., Robertson, D., Trofimov, A., and Paganetti, H. (2009). Breathing interplay effects during proton beam scanning: simulation and statistical analysis. *Physics in Medicine and Biology*, 54(14):N283–94.

Siddon, R. (1985). Fast calculation of the exact radiological path for a three-dimensional CT array. *Medical Physics*, 12:252–255.

Smith, A., Gillin, M., Bues, M., Zhu, X. R., Suzuki, K., Mohan, R., Woo, S., Lee, A., Komaki, R., Cox, J., Hiramoto, K., Akiyama, H., Ishida, T., Sasaki, T., and Matsuda, K. (2009). The M. D. Anderson proton therapy system. *Medical Physics*, 36(9):4068–4083.

Szymanowski, H. and Oelfke, U. (2002). Two-dimensional pencil beam scaling: an improved proton dose algorithm for heterogeneous media. *Physics in Medicine and Biology*, 47(18):3313–3330.

Takahashi, S., Kitabatake, T., Morita, K., Okajima, S., and Iida, H. (1961). Methoden zur besseren Anpassung der Dosisverteilung bei der bewegungs Bestrahlung. *Stralentherapy*, 115:478–488.

Topolnjak, R., van der Heide, U., and Lagendijk, J. (2005). IMRT sequencing for a six-bank multi-leaf system. *Physics in Medicine and Biology*, 50(9):2015–2031.

Topolnjak, R., van der Heide, U., Raaymakers, B., Kotte, A., Welleweerd, J., and Lagendijk, J. (2004). A six-bank multi-leaf system for high precision shaping of large fields. *Physics in Medicine and Biology*, 49(12):2645–2656.

Van Der Walt, S., Colbert, S. C., and Varoquaux, G. (2011). The NumPy Array: A Structure for Efficient Numerical Computation. *Computing in Science & Engineering*, 13(2):22–30.

Vujosevic, B. and Bokorov, B. (2010). Radiotherapy: Past and present. *Archive of Oncology*, 18(4):140–142.

Wang, D., Hill, R., and Lam, S. (2006). US Patent 7015490: Method and apparatus for optimization of collimator angles in intensity modulated radiation therapy treatment.

Watanabe, T. (1963). Telecobalt radiation therapy which composed of rotatory cross section radiograph and rotatory conformation therapy unit. *Nihon Igaku Hoshasen Gakkai Zasshi. Nippon Acta Radiologica*, 23:841–848.

Webb, S. (2003). The physical basis of IMRT and inverse planning. *British Journal of Radiology*, 76(910):678–689.

Webb, S. (2010). Does the option to rotate the Elekta Beam Modulator MLC during VMAT IMRT delivery confer advantage? - a study of 'parked gaps'. *Physics in Medicine and Biology*, 55(11):N303–19.

Webb, S. (2012). A 4-bank multileaf collimator provides a decomposition advantage for delivering intensity-modulated beams by step-and-shoot. *Physica Medica*, 28(1):1–6.

Wideröe, R. (1928). Prinzip einer methode zur herstellung von kanalstrahlen hoher voltzahl. *Archiv Fuer Elektrotechnik*, 21(4):390–391.

Wilson, E. J. N. (1996). Fifty years of synchrotrons. *Particle accelerator. Proceedings, 5th European Conference, EPAC 96, Sitges, Spain, June 10-14, 1996*, C960610:135–139.

Wilson, R. R. (1946). Radiological use of fast protons. *Radiology*, 47(5):487–491.

Wong, J. W., Sharpe, M. B., Jaffray, D. A., Kini, V. R., Robertson, J. M., Stromberg, J. S., and Martinez, A. A. (1999). The use of active breathing control (ABC) to reduce margin for breathing motion. *International Journal of Radiation Oncology, Biology, Physics*, 44(4):911–919.

Yao, J. (1997). US Patent 5591983: Multiple layer multileaf collimator.

Zenklusen, S. M., Pedroni, E., and Meer, D. (2010). A study on repainting strategies for treating moderately moving targets with proton pencil beam scanning at the new Gantry 2 at PSI. *Physics in Medicine and Biology*, 55:5103–5121.